HIGH SPATIAL RESOLUTION INFRARED IMAGING OF JUPITER: IMPLICATIONS FOR THE VERTICAL CLOUD STRUCTURE FROM FIVE-MICRON MEASUREMENTS

Thesis by

Richard John Terrile

In Partial Fulfillment of the Requirements

For the Degree of

Doctor of Philosophy

California Institute of Technology

Pasadena, California

1978

(Submitted March 13, 1978)

To my parents

for their support,

their understanding,

and especially their love.

"There appear on the surface of Jupiter certain bands darker than the rest of the disc, and they do not always preserve the same form; that is proper to clouds."

Christiaan Huygens Cosmotheoros pub. 1698

ACKNOWLEDGMENTS

It is my pleasure to acknowledge those individuals who have assisted me in conducting this research effort. I am particularly grateful to Professor James Westphal, who as my research and thesis advisor, has provided invaluable guidance in the design and construction of the experimental hardware. It was through his patience and expertise, and in his labs that I was able to learn about and use state-of-the-art scientific equipment. I am also grateful to Professor Westphal for providing large amounts of 200 inch telescope time for this work.

I am indebted to Dr. Reinhard Beer and Dr. Fredric Taylor of JPL for their contributions to the spectroscopic aspects of this work. Dr. Beer coordinated efforts at the McDonald Observatory and provided infrared spectra of Jupiter nearly simultaneous with Palomar 5 μm imaging observations. I further thank him for providing the spectroscopic calibration and much of his time in useful discussions. I am grateful to Dr. Taylor for contributing the synthetic Jupiter spectra and for spending many hours of his time discussing ideas.

I am very grateful to David Diner, Andrew Ingersoll and Glenn Orton for providing useful inputs in discussions and for commenting on early versions of this work. I thank Richard Lucinio for his valuable help in designing and constructing the data system and for spending much time teaching me about digital electronics. I am grateful to Gerry Neugebauer, Keith Matthews, Eric Becklin, and Gordon Forrester of the Caltech infrared group for providing the wobbling

secondary, infrared calibration standards, and for the use of their equipment for the work at 8-20 μm. My thanks to Douglas Currie for the use of his color correction wedges. I am grateful to Sol Giles, Michael Carr, DeVere Smith and Victor Nenow for their instruction and assistance in building hardware.

I have greatly enjoyed my stays at Palomar and I thank the Hale Observatories staff for making observing runs so pleasant. Special thanks go to the scheduled night assistants on the 200 inch; Gary Tuton, Juan Carrasco, Brad Bailey and Kevin Jordan.

The efforts of Kay Campbell and Melissa Magdaleno in typing this manuscript are greatly appreciated. I also thank my friends Dave Diner, Tony Dobrovolskis, Pete Schloerb and the other Caltech graduate students for making my stay at Caltech more enjoyable.

A very special thanks to Pam Darkes and her family for their friendship and love.

Finally, I thank my parents and family for their encouragement, support, and love throughout my education.

This work was funded by Grant NGL 05-002-003 of the National Aeronautics and Space Administration.

ABSTRACT

This study describes the design and construction of a 5 μm imaging system used at the Hale 5 m (200 inch) telescope to acquire high spatial resolution infrared images of Jupiter. These images, recorded in a spectral region clear of terrestrial and Jovian gaseous absorption, offer a unique look into the deep atmosphere and provide direct observational evidence for the existence of multiple layers of clouds in the Jovian atmosphere. Evidence of layering is provided by the observed trimodal nature and persistence of the 5 μm flux-frequency distribution of equal areas on the Jovian disk. This indicates that three distinct brightness temperatures have a higher probability of being observed than a continuum of temperatures, and that, despite significant observed variations in the lateral 5 μm cloud distribution, this phenomenon is a long term stable vertical cloud feature. Furthermore, the visible color differences correlate with areas of different 5 μm intensity, implying that the colors are due to reflection from areas of different chemistry or state at different levels in the atmosphere. Also, short time scales are observed for large 5 μm flux variations over extensive areas of the Jovian disk, supporting the concept that the redistribution of obscuring clouds accounts for the contrasts at 5 μm. Finally, the 5 μm limb-darkening and opacity models, derived from imaging and spectroscopic measurements, are consistent with multiple layering of clouds in the Jovian atmosphere.

Further information about the Jovian clouds results from the combination of 5 μm spectroscopic and imaging data sets. From the shape

of the 5 μm spectrum true maximum brightness temperatures are derived, corrected for the clearest regions in the Jovian atmosphere. Furthermore, from data on spectral line saturation, limits are placed on the 5 μm cloud reflectivity over the field of view of the spectrometer. With this information, combined with the knowledge of the spatial flux distribution from imaging, constraints are derived for the optical properties of the upper Jovian clouds.

A three layer cloud model is developed which is consistent with all of the observational data at 5 μm. The three model cloud layers have cloud top temperatures of $T_1 \leq 190°K$ (presumably $T_1 \simeq 140°K$), $T_2 = 228 \pm 2°K$ and $T_3 = 292 \pm 8°K$. The highest layer, found only over the white zones and red spots, has optical depth near unity and transmits radiation from deeper levels. This upper level has a mean 5 μm cloud reflectivity less than 0.4, while the whole central 25% of the disk has a mean reflectivity less than 0.1. The middle cloud deck is present under the upper level clouds and over the brown colored Jovian belts. This level is optically thick everywhere except in regions where blue-gray areas are visible. Here the middle level thins to a mean optical depth of about 2 and allows radiation from the deepest and hottest level to be detected.

TABLE OF CONTENTS

TABLE OF CONTENTS

FIGURES

TABLE OF CONTENTS

FIGURES (Continued)

TABLE OF CONTENTS

FIGURES (Continued)

TABLES

TABLE OF CONTENTS

TABLES (Continued)

CHAPTER I

INTRODUCTION

The spectral region between 4.5 and 5.2 μm contains many keys to the understanding of the deep atmosphere and cloud structure of Jupiter. Gillett et al. (1969) first pointed out that observations of Jupiter in the 5 μm region reveal brightness temperatures of approximately 230^{o}K averaged over a large part of the central region of the disk. Westphal (1969) showed that the 5 μm flux is emitted from localized spots, primarily in the equatorial regions, and Keay et al. (1973), Westphal et al. (1974) and Terrile and Westphal (1977a) produced data showing the detailed morphology of the emitting regions. Due to the transparency of the main atmospheric components hydrogen, methane, and ammonia in this spectral region, the source of the spatial contrasts is probably particulate in nature. Thus, the 5 μm region is especially well suited for studies of the Jovian cloud structure.

Over the past several years, spectroscopic measurements in the 5 μm window have led to the detection of such atmospheric constituents as CH_3D (Beer et al., 1972; Beer and Taylor, 1973), CO (Beer, 1975), and H_2O (Larson et al., 1975). However, because of the complex nature of the flux distribution at 5 μm, and the necessarily low spatial resolution of the spectroscopic observations, these measurements have been difficult to interpret quantitatively. Since the 5 μm appearance of Jupiter is primarily due to the presence of clouds, high spatial resolution studies of the flux morphology and

limb-darkening, and the relationship between such data and spectroscopic and visible observations should help to resolve the nature of the 5 μm opacity sources, with particular emphasis on their vertical structure.

This study is a continuation of earlier photometric observations of Jupiter in the 5 μm atmosphere window. These new observations are conducted with the highest spatial resolution attainable from the ground and extend over an observing period of four years. Described in this thesis are the design and construction of the 5 μm imaging system used to produce digital images of Jupiter from the Hale 5 m (200-inch) Telescope. The analysis of these imaging data is discussed in terms of correlations with visible features, long and short term temporal variations in the cloud morphology, the planetary flux distribution, 5 μm limb-darkening, and correlations with the spectroscopic observations of Reinhard Beer obtained at the McDonald Observatory. The procurement of near-simultaneous high spatial resolution 5 μm images and high resolution spectra represents a significant advance in studies of the Jovian atmosphere, because of the rapid secular variations in the 5 μm radiation, which normally make interpretation of data acquired over long time intervals ambiguous. The results of these near-simultaneous observations have been used to constrain model cloud parameters and a model for the deep atmospheric cloud structure is presented.

Direct observational evidence is presented which demonstrates the existence of at least three different cloud layers in the atmosphere

of Jupiter. The 5 μm flux-frequency distribution across the Jovian disk is a trimodal function indicating that three distinct brightness temperatures are more likely to be detected than a continuum of temperatures. The existence of a correlation of visible color differences with areas of different 5 μm intensity suggest that the colors may be due to reflection from different levels in the atmosphere. Short time scales associated with large flux variations over extensive areas of the Jovian disk suggest that condensation and evaporation of obscuring cloud layers is taking place. Finally, limb-darkening and opacity models derived from imaging and spectroscopic data are consistent with multiple cloud layering in the Jovian atmosphere. The resulting cloud model has three layers of clouds. The highest, coldest clouds are apparently homogeneous and cover only the white zones. These clouds are optically thin at 5 μm and allow some radiation from the middle cloud layer to be detected. The middle layer is present in both the zones and brown colored belts. Patchy portions of this cloud correlate with blue-gray colored belts and permit observational access to the deepest cloud layer. Physical parameters for each of these layers are specified and constitute a preliminary model description for the deep atmospheric structure of Jupiter.

CHAPTER II

EQUIPMENT DESIGN

The recent practicality of ground-based infrared imaging at 5 μm has been made possible through the simultaneous development of improved detectors, low noise optical system designs, and digital data handling capabilities. All of these factors have contributed significantly to overcoming the problems associated with observing Jupiter at high spatial resolution at infrared wavelengths. This chapter details the imposed observational contraints on this task and describes the factors leading to its solution.

A. Observational Constraints

In the design and construction of the hardware used to produce images of Jupiter at 5 μm, several observational constraints were taken into account. Jupiter, at opposition, has an equatorial diameter of about 49 arcsec and covers a total sky area of about 1760 square arcsec. On the best nights, atmospheric seeing will blur a point source into a disk of about ½ to 1 arcsec in diameter. This means that in order to collect all the available information from Jupiter with the best spatial resolution attainable from the ground, about 7040 separate observations should be made over the planetary disk. This high sampling density is of particular importance at 5 μm since preliminary observations by Westphal (1969) indicated a high degree of 5 μm inhomogeneity across the Jovian disk with structure on scales as small as 1 arcsec.

Furthermore, the rotational period of Jupiter is about 9^h50^m (System I) so that an equatorial point on the central meridian moves 1 arcsec (2.3° of longitude) across the disk in nearly 4 minutes. If an image is to be constructed which preserves geometric and limb-darkening information, then all 7040 observations should be made in a time on the order of 2 minutes. These degrees of temporal (i.e., rotational) variability and sample density require a system which can achieve an acceptable signal-to-noise ratio with short integration times.

B. Detectors

The development of photovoltaic indium antimonide (InSb) detectors has greatly improved astronomical measurements at wavelengths shortward of 6 μm. At 5 μm these detectors have quantum efficiencies of about 60% and are background photon noise limited with the filters used. They also have the property of having little modulation or 1/f noise (a poorly understood mechanism characterized by a $1/f^n$ noise power spectrum, where n can vary from 0.8 to 2). This property allows photovoltaic InSb detectors to be operated without the severe drift and noise problems associated with bolometers. In most astronomical infrared measurements these noise problems are so severe that choppers are employed to interrupt the source measurements periodically with measurements of the sky background. The resulting fluctuating signal is then synchronously detected with an amplifier phase locked to the chopper reference modulation frequency.

The output of this amplifier gives a direct current (D.C.) voltage proportional to the flux of the source. This technique allows operation in the high-frequency region where detector and amplifier characteristics are more favorable. Unfortunately, it also requires that one-half of the observing time be spent measuring the sky background. Because of the low 1/f noise property of photovoltaic InSb detectors, this technique of synchronous detection is not employed in favor of a D.C. mode of operation which does not chop from source to sky. It is this characteristic of the detector which effectively halves the required observing time.

The observations, to be described in the next chapter, were made with a single photovoltaic InSb detector. Various array arrangements were considered, but a single detector was chosen due to low relative cost and simplicity of operation while still meeting all of the design constraints. A round 1 mm diameter InSb cell was obtained from Santa Barbara Research Center and fitted into a specially constructed dewar. The cell was thermally isolated from the outside and operated at liquid nitrogen temperature (77°K). Also mounted in the dewar and cooled to 77°K was the first stage of the preamp (a 2N4867A FET, and its load resistor). A 1.5×10^8 Ω load resistance was used for all the 5 μm observations and the resistor was mounted in an aluminum compartment separate from the detector to insure electrical shielding. At 77°K the dynamic resistance of the detector was about 5×10^7 Ω.

The external amplifier, which was shielded by an aluminum box attached to the dewar, could be operated in two modes. The normal D.C. amplifier mode was used for most of the observations. However, when sky conditions were especially variable an automatic drift reset amplifier mode could be used. In this mode the last sky measurements of every line are compared to a reference voltage. The zero level D.C. offset of the amplifier is then adjusted automatically to compensate for any drift from this reference level. This resets the start of every scan line to the same level and prevents under or over-saturations in digitizing the data due to long term drifts in the sky background. Amplifier gain was selected by a coarse-gain rotary switch and a fine-gain 10 turn digi-pot. Gain switch positions were calibrated in the laboratory and will be discussed in the next chapter.

C. Optical System

For all 5 μm observations, the east-arm Cassegrain focus of the Hale 5-meter (200-inch) telescope was used in combination with a wobbling Gregorian secondary mirror mounted in the prime focus cage. This combination was required to achieve the fast scan rates and short integration times necessary for the Jupiter observations. The figure of the wobbling secondary mirror is an axial section of an ellipse that has its closest focus coinciding with the prime focus of the f/3.33 primary mirror. At the second focus of the ellipsoidal secondary an f/72 image is formed.

The secondary is a 12-inch diameter aluminized CER-VIT mirror hinged on its back in a line perpendicular to its axis of symmetry and is mounted about 1.2 meters past the nominal prime focus. Two servoed shaker table drivers, 180° out of phase and mounted on opposite edges of the mirror, are used to drive the secondary. A position sensor at the edge acts as feedback device such that the mirror motions accurately reproduce any arbitrary electrical input wave form as long as the acceleration is less than 10^5 arcmin sec^{-2} and the amplitude is less than 4 arcmin, measured in the focal plane.

The f/72 image formed by the wobbling secondary is directed into the telescope's east-arm observing station by two optical flats. This optical configuration is illustrated in Figure 1. The f/72 beam comes to a focus on an optical bench where the photometer, detector, and associated electronics are mounted. The plate scale at the focal plane is about 0.56 arcsec/mm. The photometer base is about 1 meter long and is mounted on four posts such that the photometer mounting plate extends 18 cm from the telescope face plate. This provides a space for inserting other instruments (i.e., cameras) into the optical path and also allows the detector sensitivity to be checked conveniently once the dewar is mounted. The photometer base contains a Liberty Mirror IR-81-E gold coated dichroic placed at a 45° angle to the beam. The function of this dichroic is to act as a beam-splitter diverting the infrared component of the incoming beam into the entrance port of the liquid nitrogen dewar and allowing the visible component

FIGURE 1 - Optical configuration for the 5 μm imaging system. The left half of this figure shows the Hale 5 m telescope with the east-arm observing station facing front. On the right, drawn at the same scale, is the optical path and the arrangement of all the major optical components. The f/72 wobbling Gregorian secondary, located above the nominal focus of the primary, directs the beam to the Cassegrain focus in the east-arm by way of 2 flat mirrors. At the focus is the photometer base containing the dichroic, guiding optics, and dewar with its field optics and detector.

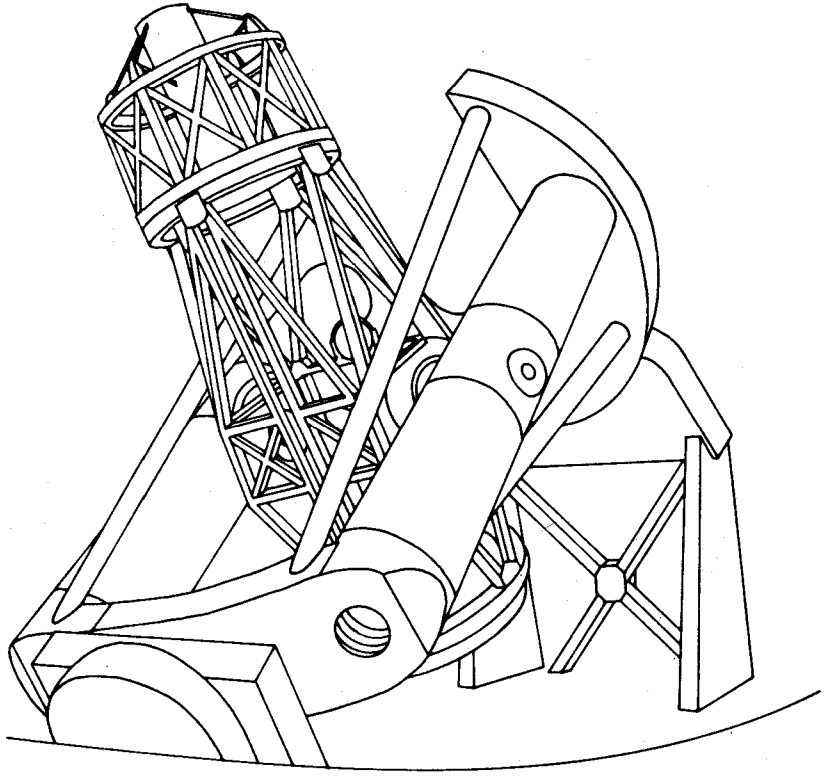

HALE 5-METER TELESCOPE

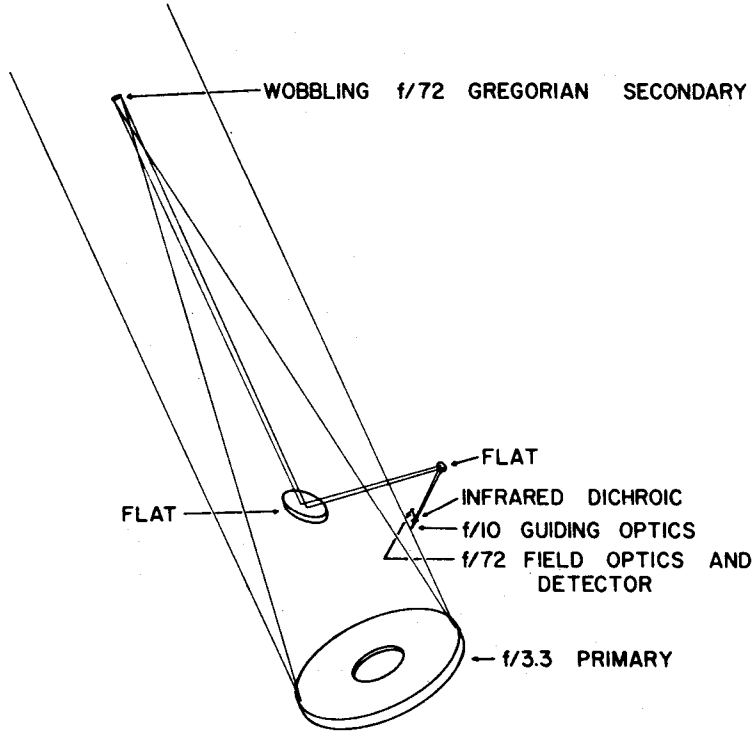

OPTICAL PATH

Figure 1

to be transmitted directly through and used for guiding. The reflectivity of the dichroic is a slowly varying function of wavelength and ranges from roughly 92% at 4 μm to about 94% at 8 μm. The transmission peaks in the visible is about 79% at 6000 Å.

The arrangement of the detector optics, filter, and aperture wheel is shown in Figure 2. The dewar is mounted in a cradle which can tilt or rotate to permit alignment of the detector optics with the wobbling secondary. Alignment is achieved by placing a chopped source at the wobbler and moving the dewar until the amplitude of the detector output is maximized. The f/72 beam enters the evacuated dewar through a 1 mm-thick sapphire window having a 5 μm transmission of 87%. Beyond this window is a radiation shield, thermally decoupled from the outside of the dewar, and cooled to 77°K. This shield completely surrounds and is also thermally decoupled from a cold inner assembly. Mounted on the inside surface of this shield is the 5 μm broad-band filter. A round 1.0" x 0.040" thick silicon interference filter was used for the 5 μm observations and had a transmission, measured at 77°K, of 91% at 4.87 μm with half power at 4.65 and 5.09 μm. At the focus of the beam, and mounted on the inner liquid nitrogen can, was a variable aperture wheel with 6 detented positions. Four round apertures with projected sky diameters of 0.75, 1.0, 2.0, and 5.0 arcsec were included along with a 1 x 5 arcsec slit and a cold, blanked-off position for measuring detector noise. This aperture wheel was operated by a steel shaft which was thermally isolated from the outside by a decouplable nylon key arrangement. A

FIGURE 2 - 5 μm Dewar Interior. Vertical Cross-Section Through the Optical Axis.

a. sapphire window
b. 4.6-5.1 μm filter
c. aperture wheel
d. barium fluoride field lens
e. InSb detector
f. preamp
g. inner nitrogen can base
h. radiation shield
i. nylon alignment struts
j. outer dewar case
k. aperture wheel steel shaft
l. nylon decouplable key
m. double O-ring vacuum seal
n. aperture selector knob
o. indicator - safety assembly
p. detector compartment
q. outer nitrogen shield
r. liquid nitrogen ($77^{o}K$)

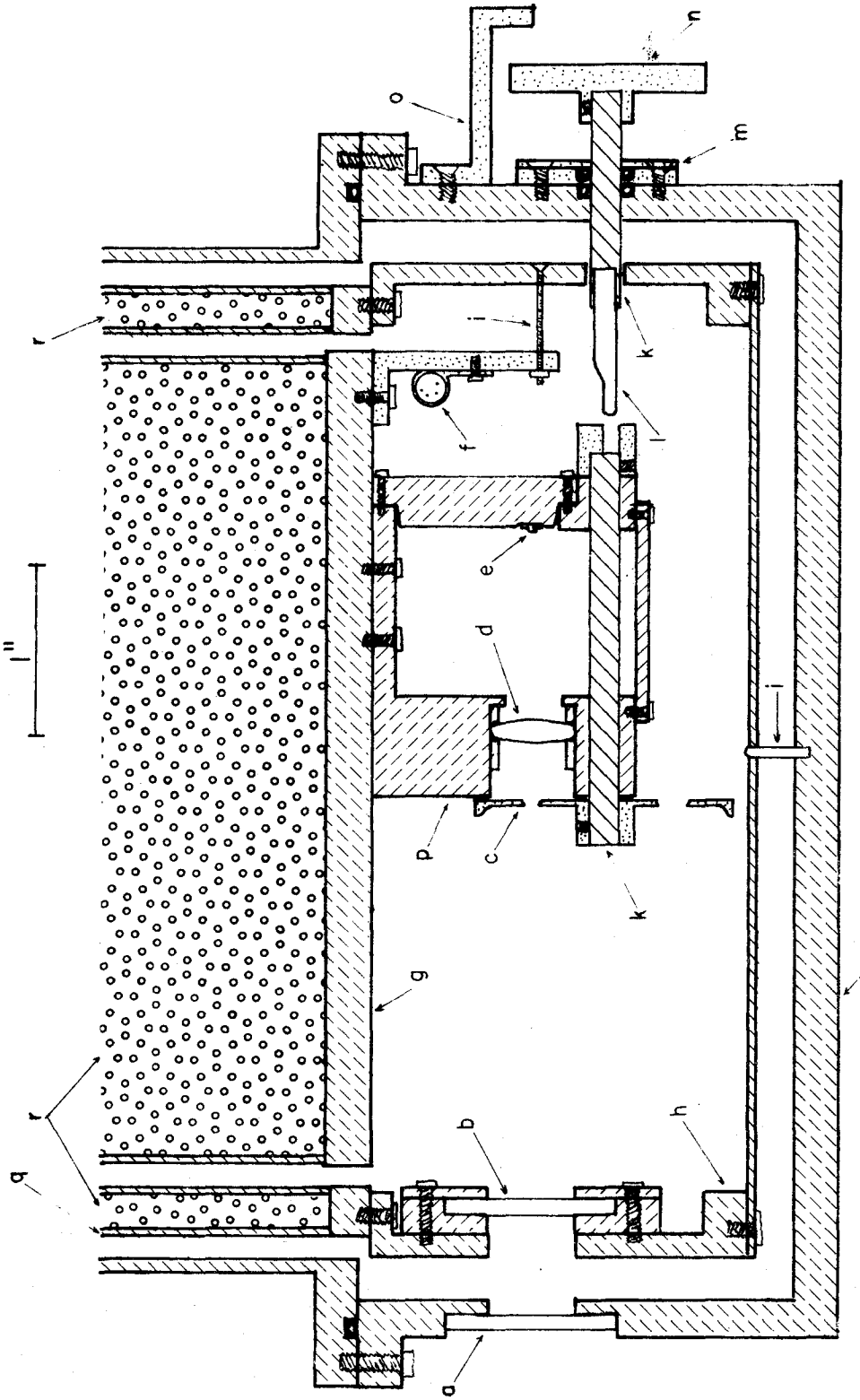

Figure 2

barium fluoride f/72 field lens with a 5 μm transmission of 95% was located beyond the aperture stop. This lens was initially positioned by focusing with visible light; a calculated position offset was then introduced in order to focus the 5 μm image of the telescope primary mirror properly onto the InSb detector. The inner liquid nitrogen can also contained the detector preamp and a compartment full of a ceramic molecular sieve which acted as a getter for residual gases. Thin nylon alignment struts maintained optical positioning and also reduced microphonic noise.

In addition to the infrared detector system, two other optical systems are employed for guiding and visible photography. The portion of the f/72 beam which is transmitted through the dichroic enters a 4.8 inch entrance aperture lens and is converted to an f/10 beam. The image at the focus of this lens is then reimaged through an elbow viewer which acts as a on-axis guider. The f/10 field of view is conveniently wide enough (about 1.5 arcmin) and the images bright enough to allow relatively efficient location of Jupiter and the calibration stars even in daylight. A system for acquiring color photographs between 5 μm imaging sequences was necessary for correlation of the infrared features with features seen at visible wavelengths. This was accomplished by occasionally interposing the telescopes' f/16 Cassegrain secondary in front of the wobbler so as to produce an image with a plate scale of 2.54 arcsec/mm. This

beam was intercepted in the space between the photometer and telescope mounting plate by a diagonal flat mirror, mounted on a rigid track perpendicular to the optical path. The intercepted beam was directed down the track to a second diagonal mirror and into a set of variable dispersion color-correction wedges and a Cannon 35 mm single lens reflex camera. For photographic sequences, this entire assembly was moved into place during the time required for changing secondary mirrors (about 5 minutes). The color-correction wedges were used to compensate for atmospheric color dispersion and were adjusted before each sequence by observing a Jovian satellite through the camera. The wedges were rotated until no color dispersion was observed on the satellite edges. Standard Kodachrome and Ektachrome ASA 64 color film was used and required exposures of ¼ to ½ second on Jupiter.

D. Data System

The control and monitoring of the imaging system is done from the east-arm using a data system. This system is designed to execute the several simultaneous functions which are required to build up a raster (facsimile) image. These functions include the control of the wobbling secondary mirror, as well as data integration, digitization, storage, and real time display. All of these functions are controlled by a 100 kHz quartz crystal clock.

Images are produced by moving the image of Jupiter in two dimensions across the detector aperture. This is accomplished by a combination of scanning with the wobbling secondary in declination

and introducing an offset in the telescope's sidereal tracking rate to produce a constant drift in right ascension. The data system digitally produces a stepped ramp with continuously adjustable amplitude. The number of steps per ramp can be chosen as 32, 64, or 128, and the dwell time at each step can be selected as 1, 10, 20, 40, or 80 msec. This ramp is converted to an analog signal and fed to the driver electronics of the wobbling secondary. Thus, the secondary steps the image along the celestial north-south line, remaining at each step for one dwell time and stepping a total distance determined by the amplitude of the ramp. At the end of each ramp excursion there is a reinitialization or flyback of the ramp and a settling time of 8 step lengths, during which there is no mirror motion. This flyback time is required to damp out vibrations set up in the wobbler after repositioning for a new scan. For the 5 μm imaging program scans consisted of 128 steps, each of 10 msec duration, plus 80 msec per scan for mirror flyback. This set of parameters allows a 128 x 128 picture element (pixel) image to be sampled in 174.1 seconds. Observations of Jupiter were performed with either the 1.0 or 0.75 arcsec aperture with pixel spacings of about 0.5 arcsec. Each resulting image had a projected sky area of about 60 x 60 arcsec.

The primary functions of the data system are to receive the analog output from the 5 μm detector amplifier, digitize the signal, and record the information on digital magnetic tape. The analog

detector output first enters an integrator circuit which accumulates the signal for one step time (i.e., 10 msec). At the end of each step, the output of the integrator is latched by a sample-and-hold circuit and then digitized to 8 bits (256 gray levels) with an analog-to-digital convertor (ADC). The sample-and-hold output is also monitored on an oscilloscope to insure that this signal does not saturate the ADC and to permit evaluation of the data quality. The output of the ADC is then fed into a Cipher Data Products, 800 bits-per-inch, 9 track digital tape recorder and written on magnetic tape in an IBM compatible format.

Another function of the data system is to provide real-time, two-dimensional display of the data. This is accomplished by reading the six most significant bits of every pixel into a digital scan converter. Depending on the number of pixels used per line (n), counters in the data system complete lines in such a way as to provide an n x n pixel image in the first n lines and samples of a 256 x 256 array. The complete 256 x 256 array is then displayed on a television monitor at the end of each data frame. Perhaps the greatest advantage of this feature is that it provides a real time first look at the data in image form. This is of great importance and utility for discerning features which might otherwise remain unnoticed until several days after an observing run when the stored data are reduced and examined in the laboratory. Real time decisions regarding the use of certain filters, the need for absolute photometric

calibrations, procurement of repeatable single-line scans, and sequencing of color photography may be made in response to the appearance of a particular TV display. Estimates of data quality, seeing, focus, tracking stability, and long-term detector drifts may also be made from the TV images.

CHAPTER III

OBSERVATIONAL DATA

In this chapter the processing of the 5 μm digital images will be described in detail. In addition, a discussion of the quality of the 5 μm data will be presented. The calibrations and observational procedures used to obtain 5 μm images coordinated with spectroscopic measurements will also be discussed.

A. Time and Data Quality of Observations

The first 5 μm images of Jupiter were produced at the Hale 5-meter telescope on UT 13 September 1973. Since that time, observations have been made during every apparition with time intervals between consecutive observing periods ranging from days to months. Table 1 lists the data upon which 5 μm Jupiter observations were made and tabulates the System I and II central meridian longitude coverage as well as estimates of the data quality (i.e., effects of atmospheric seeing, noise, etc.). On each night of observation on which the seeing was less than 1.5 arcsec, frames were recorded about every 3.5 minutes with occasional interruptions for procurement of standard-star calibrations and visible photographs. Two of these observing runs were coordinated with other Jupiter observations in order to enhance the data return. The coverage obtained on UT 3 December 1973 coincided with the regions of Jupiter observed at 20 and 45 μm by the Pioneer 10 spacecraft (Chase et al., 1974) three hours later. High spectral

TABLE 1

LOG OF JOVIAN 5 μm IMAGING OBSERVATIONS

Date (UT at start)	Central Meridian Longitude System I Start	System I End	System II Start	System II End	Resolution/Seeing (arcsec) Average	Best
13 September 1973	271°	286°	103°	119°	1-2	1
15 September 1973	169°	324°	347°	141°	1-3	1
16 September 1973	308°	131°	119°	300°	1-3	<1
19 September 1973	56°	266°	203°	52°	1-3	1
20 September 1973	253°	61°	33°	199°	1-2	<1
11 October 1973	212°	77°	192°	56°	2	2
3 December 1973	39°	149°	328°	77°	1-3	1
8 May 1974	181°	288°	3°	108°	2-4	2
9 May 1974	327°	74°	141°	247°	2-4	2
29 August 1974	45°	255°	87°	295°	1-3	<1
31 August 1974	50°	266°	76°	291°	2-4	1
1 September 1974	180°	293°	199°	311°	1-4	1
26 September 1974	177°	341°	5°	168°	2-4	2
27 September 1974	270°	133°	92°	312°	2-5	2
29 September 1974	214°	68°	20°	232°	2-4	2
23 September 1975	39°	271°	34[illegible]	215°	2-5	2

TABLE 1
(Continued)

LOG OF JOVIAN 5 μm IMAGING OBSERVATIONS

Date (UT at start)	Central Meridian Longitude System I Start	System I End	System II Start	System II End	Resolution/Seeing (arcsec) Average	Best
24 September 1975	234°	106°	172°	42°	2-5	1,5
25 September 1975	17°	264°	308°	192°	2-3	1
24 October 1975	246°	353°	316°	62°	2-4	1,5
25 October 1975	355°	154°	58°	215°	2-4	1
4 October 1976	216°	79°	165°	26°	1-3	1
5 October 1976	338°	216°	279°	155°	1-3	< 1

resolution 5 μm spectroscopic data were recorded at the McDonald Observatory on UT 3 October 1976 and correlate with the same area imaged at 5 μm at Palomar Observatory on UT 4 and 5 October of that year. Each of these correlations of other data sets with 5 μm imagery will be discussed in a later chapter.

B. 5 μm Image Processing

Raw data from the telescope are stored on magnetic tape in the form of 128 x 128 pixel x 8 bit (256 gray level) arrays. These digital images are then computer reformatted to 256 x 256 pixels for compatability with the picture playback system described by Westphal (1973). This playback system utilizes a digital scan convertor to display recorded images on a TV monitor. An oscilloscope is also used to display individual lines or columns of a particular image and it is possible to obtain a readout of the digital intensity of any pixel. Hard-copy black-and-white (either Polaroid or standard) photographs are produced using a Tektronix Type 602 Display Unit. This playback system is quite versatile so that many phases of the data analysis can be carried out without the need for more elaborate equipment. Figure 3 illustrates a raw 5 μm data frame of Jupiter which has been reformatted to a 256 x 256 array by duplicating each pixel in the horizontal and vertical directions. No averaging or smoothing has been done at this stage of the processing so every pixel in each 2 x 2 square has identical intensity. This image has a resolution of about 1½-2 arcsec, limited by the atmospheric

FIGURE 3 - A raw 5 μm data frame of Jupiter recorded at 23:11 UT 3 December 1973. This image was constructed by fast scanning the planet from south to north with the wobbling secondary and moving the telescope in right ascension with an east drift rate relative to the sidereal tracking rate. A slight mismatch in these two independent rates causes the image to appear too oblate. The only processing done to this frame was to repixellate it from 128 x 128 to 256 x 256 pixels for compatability with the picture playback system, and the addition of an identification label. Further processing centers the image, removes geometric distortions, rotates the image so that Jupiter's axis of rotation is parallel to the columns of pixels, and in the case for some inverted data, mirror-images the planet so that it appears to rotate in the right hand convention. A 1 arcsec aperature was used to record this image, however, the atmospheric seeing was about 2 arcsec. Consequently, several line tears can be seen in the image caused by hard seeing moving the entire image as it was being recorded. In this representation, hot regions on the planet appear bright and cold regions dark.

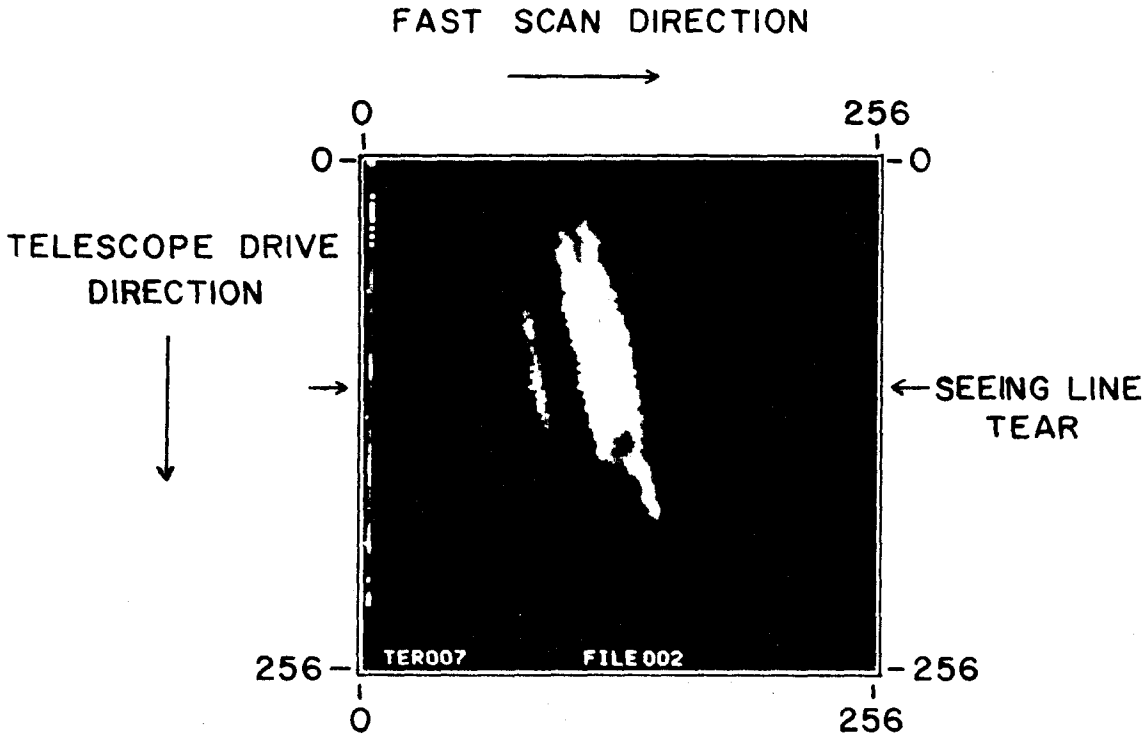
FAST SCAN DIRECTION
0
256
0
0
TELESCOPE DRIVE DIRECTION
SEEING LINE TEAR
TER007
FILE 002
256
256
0
256

Figure 3

seeing, and can be compared to images of much higher quality described later in this work. Note the distorted shape of the planet due to uneven pixel spacing in the scan and drive directions and occasional line tears (arrow). The line tears in this image are caused by "hard" atmospheric seeing which tends to move the entire planetary image across the aperture on a time scale comparable to the fast scan rate. Wave-like features induced by this type of seeing can be distinguished easily from real features because the artifacts will appear all along an entire scan line.

A great advantage offered by digital images in comparison to other forms of data is that very effective computer processing techniques can be applied. Several stages of digital image processing are applied to the Jupiter data in order to correct for low frequency signal drifts, improve signal-to-noise ratios, edit bit errors and line drops, and correct for geometric distortions. Low frequency detector drifts or background variability associated with broad sky gradients are removed by fitting a straight line to the first and last 10 sky pixels of every line. Each line is then tilted so that sky intensities at the start and end of each line are identical. When imaging regions on the Jovian disk which have low intensity or contrast, it is sometimes necessary to average a number of frames in order to increase the signal-to-noise ratio of the measurements. Registration of individual images prior to averaging is facilitated by defining the planetary limb and deriving a disk center. All

images are then shifted to a common location and added together pixel by pixel. The data averaging procedure has the effect of increasing the signal-to-noise ratio by roughly the square-root of the number of frames added, but also results in a longitudinal smearing of the planetary brightness distribution because of rotation. As a consequence of this smearing, only those regions in which longitudinal homogeneity can be assumed (i.e., some zones) are considered in the analysis of composite images produced using the averaging procedure.

Since images are constructed by fast scanning in one direction and driving the telescope at right angles, some geometric distortion (i.e., artificial equatorial or polar "flattening") occasionally occurs because of unmatched pixel spacing in the scan and drive directions. The appropriate geometric corrections are performed in an image processing program which repixellates an entire image and maps it into the correct geometry. For the purpose of simplifying subsequent data analysis, it is useful to orient the Jovian equator such that it is parallel to a data line or column. This requires an image rotation, which is performed in the same computer program responsible for geometric corrections. Since 128 x 128 pixel input arrays are mapped into 256 x 256 pixel output arrays, no loss of resolution is incurred as a result of these geometric and rotational transformations.

Occasional line drops or bit errors are edited by the standard procedure of filling in bad or missing data with the average

brightness represented by adjacent lines or pixels. This editing is performed on blemished data used for illustrations only, and serves a purely cosmetic purpose.

C. Calibration

In order to understand the physical significance of the 5 μm data, it is necessary to calibrate the flux measurements such that they can be converted into absolute brightness temperatures. These brightness temperatures can in turn be used to interpret the physical properties of the Jovian clouds. Three parameters are required in order to calibrate each night of observations in an absolute sense. First, a source of known brightness must be observed through the system in order to establish the electrical response of the detector to a known thermal flux. This is accomplished by scanning across a standard star with a round 5 arcsec aperture. The large aperture insures that all the stellar radiation is focused on the detector, particularly since the star image is smeared due to atmospheric seeing. Table 2 lists the standard stars used in the observations (Becklin, 1974; Beckwith, et al., 1976) as well as their respective magnitudes and positions. Several standard stars were imaged per night in order to intercompare sources of different flux levels. The second parameter necessary for the photometric calibration is the response of the detector electronics as a function of gain setting. Since standard stars are generally bright in comparison with Jupiter, and the dynamic range at a given gain setting is limited by the 8 bits

TABLE 2

5 μm CALIBRATION STARS

Name	RA (hms) 0^h 1 Jan 1976	Dec (° ' ") 0^h 1 Jan 1976	V Mag	Spectra Type	Magnitude at 4.8 μm
β And	1 08 22.9	+35 29 37	2,4	MO	-1.76
α Cet	3 01 01.3	+ 3 59 47	2.8	MO	-1.57
α Tau	4 34 32.5	+16 27 44	1.1	K5	-2,81
α Ori	5 53 52.3	+ 7 24 13	0-1	MO	-4.21
α Sco	16 27 55.9	-26 22 49	1.3	MO,A3	-3.81
α Lyr	18 36 07.5	+38 45 38	0.1	AO	0.00*
β Peg	23 02 36.4	+27 57 08	2.6	MO	-2.18

*Flux from a 0th magnitude star = 2.0×10^{-15} w/cm^2 μm at 4.8 μm.

of digitization, it is necessary to change the detector gain so that each object observed utilizes the full dynamic range. For this technique to work the output response vs. gain setting must be accurately known. The gain of the detector electronics was carefully measured in the laboratory by inputting a constant signal and recording the output as a function of gain setting. This was done at several different input values to insure system linearity as a function of input signal. It was found that the gain of the detector electronics is well behaved, linear, and reproducible to within 3%. The final parameter required for calibration is a measure of the atmospheric extinction as a function of zenith angle. This is obtained by choosing a standard star and recording its intensity several times during the night at several values of air mass. Standard stars are, in general, chosen so that they are close to Jupiter in the sky in order to insure that both objects are measured throughout a similar range of air masses. The results are then fitted to a Beer's Law relationship in which measured intensity is an exponential function of air mass. Deviations from this simple relationship are used as indications of unreliable data calibration due to non-photometric atmospheric conditions. On photometric nights calibration measurements will lie within the 5% error envelope of the derived extinction coefficient.

The total errors in the absolute calibration are obtained by summing all the contributing error sources. These sources of

uncertainty are in the absolute calibration of a zero magnitude star (α Lyr), the relative calibrations of secondary standards, the atmospheric extinction coefficient, and the gain reproducibility of the detector amplifier. On photometric nights these absolute calibration errors are on the order of 10%. In terms of calibrated brightness temperatures, this translates into an absolute temperature error of about 1.7°K at 225°K. Errors in relative temperature measurements on a single frame are determined by the signal-to-noise ratio and are usually smaller than absolute errors by about a factor of ten.

D. Spectroscopic Procedures

(i) Observations

An attempt was made in October 1976 to obtain simultaneous calibrated 5 μm images and spectra of Jupiter. The images were made with the previously described imaging system at the Hale 5 m telescope, and the spectra were obtained by Beer and Taylor (1978a) using a Fourier spectrometer at the 2.7 m telescope at McDonald Observatory (see Beer, et al., 1971 for a description of this system). Unfortunately, the erratic nature of weather between California and Texas made it impossible to obtain true simultaneity. Thus, the spectra were all obtained on UT 3 October 1976, while the images were acquired on the following two nights (and therefore within 3 to 5 Jovian rotation periods of the spectroscopic observations). The images, nevertheless, covered the same range of central meridians

observed spectroscopically. Obviously, near-simultaneity is less satisfactory than true simultaneity, but while Jupiter is variable both temporally and longitudinally, the temporal variations are, in general, of scales significantly longer than the Jovian rotational period.

The log of spectroscopic observations is presented in Table 3, each Jupiter run being interspersed by a similar scan of α Tau (a 5 μm standard-star that was within a few degrees of Jupiter). These observations were made with a field of view 20 arcsec in diameter, centered on the Jovian disk. Each scan was completed in 15 minutes or less in order to limit the range of central meridian longitudes (L_I). The resolution was kept to 2 cm^{-1} (apodized), in order to achieve a good signal-to-noise ratio (> 300 at the peak) with the exception of the last run (run number 1146) which was extended to a resolution of 0.1 cm^{-1}. Only the first part (i.e., out to a resolution of 2 cm^{-1}) of this last scan was used in the present analysis. A detailed analysis of the high resolution scan has been presented elsewhere (Beer and Taylor, 1978a, b).

(ii) Calibration

The procedure for calibrating Fourier spectra is sufficiently different from that employed in classical photometry that it bears a brief description. The calibration relies upon the property of a Fourier spectrometer that the amplitude of an interferogram, measured at zero path difference (equal interferometer optical

TABLE 3

LOG OF JOVIAN 5 μm SPECTROSCOPIC OBSERVATIONS:

UT 3 OCTOBER 1976

Run Number	L_I*		L_{II}**	
	Start	End	Start	End
1140	41°	56°	320°	335°
1142	101°	115°	20°	34°
1144	133°	142°	52°	61°
1146	157°	160°	76°	79°

* System I longitude of the central meridian at start and end of integration.

** System II longitude of the central meridian at start and end of integration.

paths), is directly proportional to the area under the measured spectrum, i.e., the true spectrum modified by transmission through the Earth's atmosphere, the telescope, and the interferometer. These three modifiers are treated separately. The absolute instrumental response function is determined by observation of an internal blackbody standard, and the telescope transmission is determined from observations of standard stars. Unfortunately, stars are standardized only at infrequent spectral intervals, and it must be assumed that the transmittance is invariant over a particular spectral region of interest. In the present case, the transmittance of the 2.7 m telescope coude system was determined both at $L(\bar{\upsilon} = 2940\ cm^{-1})$ and $M(\bar{\upsilon} = 2083\ cm^{-1})$ and found to be 0.29 ± 0.03 at both frequencies after correction for the effects in the terrestrial atmosphere. The same value was assumed to pertain across the entire 5 μm window. The apparent spectrum is divided by this factor, thus providing a measure of the spectrum corrected for telescopic transmission losses.

The problem of the Earth's atmosphere, especially in the 5 μm window, is much more difficult. The classical technique of observing the source over a wide range of air masses cannot be applied to Jupiter because of the planet's rapid intrinsic rotational variability. The alternative approach of following a standard star also was not feasible because of the unsatisfactory signal-to-noise ratio at 5 μm and the shortage of observing time. The less satisfactory, but more practical, approach of employing the Sun as an extra-

atmospheric light source and obtaining extinction coefficients on a statistical basis has therefore been used. Solar observations over a wide range of air masses have been accumulated over several years (Beer, 1976). From these, it is found that within certain selected microwindows (a microwindow is a spectral interval of low or moderate extinction typically about 2 cm^{-1} wide) the received intensity is well characterized by an expression of the form

$$I = I_o \exp\left[-(a\,x + b)\,\bar{m}\right] \quad , \qquad (1)$$

where I and I_o are the received and extra-atmospheric intensities, respectively, $\bar{m}$ is the weighted mean airmass for the observation, x is the local absolute humidity, and a and b are empirically derived constants. In the 5 μm region, it is found that a is significant only for frequencies less than 2112 cm^{-1}. That is, between 2112 and 2167 cm^{-1}, and extinction is independent of the local water content of the atmosphere. Fourteen such microwindows from 1930 to 2167 cm^{-1} have been employed in the present analysis. The results of these spectroscopic observations and the 5 μm imaging will be presented in the next chapter.

CHAPTER IV

OBSERVATIONAL RESULTS

This chapter describes in detail the observational properties of the 5 μm emission from Jupiter. The discussion consists of several parts. First, the morphology and temporal variations associated with broad and small-scale features on the Jovian disk are discussed and a comparison is made with visible features seen in color photographs. Second, a quantitative description of the 5 μm flux distribution over the disk is given and the data are calibrated in terms of absolute brightness temperatures. Third, limb-darkening data are presented for various regions on the Jovian disk. Finally, descriptions of two near simultaneous, synergistic observations of Jupiter involving the 5 μm imaging data are presented. The first involves 20 and 45 μm images obtained by the Pioneer 10 spacecraft and the second deals with high spectral resolution spectroscopy in the 5 μm region. In the first case, a qualitative description of correlated features is given, and in the second case a set of quantitative parameters is given which will be used to constrain Jovian cloud models. An atmospheric model for the vertical cloud structure of Jupiter which makes use of the data presented here will be developed in the next chapter.

A. Correlation of 5 μm Images with Visible Photographs

This section is an extension of the color comparison work started by Westphal (1969) and continued by Keay *et al.* (1972, 1973),

Westphal et al. (1974), and Terrile and Westphal (1977a). More detailed comparisons have been made possible recently, owing to the simultaneous acquisition of high spatial resolution 5 μm images and color photographs. An example of such a comparison is presented in Figure 4, which shows a black and white print made from a Kodachrome slide taken at 04:12 UT 20 September 1973 and a 5 μm image recorded 10 minutes earlier. The visible appearance of Jupiter in this view (Figure 4a) is typical of the planets appearance in 1973 and 1974 and will be used to define individual features. The nomenclature used is similar to that employed by Peek (1958) in defining the most prominent belts and zones. In the picture shown in Figure 4a, the South Tropical Zone (STrZ), appears very broad and extends from about -10° to -27° latitude. At more typical times, Jupiter displays a southern component to the South Equatorial Belt (SEBs) which splits the STrZ and appears at a latitude of about -16° to -21°. This component is only faintly present in the 1973 and 1974 visible data. The northern component of the South Equatorial Belt (SEBn) as well as the southern component of the North Equatorial Belt (NEBs) have well defined north and south sub-components. The equatorward sub-components appear blue-gray in color photographs while the higher latitude equatorial belt sub-components appear brown. The plume visible in the Equatorial Zone (EZ) is also blue-gray and has been observed at least as long ago as 1964 (Smith and Hunt, 1976). In addition to belts, zones, and associated plumes, a prominent feature

FIGURE 4 - The positions of the most prominent belt and zone features are shown in this comparison of a visible photograph and a 5 μm image of Jupiter. Figure 4a is a black and white print of a Kodachrome slide taken at 04:12 UT 20 September 1973. Figure 4b is a 5 μm image recorded 10 minutes earlier with approximately the same central meridian longitude. In both images north is at the top and east is at the right. The column in between the images shows the positions and nomenclature for the Jovian features after Peek (1958). The abbreviations used are as follows:

NPR	North Polar Region
NTeB	North Temperate Belt
NTrZ	North Tropical Zone
NEB	North Equatorial Belt (2 components)
EZ	Equatorial Zone
SEB	South Equatorial Belt (2 components)
STrZ	South Tropical Zone (with GRS - Great Red Spot)
STeB	South Temporate Belt
STeZ	South Temperate Zone
SPR	South Polar Region

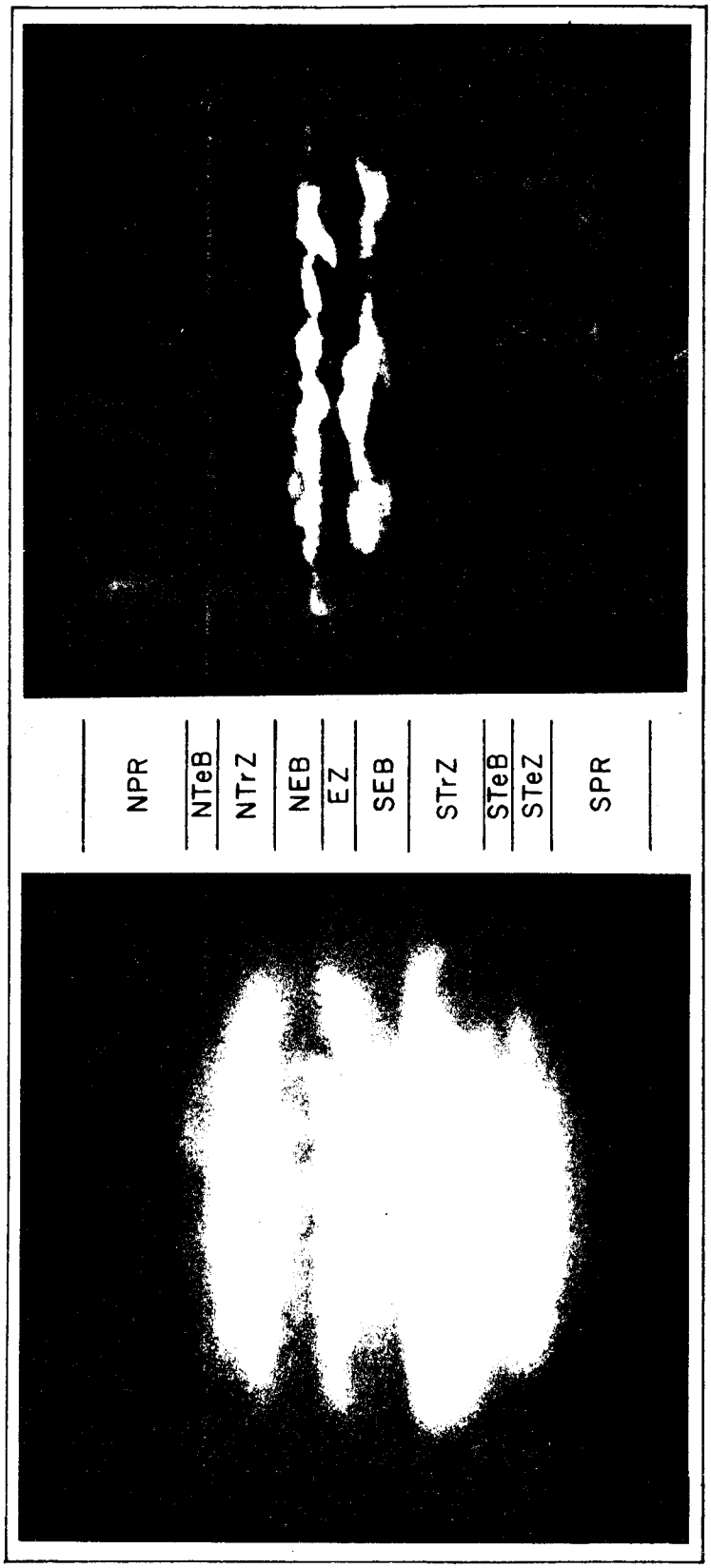

Figure 4

on Jupiter is the Great Red Spot (GRS), which normally resides in the STrZ. A smaller red spot may ocasionally be observed in the North Tropical Zone (NTrZ). The positions of most of the features described above are indicated in Figure 4.

The most striking feature of a 5 μm Jupiter image (see Figure 4b) is the marked latitudinal contrast. Regions of low flux correlate with zones on the visible photograph. Zones exhibit the lowest levels of 5 μm flux and are only slightly brighter than the background sky. In general, zones appear uniform and homogeneous and contain no localized hot spots. The only observed exception to this homogeneity occurs when the Equitorial Zone is interrupted by dark plumes originating in the North or South Equatorial Belts. In such cases, the plumes correlate with hot 5 μm features.

In general, areas of high 5 μm emission correlate with the dark visible features. The main exceptions to this are the red spots which appear in Jovian zones. These spots are characterized by low albedos in the blue and exhibit the lowest levels of 5 μm flux. Perhaps the best known and best observed example of this is the Great Red Spot in the South Tropical Zone. Figures 4a and 4b show that there is large contrast between the GRS and the STrZ in the visible; however, the red spot is indistinguishable from the zone at 5 μm.

Unlike zones, belts are heterogeneous in 5 μm flux distribution and exhibit a wide range of brightness temperatures. Figures 5 and 6

show four different longitude regions of Jupiter at 5 μm obtained in September 1973. Contour maps of the 5 μm flux are also provided to illustrate further the belt-zone morphological differences. Belts are often resolved under the best seeing conditions into two or more filaments of high emission. Along these bright filaments the most intense localized hot spots may often be observed. These spots are associated with the blue-gray features on visible photographs. The edges of the North and South Equatorial Belts are usually areas where the highest flux levels are observed, while a relatively cooler region covers the main body of the belt. This cooler belt region is nevertheless warmer than zones at 5 μm.

Five micrometer emission from high latitude belts and polar regions also follow the correlation of hot 5 μm features with areas of low visible albedo. The North and South Temperate Belts, shown in Figures 5 and 6, contain concentrations of hot 5 μm features. The southern edge of the South Temperate Belt (STeBs) is often interrupted by features which appear in visible photographs as white ovals. These features were first observed in 1939-40 as three bright clouds, each extending more than 100,000 km in length (Peek, 1958). Since that time, each has contracted to its present size of about 14000 by 8800 km. The ovals are zone-like in their cold 5 μm appearance and in their lack of color in visible photographs. The correlation between hot 5 μm areas and low visible albedo also holds in the polar regions. Above 45° latitude

FIGURE 5 and FIGURE 6 - 5 μm images and contour maps of four different longitude regions on Jupiter during September 1973. Contour maps are linear in flux and have not been geometrically rectified. They are shown to illustrate the inhomogeneity of 5 μm brightness across the planetary disk. Figure 5a was recorded at 04:02 UT 20 September 1973 with a System I central meridian longitude (L_I) of 221.7° and a System II central meridian longitude (L_{II}) of 345.8°. Figure 5b was recorded on the same date at 06:30 UT with L_I = 313.1° and L_{II} = 76.4°. Figure 6c was recorded at 03:07 UT 19 September 1973 with L_I = 30.8° and L_{II} = 162.9°. Figure 6d was recorded on the same date at 05:32 UT with L_I = 118.6° and L_{II} = 249.9°.

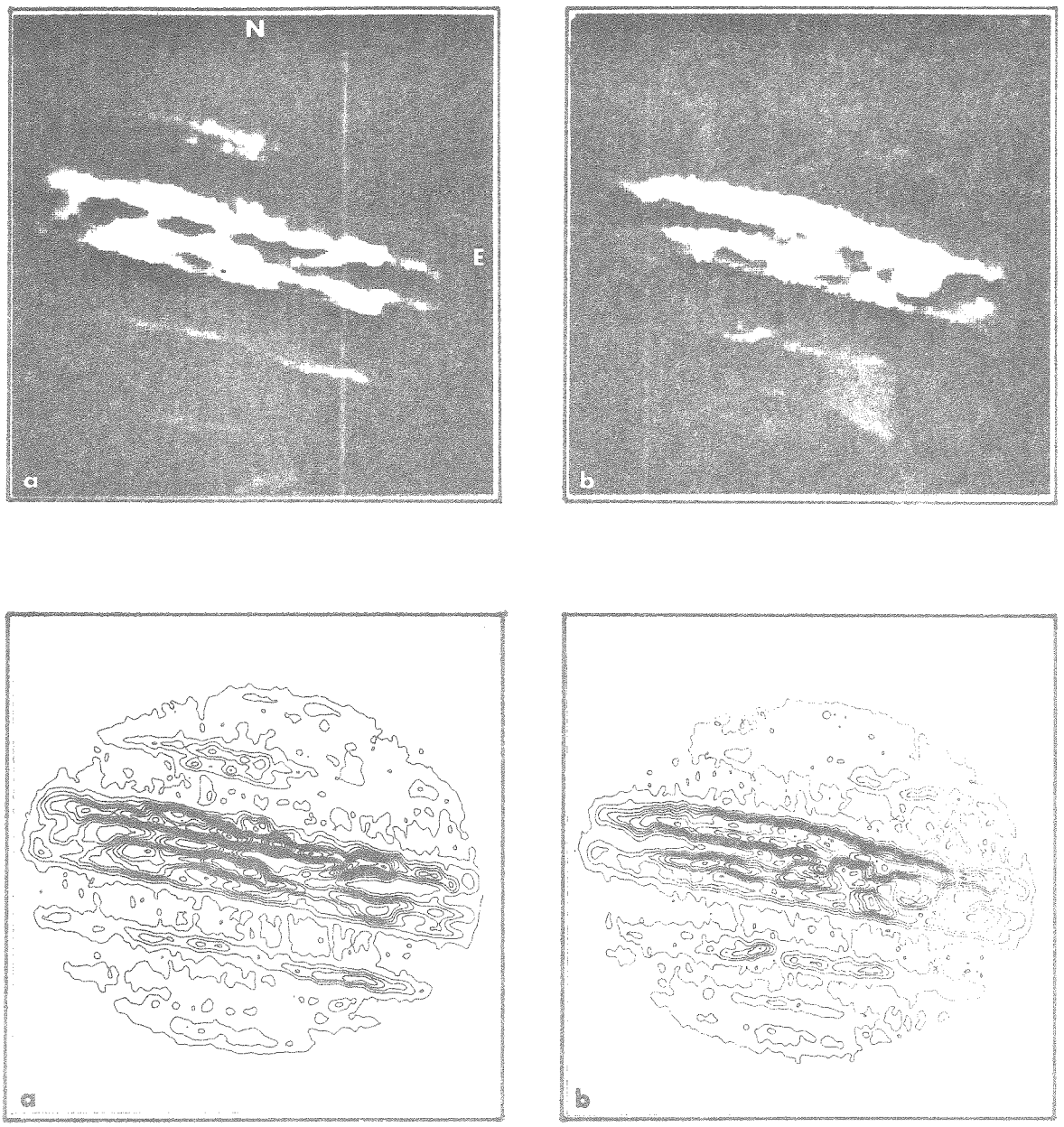

Figure 5

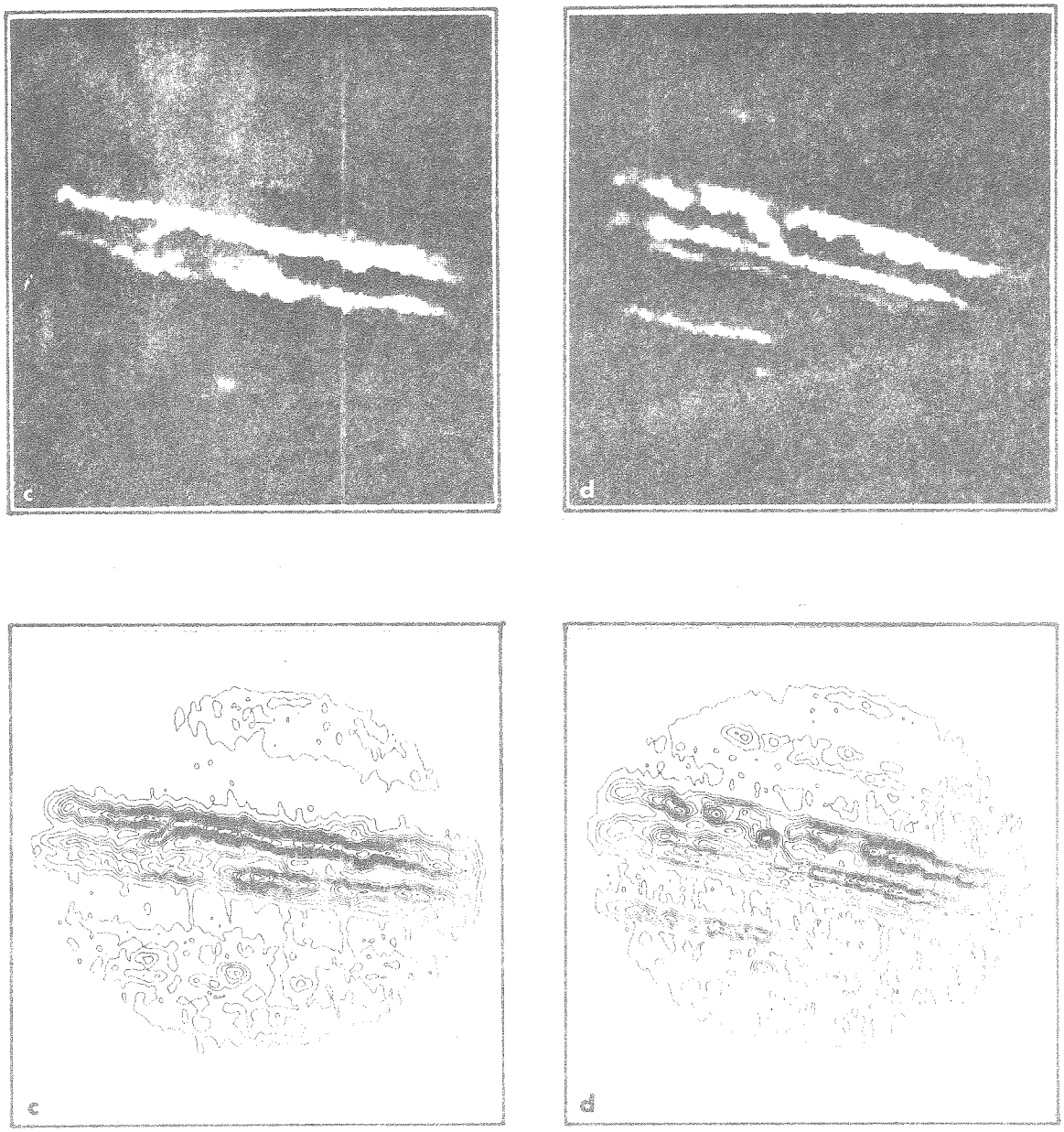

Figure 6

Jupiter's atmosphere departs from the belt-zone structure characteristic of the lower latitudes but retains a low albedo, belt-like appearance (Baker et al. 1975). These polar areas are hot 5 μm features.

Ground-based photographs, as well as Pioneer photopolarimeter images, reveal small doughnut-like features in the North North Temperate Belt (NNTB) and the South South Temperate Belt (SSTB). These features are rings of dark material with white cores and are surrounded by lighter areas. Figures 7a and 7b show a comparison of a black and white print made from a Kodachrome slide taken at 09:13 UT 29 August 1974 and a negative 5 μm image obtained 15 minutes earlier. The dashed line in Figure 7a shows the actual position of the limb which was lost due to contrast enhancement. The arrows point to a resolved doughnut-like feature in the southern hemisphere. These features were resolved at 5 μm using a 0.75 arcsec aperture, and the doughnuts appear as hot ring-like features with cold cores. The dark doughnuts are about 8000 km in diameter with central cores of about 3000 km in diameter.

B. Global Variations of Jupiter's Cloud Morphology

Jupiter's visible appearance over the last four years has undergone several interesting changes on a large scale. No attempt is made here to describe in detail the long history of observations of Jupiter's visible cloud features. For a complete and detailed account

FIGURE 7 - Comparison of a visible photograph of Jupiter with a 5 μm image. Both images are oriented with north at the top and east at the right. Figure 7a is a black and white high-contrast print from a Kodachrome slide, with System I and System II central meridian longitudes of 249° and 289°, respectively. The dashed line shows the actual position of the limb which was lost by contrast enhancement. Figure 7b is a negative 5 μm image with System I and System II central meridian longitudes of 210° and 250°, respectively. Arrows point to a resolved doughnut-like feature in the southern hemisphere. Both images were taken on UT 29 August 1974.

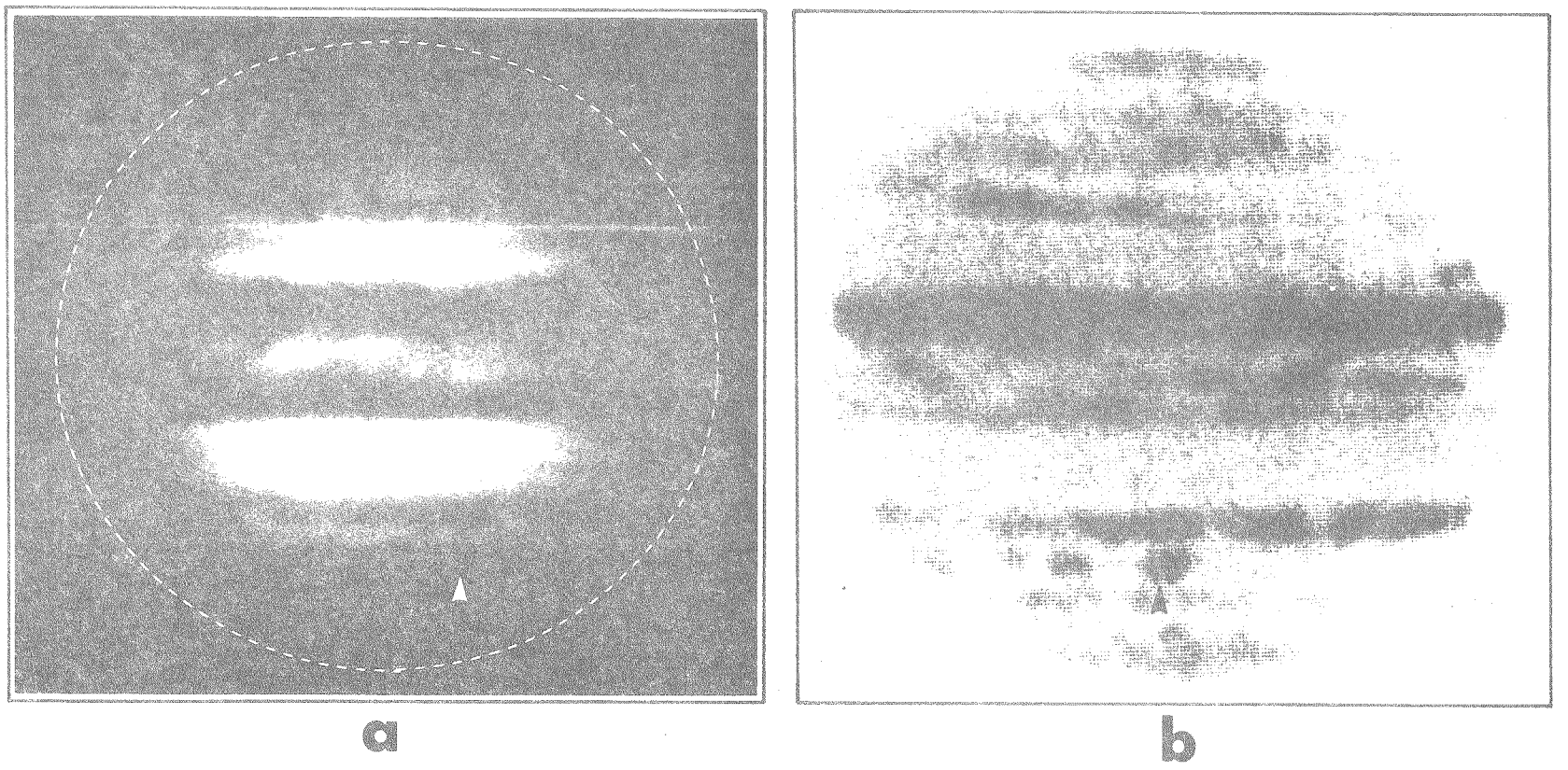

Figure 7

of these observations, the reader is directed to Peek (1958) and Smith and Hunt (1976). However, for the aims of this study, some discussion of the cloud and color changes which occurred on Jupiter during the period of observations is warranted. This discussion is the subject of this section.

(i) Variations in the Visible

Significant large scale changes in the visible morphology of the Jovian cloud features can be seen in Figure 8. This figure shows 4 views of Jupiter on 04:12 UT 20 September 1973, 06:45 UT 28 September 1974, 07:41 UT 25 September 1975, and 12:58 UT 4 October 1976. Note that Figures 8a and 8b, the pictures from 1973 and 1974, are very similar. The positions of the most prominent belts and zones have remained unchanged and the only color difference is the subtle loss (in 1974) of blue color in the equatorward edge of the SEBn. Differences between the 1974 and 1975 appearance of Jupiter are seen clearly in Figures 8b and 8c. In 1975 the dark SEBs appeared in what was a very broad and featureless STrZ. The area between the northern and southern components of the SEB to the east of the GRS appears white and featureless, that is zone-like. However, to the west of the GRS this same latitude band is dark gray in color and mottled. This appearance is part of the characteristic trend which has been observed in the SEB many times before (Peek, 1958; Reese, 1972; Smith and Hunt, 1976). A disturbance in the SEB generally starts out as a localized outburst of bright and dark spots and eventually

FIGURE 8 - Yearly comparisons of Jupiter in the visible from 1973 to 1976. In this figure black and white reproductions of Kodachrome (Figures a and b) and Ektachrome (Figures c and d) slides illustrate the global cloud variations which occurred on Jupiter over a four year period. Figure 8a was acquired at 04:12 UT 20 September 1973 with System I and System II central meridian longitudes (L_I and L_{II}) of 272° and 51°, respectively. Figure 8b was acquired at 06:45 UT 28 September 1974 with $L_I = 187°$ and $L_{II} = 0°$, and Figure 8c was acquired at 07:41 UT 25 September 1975 with $L_I = 99°$ and $L_{II} = 29°$. Finally, Figure 8d was acquired at 12:58 UT 4 October 1976 with $L_I = 65°$ and $L_{II} = 13°$. In all the images the Great Red Spot is visible (lower left in Figure 8d) and north is at the top and east at the right. The low contrast in Figure 8d is a real feature of the planet and not the result of image degradation by seeing or poor film quality. The seeing during acquisition of these images was one arcsec or less.

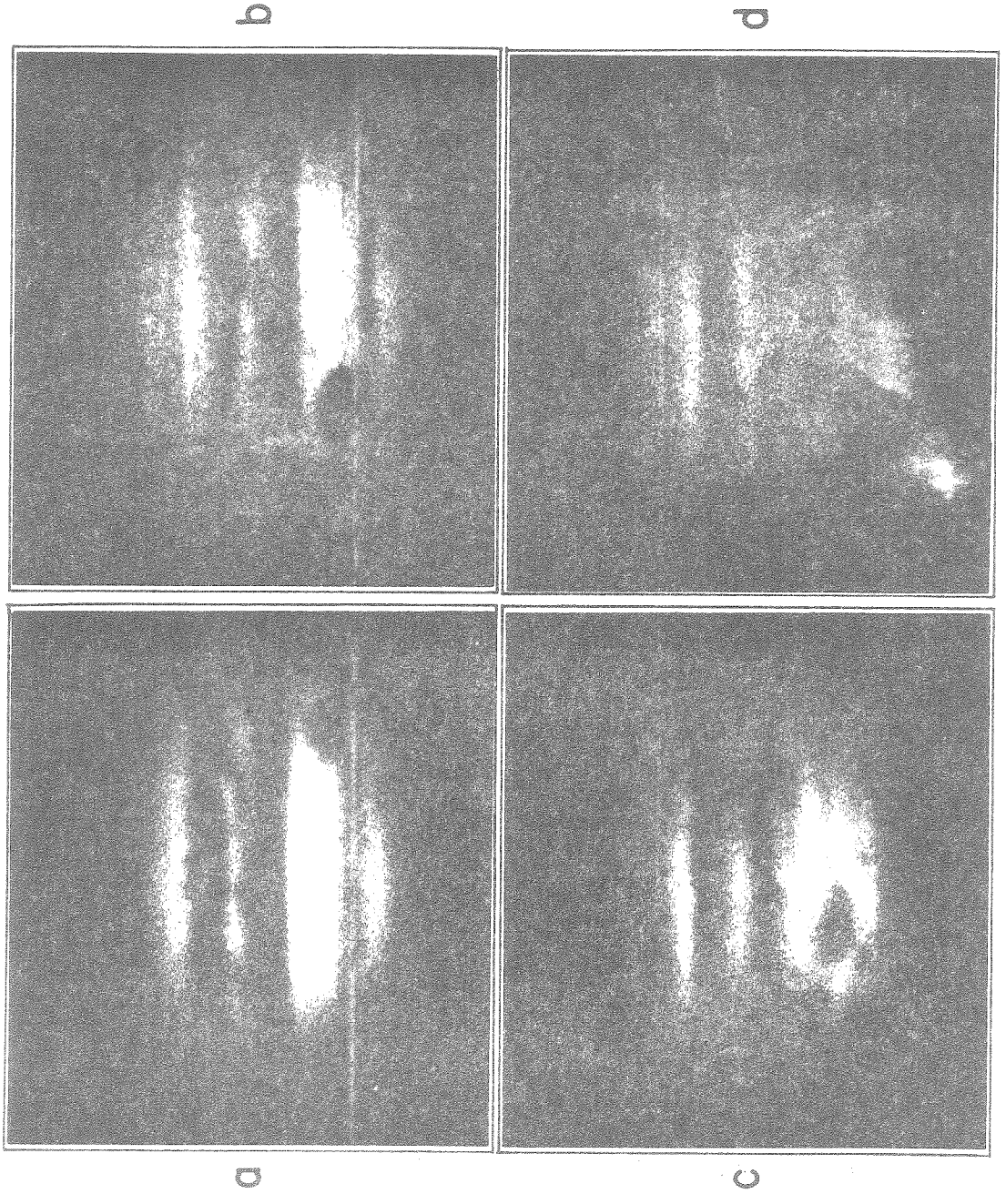

Figure 8

spreads in longitude until the entire belt displays a mottled appearance. Figure 8c shows Jupiter part-way through this transition. The STeB, which was in longitudinally homogeneous in 1973 and 1974, appears to have broken up into small fragments in the 1975 view. Other changes apparent in the 1975 picture are that the equatorward edge of the SEB regained its blue color and the NEBn acquired a conspicuous dark brown color. Figure 8d shows that in 1976 the South Equatorial Belt disturbance completely obliterated the zone (i.e., the STrZ) separating its northern and southern components. This very wide belt appears blue-gray on its north edge and brown to the south. The Great Red Spot has lost most of its contrast because of its proximity to dark material surrounding the red spot and in a belt directly to the north. The NEB remains unchanged from the previous year but the STeB once again displays a homogeneous appearance. In summary, the past four years of Jovian cloud activity has been characterized by color variations in all belts and by a major South Equatorial Belt disturbance resulting in the darkening of a large part of the South Tropical Zone.

(ii) Variations at 5 μm

The rather dramatic changes in Jupiter's physical appearance at visible wavelengths have been manifested in the 5 μm appearance of the planet as well. Figure 9 shows four 5 μm images acquired on 04:02 UT 20 September 1973, 07:23 UT 31 August 1974, 04:46 UT 25 September 1975, and 08:54 UT 5 October 1976, respectively. The difference

FIGURE 9 - Yearly comparisons of Jupiter at 5 μm from 1973 to 1976. This figure illustrates the 5 μm global cloud variations which occurred on Jupiter over a four year period and is complementary to Figure 8. Figure 9a was recorded at 04:02 UT 20 September 1973 with System I and System II central meridian longitudes (L_I and L_{II}) of 266° and 45°, respectively. Figure 9b was recorded at 07:22 UT 31 August 1974 with L_I = 107° and L_{II} = 133°, and Figure 9c was recorded at 04:46 UT 25 September 1975 with L_I = 353° and L_{II} = 284°. Finally, Figure 9d was recorded at 08:54 UT 5 October 1976 with L_I = 75° and L_{II} = 16°. In all the images north is at the top and east at the right.

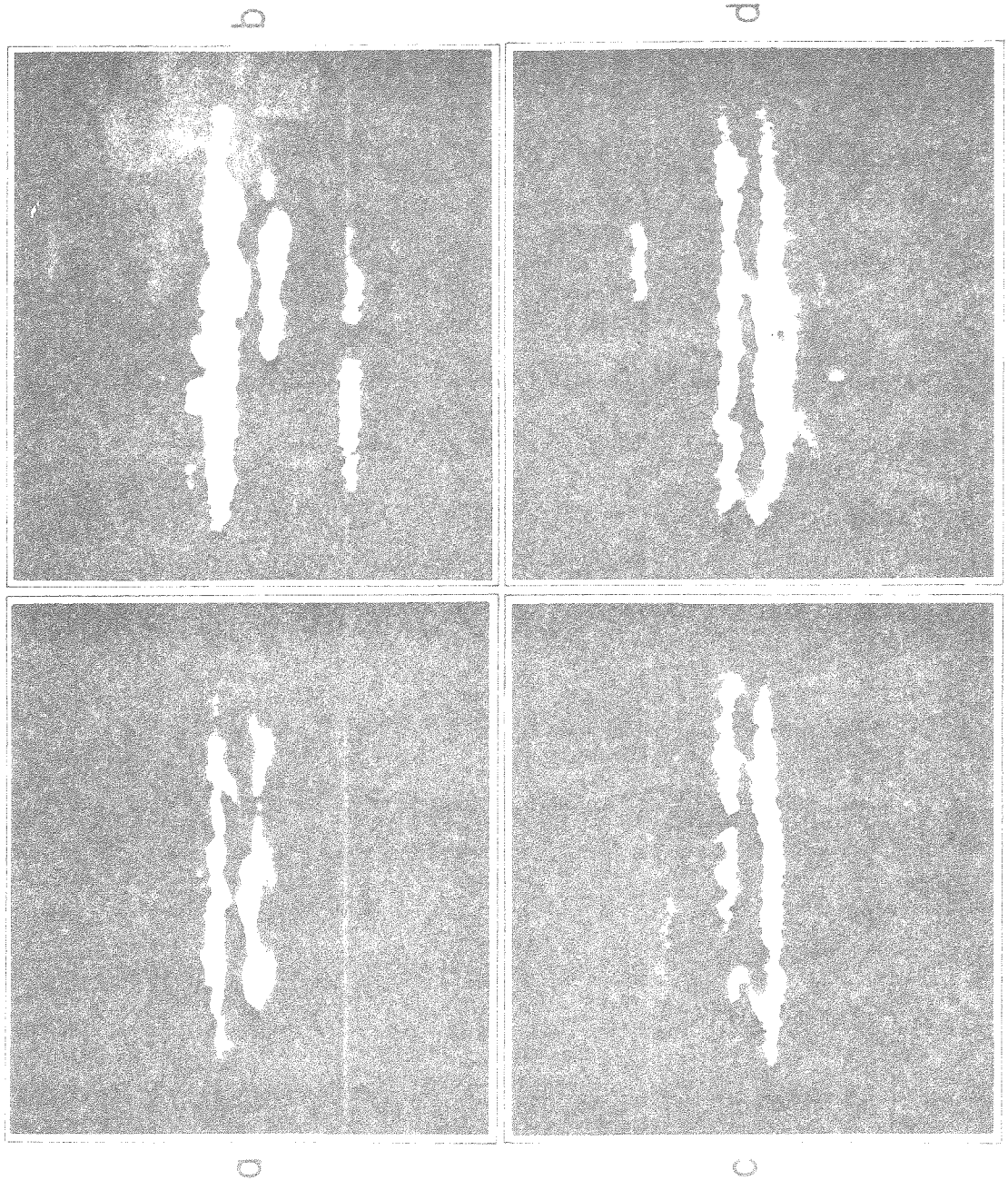

Figure 9

between the 1973 and 1974 apparitions is shown in Figure 9a and 9b. Jupiter's 5 μm appearance changed from a symmetric equatorial belt configuration to one in which the North Equatorial Belt is much more prominent than its southern counterpart. This is a result of a decrease in the 5 μm flux emitted from the South Equatorial Belt to 35% of the value observed in 1973. The area affected by this flux decrease corresponds to the same latitude region which changed color from blue-gray to brown in visible photographs. Five micrometer emission from the SEB increased again in 1975 and once again equaled or surpassed the emission from the NEB (see Figure 9c). Less intense levels of emission may be seen in the otherwise cold STrZ. These areas correspond to dark features on visible photographs and seem to be related to the start of the South Equatorial Belt disturbance. In Figure 9d, from 1976, the SEBs is continuous and bright at 5 μm. The brightest features, in this view, are the equatorward components of the North and South Equatorial Belts, which are of roughly equal intensity. The Great Red Spot, which normally does not appear in 5 μm images, is visible in the lower left as a dark area because it is surrounded by hot features. In general, all of the major changes at 5 μm, over the past four years have taken place in the equatorial belts and at higher latitudes in the southern hemisphere.

C. Short Time-Scale Changes in 5 μm Features

Significant morphological changes in some of the detailed structures observed in the clouds of Jupiter have been seen to occur on time scales much shorter than those associated with the previously

discussed global changes. Peek (1958) describes a number of occurrences where visible cloud features in the South Equatorial Belt were observed to change dramatically as they rotated from a position roughly 30° west of the central meridian to roughly 30° east. These observations imply changes on a linear scale of at least 3000 km occurring over a period of about 1 hour 40 minutes. The visible cloud morphology within the Equatorial Zone has also been observed to undergo rapid changes. The structure of specific features has changed noticeably during a single rotation of the planet, i.e., over a period of about 10 hours (Smith and Hunt, 1976). Similar changes in Equatorial Zone features have been recorded at 5 μm. Figure 10a and 10b show a comparison of two 5 μm Jupiter images recorded at 03:00 UT 16 September 1973 and 05:16 UT 20 September 1973, respectively. The System I longitudes of the central meridians of the images are within 13°. Both of these images were obtained when the seeing was better than 1 arcsec. Figure 10b shows a clearly resolved bright area in the center of the Equatorial Zone which is about 12,000 km in diameter. Ten Jovian rotations earlier, however, (in Figure 10a), the feature appeared markedly different and was less intense by a factor of two. In terms of brightness temperatures, this brightening corresponds to a temperature difference of about 15°K Other 5 μm features have also been observed to disappear or form over the course of a few rotations. These dramatic short-term intensity changes can most easily be accounted for by variations

FIGURE 10 - Short time scale variations on Jupiter at 5 μm. This figure shows the same longitude regions of Jupiter on two 5 μm images recorded ten Jovian rotations apart. Figure 10a was recorded at 03:00 UT 16 September 1973 with System I and System II central meridian longitudes (L_I and L_{II}) of 317° and 128°, respectively. Figure 10b was recorded at 05:46 UT 20 September 1973 with L_I = 330° and L_{II} = 108°. Both of these images were obtained when the seeing was less than one arcsec and are shown with north at the top and east at the right. This figure shows the formation of a bright feature about 12,000 km in diameter in the center of the Equatorial Zone.

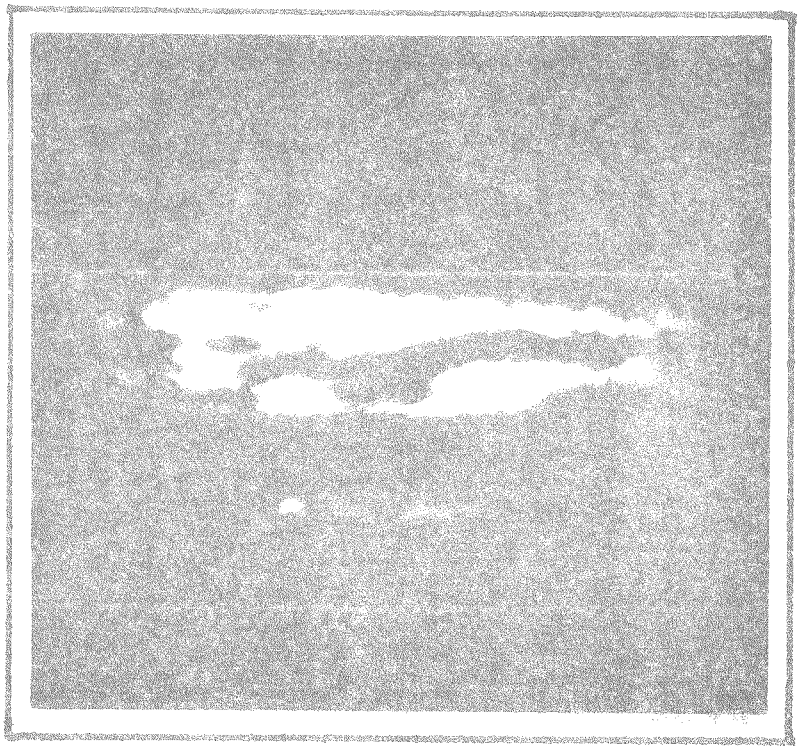

a

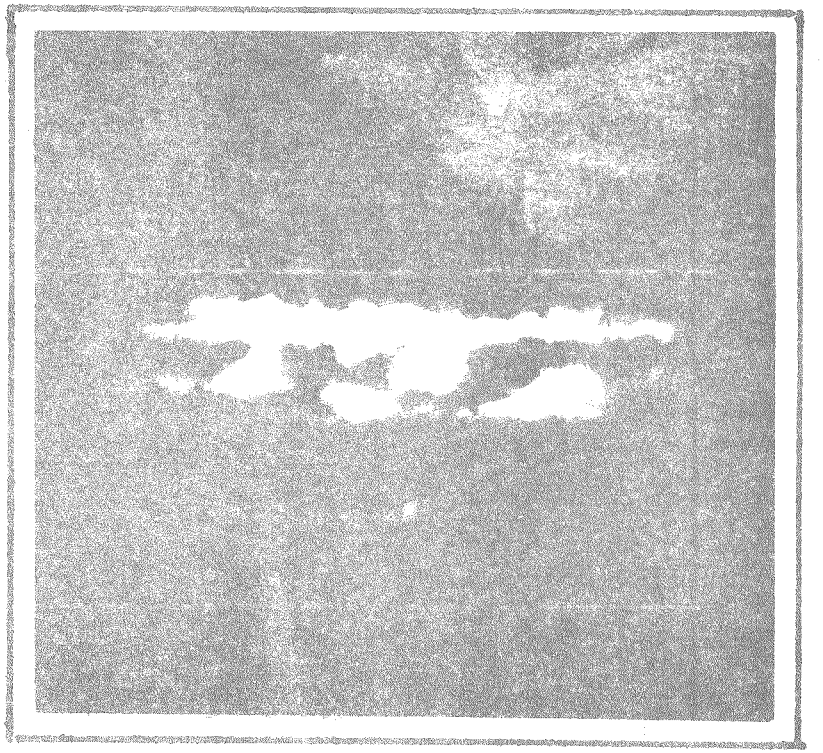

b

Figure 10

in the cloud opacity as a result of condensation or evaporation of an obscuring layer. Based on microphysical considerations, Rossow (1977) has calculated the time scales for precipitation of ammonia-water and ammonia-ice clouds on Jupiter, assuming cosmic abundances. These time scales are less than 3 hours and are consistant with the time scales for changes in cloud structure observed on Jupiter. A somewhat less satisfactory alternative to condensation and evaporation is that lateral motions of obscuring cloud layers account for the observed rapid 5 μm morphology variations. In order for features to be covered or uncovered by clouds, relative horizontal velocities of about 50 m/sec are required. These velocities are within the range of observed Jovian zonal velocities (Smith and Hunt, 1976), but in general, are not observed near variable areas. Cloud features adjacent to regions of rapid 5 μm variation do not exhibit such motions or shears, but remain relatively unchanged.

D. Flux Distribution

In this section the distribution of 5 μm emission from the disk of Jupiter is discussed. In a gross sense, belts correlate with warm regions, and zones correlate with cold areas. However, the detailed distribution is more complicated than this. Figure 11a illustrates the flux distribution in the equatorial area on UT 20 September 1973 as a flux-frequency histogram. These data are derived from 67 images and are divided into equal area partitions using only those pixels which have μ (cosine of the emission angle) greater than 0.95. Only equatorial data near the central meridian

FIGURE 11 - The flux-frequency histograms of Jupiter at 5 μm. In Figure 11a data from UT 20 September 1973 were divided into equal area partitions. The flux values from areas with $\mu > 0.95$ are plotted against the numbers of times such values occur. The area of observation includes the Equatorial Zone and the North and South Equatorial Belts. Sixty-seven images were used to cover 210° of longitude. Figure 11b is a similar plot of flux data from 21 images acquired on UT 4 October 1976. A small zero offset difference exists between the two sets of data causing a difference between the relative DN scale and the absolute calibration of each plot. Nevertheless, a trimodal flux distribution can be seen in both histograms.

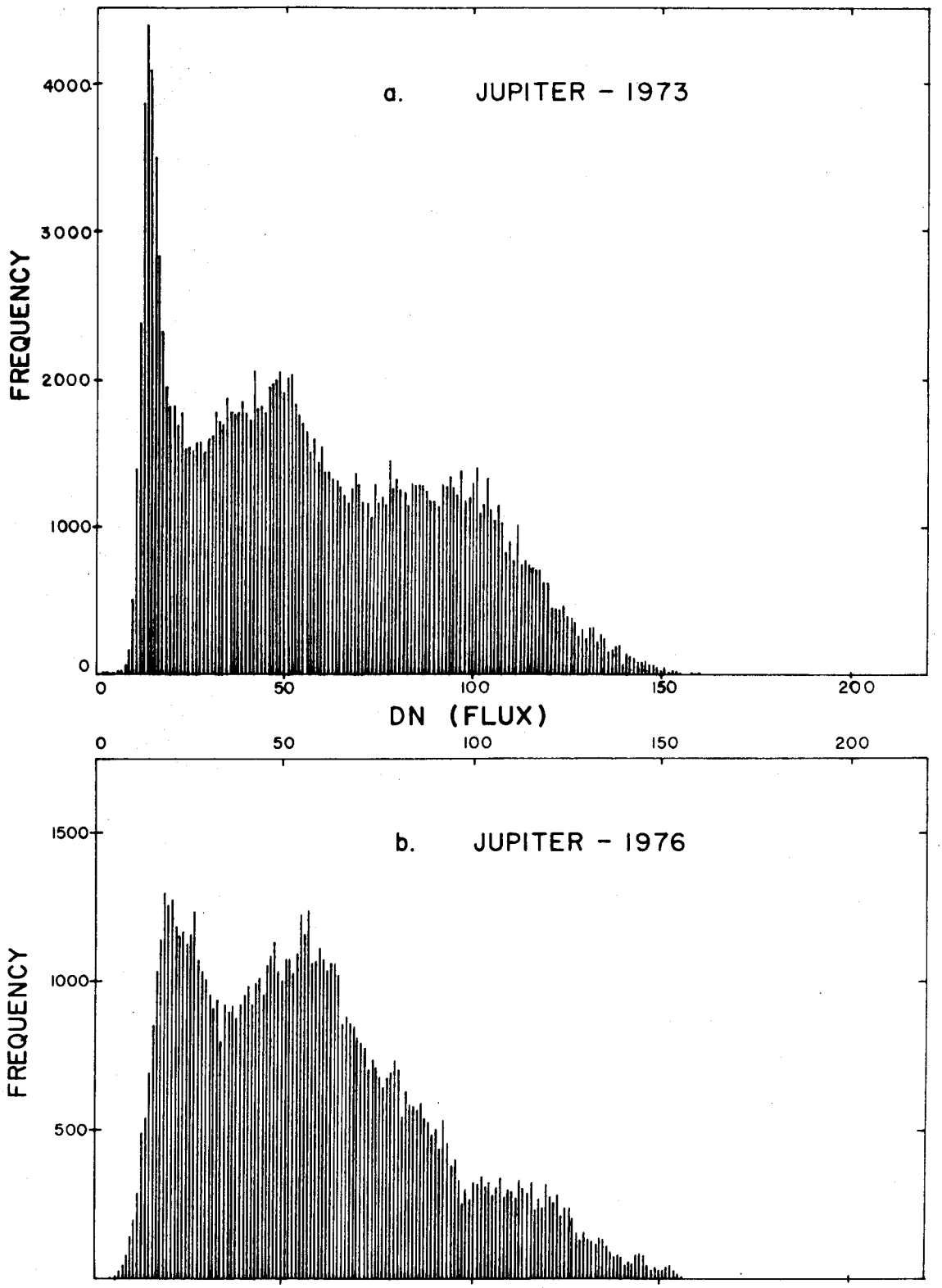
a. JUPITER - 1973
FREQUENCY
4000
3000
2000
1000
0
0
50
100
150
200
DN (FLUX)
b. JUPITER - 1976
FREQUENCY
1500
1000
500

Figure 21

were used in order to minimize the effects of limb-darkening. All frames were calibrated and corrected for atmospheric extinction. Due to planetary rotation approximately 210° of longitude in the Equatorial Zone and North and South Equatorial Belts are represented in Figure 11a. For comparison, a similar plot of data acquired on UT 4 October 1976 is shown in Figure 11b.

The histograms show a trimodal distribution of flux in the equatorial region. This means that there is a higher probability of detecting certain specific brightness temperatures than others. By detailed examination of the data, it can be seen that the highest and narrowest peak corresponds to the lowest level of flux coming from the Equatorial Zone. The middle peak corresponds to an intermediate flux level in the belts, and the hottest peak corresponds to the 5 μm hot spots in the belts.

Absolute brightness temperatures have been calculated by calibrating the flux measurements with standard stars. Figures 12a and 12b are a comparison of two brightness temperature-frequency histograms from 1973 and 1976. Figure 12a contains the same data as Figure 11a, but in this case the data are plotted as a function of brightness temperature instead of flux. Data from 32 images, recorded on UT 5 October 1976, were reduced in a similar manner as the 1973 data. Figure 12b is a plot of the 1976 brightness temperature distribution. Data are divided into 5°K wide bins with bin temperature values shown on the horizontal scale. The important point illustrated by this comparison is that three specific

FIGURE 12 - Comparison of brightness temperature frequency histograms of Jupiter from 1973 and 1976. Equal area partitions of the central region of the Jovian disk ($\mu > 0.95$) were sorted into 5°K wide bins (except for first bin) according to their brightness temperature. This was done for many frames so that a significant portion of one Jovian rotation is represented. The number of times a brightness temperature value is observed is plotted against the bin value. Figure 12a represents data from 67 frames recorded on UT 20 September 1973 and approximately 210° of longitude in the Equatorial Zone and North and South Equatorial Belts are represented. Figure 12b shows the same areas from 32 frames recorded on UT 5 October 1976 representint about 140° of longitude. In both histograms a trimodal distribution of brightness temperatures can be seen, however, the relative porportions of the peaks has changed somewhat.

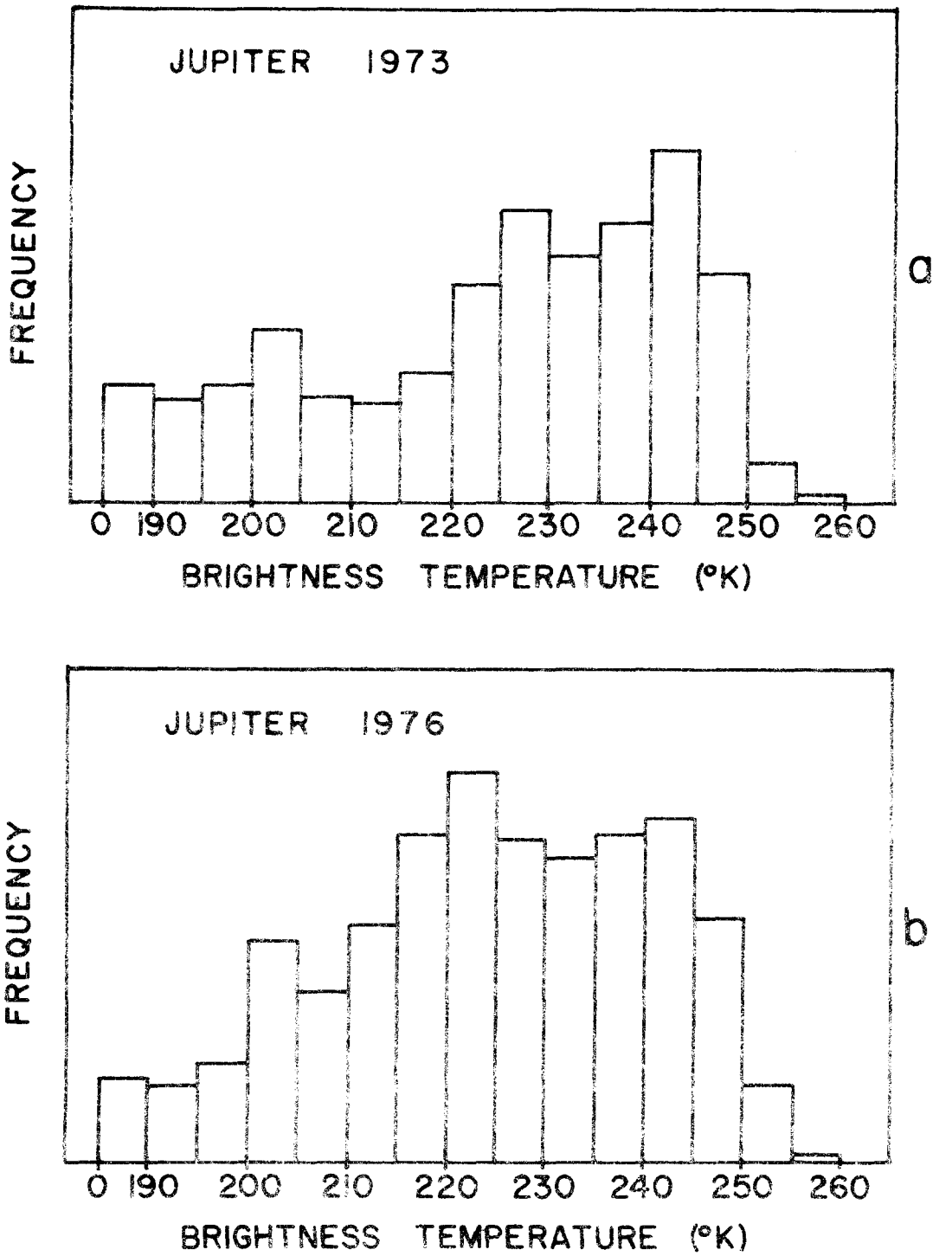
JUPITER 1973
FREQUENCY
a
0 190 200 210 220 230 240 250 260
BRIGHTNESS TEMPERATURE (°K)
JUPITER 1976
FREQUENCY
b
0 190 200 210 220 230 240 250 260
BRIGHTNESS TEMPERATURE (°K)

Figure 12

ranges of brightness temperatures are observed in unlimb-darkened 5 μm data, and this trimodal distribution is a long term feature of the flux distribution. Between 1973 and 1976 both the visible as well as 5 μm cloud morphology of Jupiter changed significantly. Nevertheless, the same values of most probable brightness temperatures are observed at every apparition. This implies that the trimodal nature of the flux distribution is a characteristic of the vertical cloud structure and not altered by horizontal redistribution of cloud material.

The areal distribution of the three temperature regimes is illustrated in Figures 13a, b, c, and d. Figure 13a and 13b are, respectively, a black and white copy of an Ektachrome slide taken at 08:49 UT 5 October 1976 and a 5 μm image recorded at 08:54 UT on the same date. The calibrated 5 μm image is displayed as a brightness temperature contour map in Figure 13c. The contour interval is 5°K with the lowest contour at 190°K and the highest at 255°K. Brightness temperature values of 215°K and 235°K correspond to the relative minima in the histogram data from the center of this 5 μm image. By using these specific values to define contour intervals, it is possible to illustrate the spatial distribution of brightness characterized by the three histogram peaks. Such an illustration is shown as Figure 13d. Because of limb-darkening the brightness temperature contours apply only to the center of the disk and only this region should be considered in the following discussion. Nevertheless, the previously discussed qualitative correlations of

FIGURE 13 -- The areal distribution of the three temperature regimes of Jupiter. Figure 13a is a black and white print of an Ektachrome slide taken at 08:49 UT 5 October 1976 with $L_I = 72^\circ$ and $L_{II} = 13^\circ$. Figure 13b is a 5 μm image recorded at 08:54 on the same date with $L_I = 75^\circ$ and $L_{II} = 16^\circ$. A calibrated contour map of this frame is shown in Figure 13c with a 5°K contour interval. The lowest contour is at 190°K and the highest at 255°K. Brightness temperature values of 215°K and 235°K correspond to the relative minima in the histogram data for the central region of this particular 5 μm frame. These values are used to define contours for Figure 13d. In this figure the black regions correspond to the coldest 5 μm areas with brightness temperatures of less than 215°K, while the gray regions correspond to the intermediate temperature features with brightness temperatures between 215 and 235°K. The hottest 5 μm features are represented as white areas with brightness temperatures greater than 235°K. These figures are oriented with north at the top and east at the right.

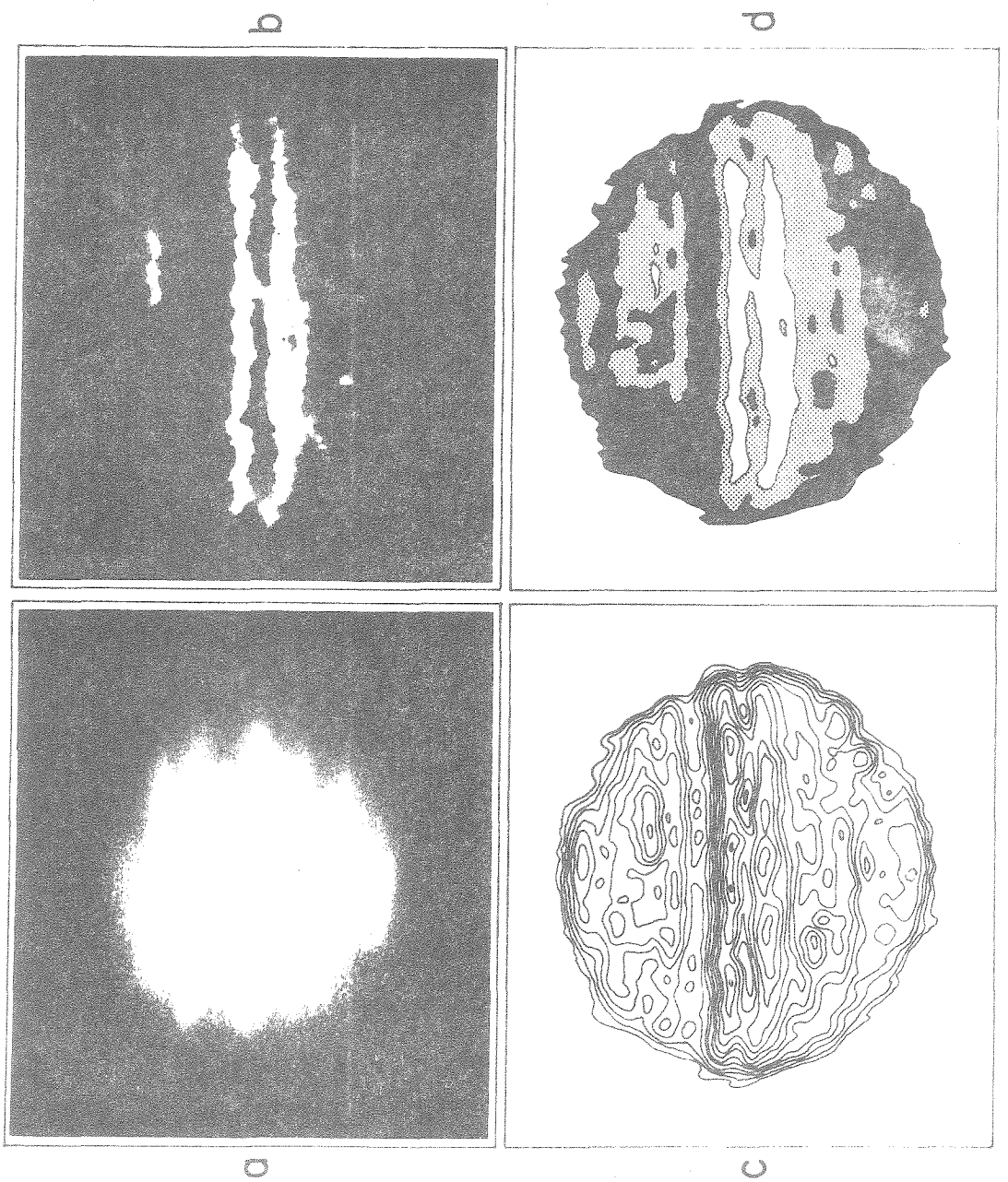

Figure 13

visible Jovian features with 5 μm brightness temperatures are exemplified by comparing Figures 13b and 13d. The hottest regions, with brightness temperatures of 240-260°K, correspond to the dark belt cores which are seen in visible photographs as blue-gray areas. These cores are surrounded by broad brown belt areas of intermediate brightness temperatures in the range of 215-235°K. The coldest regions with temperatures of 190-210°K are clearly delineated by the white zones and Great Red Spot. The polar regions emit 5 μm radiation with average brightness temperatures of about 215°K and maxima near 225°K, so they appear in the middle temperature category. However, these regions are near the limb and are thus observed at large slant angles. If the same limb-darkening law applies to the poles as the equatorial belts, then the mean polar 5 μm brightness temperature corrected for zero emission angle would be about 235°K, with maximum values near 247°K.

E. Limb-darkening

A study of the relative limb-darkening of different local features should provide further information on the nature of the 5 μm emission from Jupiter.

Limb-darkening measurements are made by selecting a region of interest on the disk and measuring its brightness as it rotates around the planet. This requires using many different images of Jupiter over several hours in order to construct one profile. This

technique has the advantage that limb-darkening curves can be obtained independently of longitudinal inhomogeneities, and may be applied to regions of relatively small spatial extent.

Figure 14, 15, 16, and 17 illustrate the differences in limb-darkening for various types of Jovian features. With the exception of Figure 17, each plot consists of combined data from several different localized features as they rotated across the disk. In all cases the data are plotted against the cosine of the local emission angle (μ) and are shown both in terms of brightness temperature and on a relative flux scale normalized to unity at μ=0.90.

The data shown in Figure 14 are from the hottest 5 μm areas seen in 1973 in the North and South Equatorial Belts and in 1974 in the North Equatorial Belt. The limb-darkening is quite steep and is characteristic of areas with brightness temperatures in the hottest histogram peak. Analysis of data from the Equatorial Belts during the 1975 and 1976 apparitions indicates that the hottest areas always follow this steep limb-darkening law independent of yearly changes in the flux distribution.

Figure 15 shows the limb-darkening for several bright 5 μm areas observed in the South Temperate Belt during the 1973 apparition. These data, as well as data from subsequent years, indicate that the hottest regions in high latitude belts have the same limb-darkening and the same brightness temperatures, at similar μ values, as the Equatorial Belts. In general, all 5 μm features with brightness

FIGURE 14 - 5 μm limb-darkening of Jupiter. Individual measurements of isolated hot areas in the North and South Equatorial Belts in 1973 and 1974 are plotted against the cosine of the emission angle (μ). As Jupiter rotates the emission angle changes and a limb-darkening profile is generated which is free from any affects of lateral inhomogeneities. These data are normalized on a relative flux scale to unity at $\mu = 0.9$. A brightness temperature scale is also provided on the right.

FIGURE 15 - Same as Figure 14 but for high latitude hot regions in the South Temperate Belt in 1973.

FIGURE 16 - Same as Figure 14 but for intermediate brightness temperature areas in the North Equatorial Belt in 1973.

FIGURE 17 - Average 5 μm limb-darkening of a Jovian zone. In order to achieve an adequate signal-to-noise ratio in low flux regions 34 images, acquired on UT 29 August 1974, were registered and averaged together pixel by pixel. This figure shows the limb-darkening data from the South Tropical Zone in the averaged data. For this purpose longitudinal homogeneity was assumed and an average limb-darkening profile is shown.

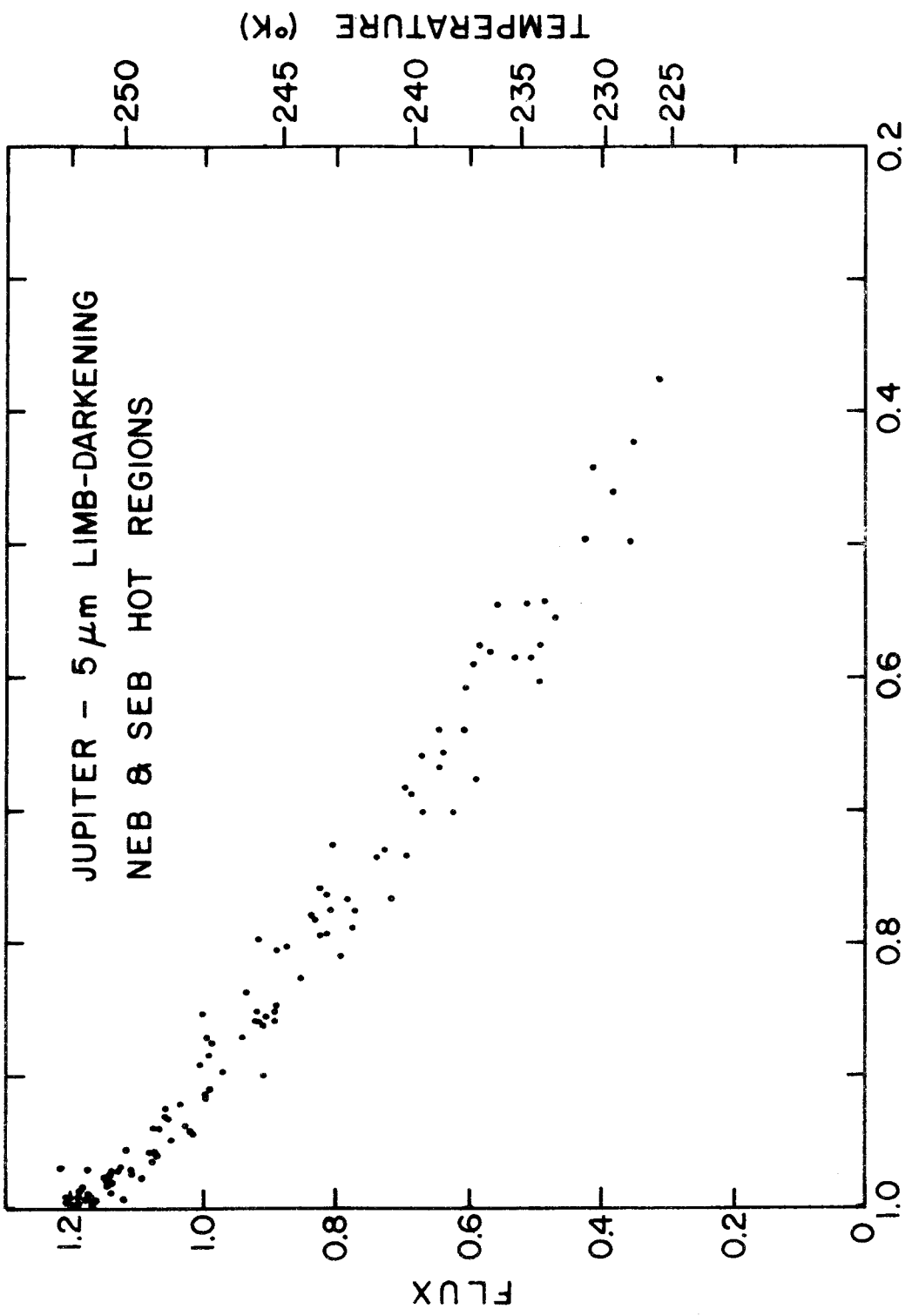
JUPITER - 5 μm LIMB-DARKENING
NEB & SEB HOT REGIONS
TEMPERATURE (°K)
250
245
240
235
230
225
FLUX
1.2
1.0
0.8
0.6
0.4
0.2
0
1.0
0.8
0.6
0.4
0.2
μ

Figure 14

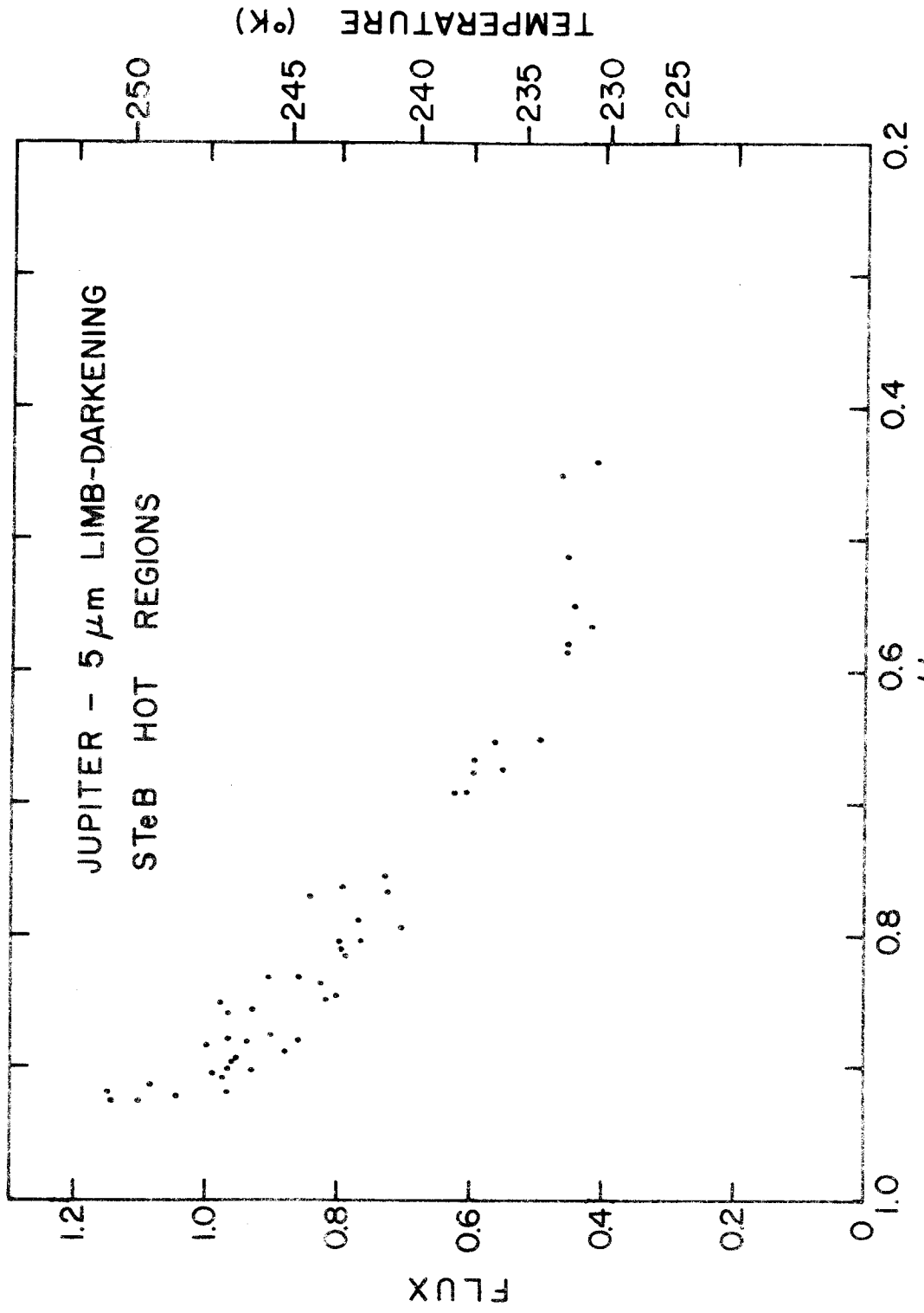
JUPITER - 5 μm LIMB-DARKENING
STeB HOT REGIONS
TEMPERATURE (°K)
250
245
240
235
230
225
FLUX
1.2
1.0
0.8
0.6
0.4
0.2
0
1.0
0.8
0.6
0.4
0.2
μ

Figure 15

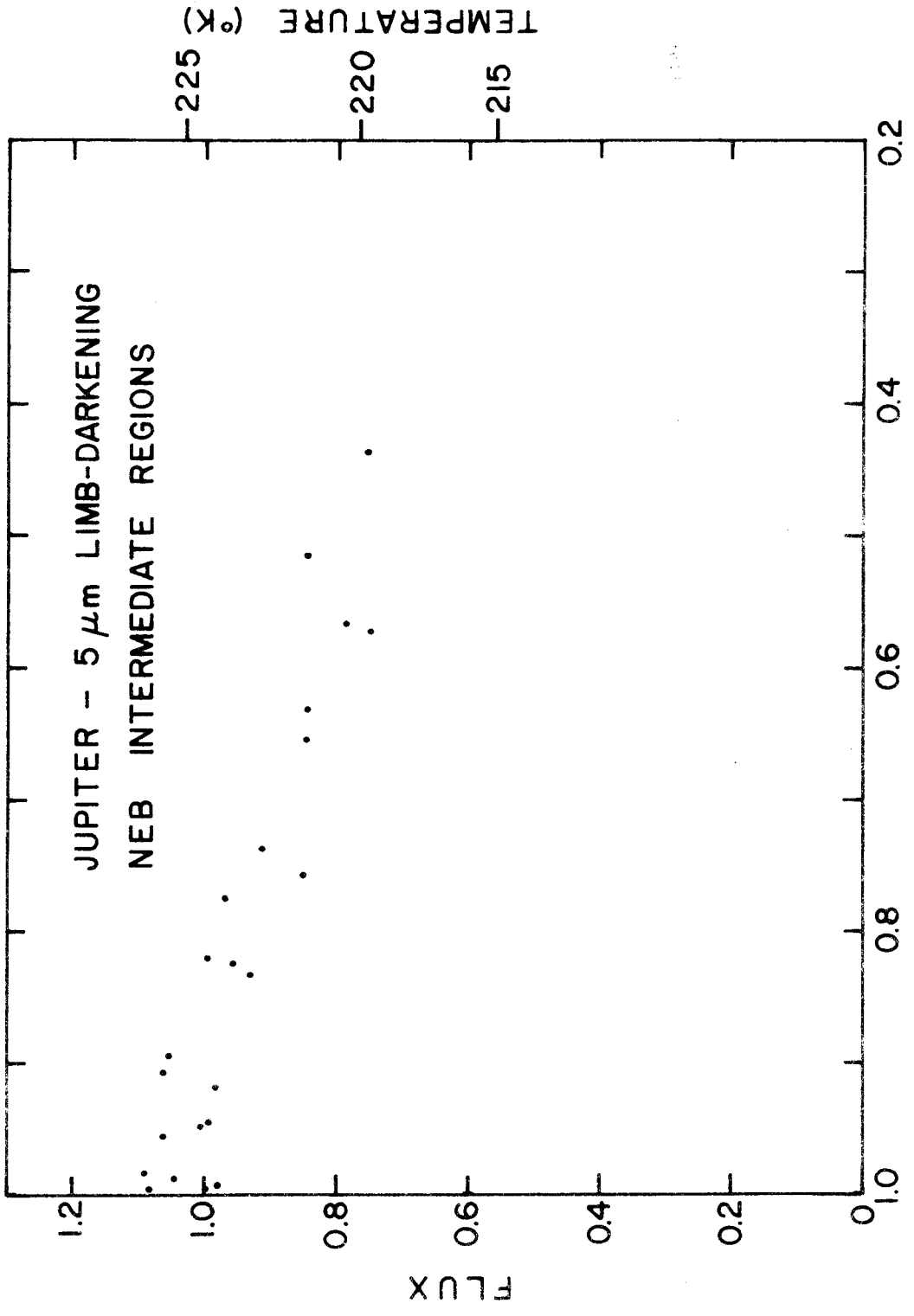
JUPITER - 5 μm LIMB-DARKENING
NEB INTERMEDIATE REGIONS
TEMPERATURE (°K)
225
220
215
FLUX
1.2
1.0
0.8
0.6
0.4
0.2
0
1.0
0.8
0.6
0.4
0.2
μ

Figure 16

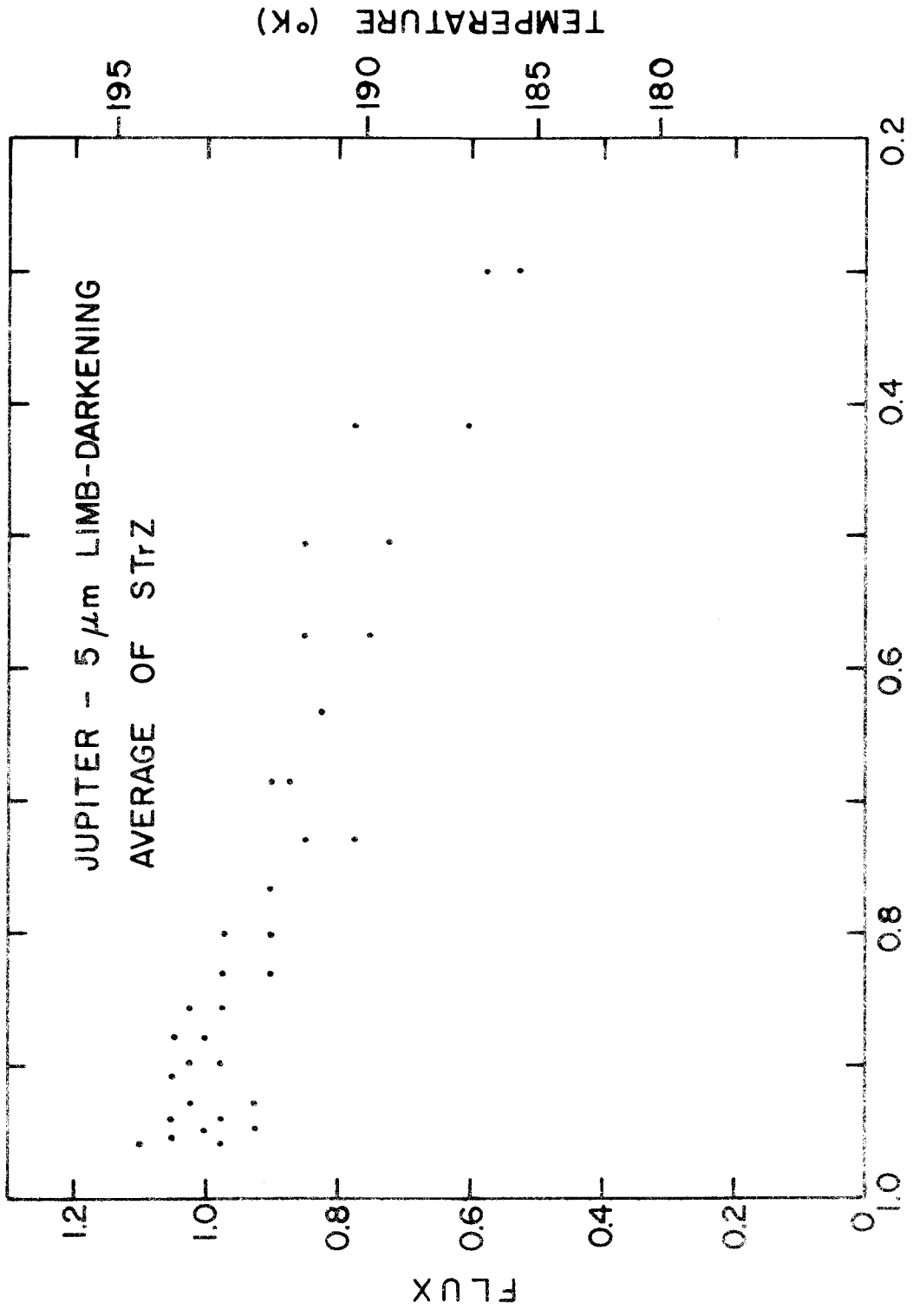
JUPITER - 5 μm LIMB-DARKENING
AVERAGE OF STrZ
TEMPERATURE (°K)
195
190
185
180
FLUX
1.2
1.0
0.8
0.6
0.4
0.2
0
1.0
0.8
0.6
0.4
0.2
μ

Figure 17

temperatures (measured such that they are unaffected by limb-darkening) corresponding to the hottest flux-frequency histogram peak, have a blue-gray visible appearance and exhibit the steep limb-darkening characterized in Figures 14 and 15.

The limb-darkening of intermediate flux regions in the North Equatorial Belt in 1973 is plotted in Figure 16. These regions correspond to brown areas on simultaneous color photographs and have brightness temperatures in the range of the middle histogram peak. These data display considerably less limb-darkening than the adjacent equatorial hot regions. As was true for the hottest regions, yearly changes in flux distribution do not affect the shape of the limb-darkening curve of intermediate 5 μm features.

Figure 17 shows the limb-darkening profile for the South Tropical Zone in 1974. Due to the low level of emitted 5 μm flux from the zone, data from 34 images were added together to increase the signal to noise ratio. For this purpose longitudinal homogeniety was assumed and an average limb-darkening profile is shown. Zonal limb-darkening is relatively mild and is similar to the behavior shown by intermediate belt regions.

Because reflected solar radiation could be a major contribution to the low levels of observed 5 μm flux in the Jovian zones, it is difficult to assign a meaningful brightness temperature. However, by assuming that all of the observed radiation is due to thermal emission, a value less than 194°K is obtained for the South Tropical

Zone in 1974. At the other extreme, we may assume that all of the observed flux is reflected sunlight and calculate an albedo necessary to account for the measured brightness. A perfectly diffusing surface with an albedo of unity will reflect 5 μm radiation equivalent to the thermal flux from a 209°K blackbody at the distance of Jupiter. Therefore, a geometric albedo of 0.4 is needed to give an equivalent brightness temperature of 195°K. Infrared reflectivity data from Hovis and Tobin (1967) for water clouds and from Kieffer (1975) for ammonia ice crystals indicate that the single scattering albedo at 5 μm is less than 0.3 for such cloud materials. Therefore, reflected sunlight could account for the entire observed zone flux if the albedos of Jovian clouds are somewhat greater than those observed in the laboratory and for terrestrial clouds. More precise limits on the zone cloud reflectivities and transmissions will be discussed in a subsequent section by analyzing 5 μm spectral line desaturations.

F. Comparisons of 5, 20, and 45 μm Jupiter Images

At 02:25 UT 4 December 1973 Pioneer 10 encountered Jupiter and acquired infrared images in two spectral channels centered at 20.0 and 45.4 μm and having equivalent widths of 11.6 and 22.7 μm, respectively (Ingersoll et al. 1975). Approximately 3 hours earlier the same area of Jupiter was imaged from the ground at 5 μm. In this section these near simultaneous images are compared.

Figures 18a, b, and c show three images of the same area of Jupiter at 5, 20, and 45 μm, respectively. The sub-Earth latitude and System I longitude are -0.3° and 66° for the 5 μm image and the sub-spacecraft latitude and System I longitude are -11.3° and 57° for each of the Pioneer frames. Features visible in the 5 μm image correlate to a greater degree with the 45 μm data than with the 20 μm data. This is particularly true in the equatorial area. The South Equatorial Belt shows a strong longitudinal inhomogeneity, visible as a dark band in the rising (west) limb of the 5 μm frame. If this dark band at 5 μm is interpreted as a cold obscuring cloud layer over the otherwise warm belt than the 5 μm-45 μm correlation indicates that this cloud must be cold enough to influence the 45 μm data. Orton and Terrile (1978) use this correlation to estimate the degree of partial cloud cover over the belt under the assumption that the same level of the atmosphere affects both the 5 μm and 45 μm emission. If this is true then the cloud top temperature of this cold obscuring region must be comparable to the measured 45 μm temperature of 140°K (Orton, 1975a). Five micrometer cloud features, on the other hand, do not correlate well with the 20 μm image which comes from a higher level in the atmosphere and has a brightness temperature of about 125°K.

G. Spectroscopic Results

In order to use both imaging and spectroscopic data sets most accurately, they must be compared in a complementary manner. Since the projection of the entrance aperture of the spectrometer

FIGURE 18 - Comparison of 5 μm images of Jupiter with 20 and 45 μm images from Pioneer 10. Figure 18a is a 5 μm image recorded at 23:57 UT 3 December 1973 with a sub-Earth latitude and System I and II longitudes of -0.3°, 66° and 356°, respectively. The Pioneer 10 images were each acquired at 02:25 UT 4 December 1973 from a distance of about 3.4 Jovian radii and with a sub-spacecraft latitude and System I and II longitudes of -11.3°, 57° and 345°, respectively. The 20 and 45 μm images are shown as Figures 18b and c, respectively. North is at the top and east at the right.

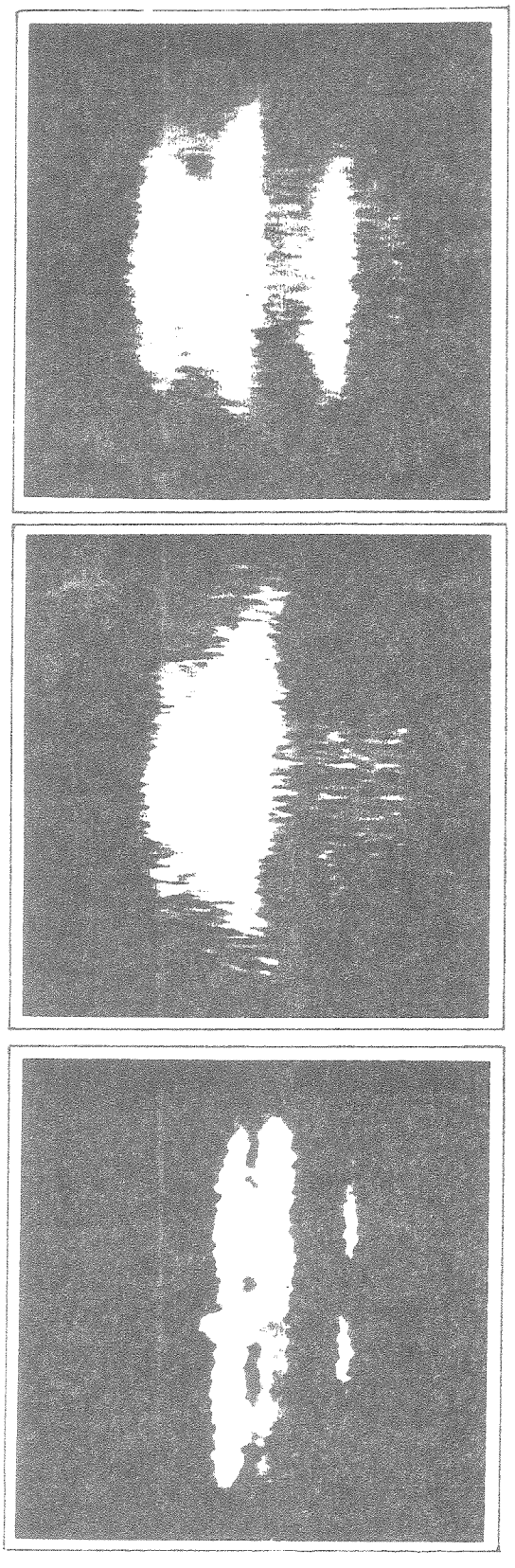

Figure 18

was 20 arcsec, and Jupiter had a mean diameter of 44 arcsec, only about 25% of the disk was observed. Furthermore, spectroscopic integrations lasted as long as 15 minutes, during which Jupiter's central meridian longitude changed by about 9° or moved about 7 arcsec across the aperture. In order to match the spectroscopic coverage, 5 μm imaging frames are selected with central meridian longitudes within those observed in spectroscopic integrations, and only data within the central 20 arcsec are used for comparisons. For measuring mean brightness temperatures and flux distributions, the imaging frames are added in such a way as to weight each point on the disk by its time and position in the spectroscopic aperture. In this way, it is possible to construct a spatially resolved flux distribution for the total area observed spectroscopically. Figure 19 is a brightness temperature histogram of the area coinciding with the field of view of the spectrometer during run number 1140. Each point represents the number of equal area partitions of the field of view with brightness temperatures within 5°K wide bins with brightness temperature values shown on the horizontal scale. Since these data came from the central 25% of the area, the temperature smearing effects of limb-darkening are minimized. However, the effects of atmospheric seeing and of cloud structure smaller than the resolution element still influence the shape of this curve. Nevertheless, the typical tri-modal distribution is apparent, with central brightness temperatures occurring at 202, 225 and 250°K, and with a maximum brightness

FIGURE 19 - The brightness temperature histogram of Jupiter corresponding to spectroscopic observations. The solid lines in this figure consist of histogram data acquired on UT 4 October 1976 from the central 25% of the disk and coincides with the field of view of the spectrometer on run number 1140. Each solid bar represents the number of equal area partitions of the field of view with brightness temperatures in 5°K wide bins (except the first bin). The observations are interpreted as consisting of three components, as shown by the dashed lines. The A's refer to the area under each dashed curve and the subscripts to the mean brightness temperature of each.

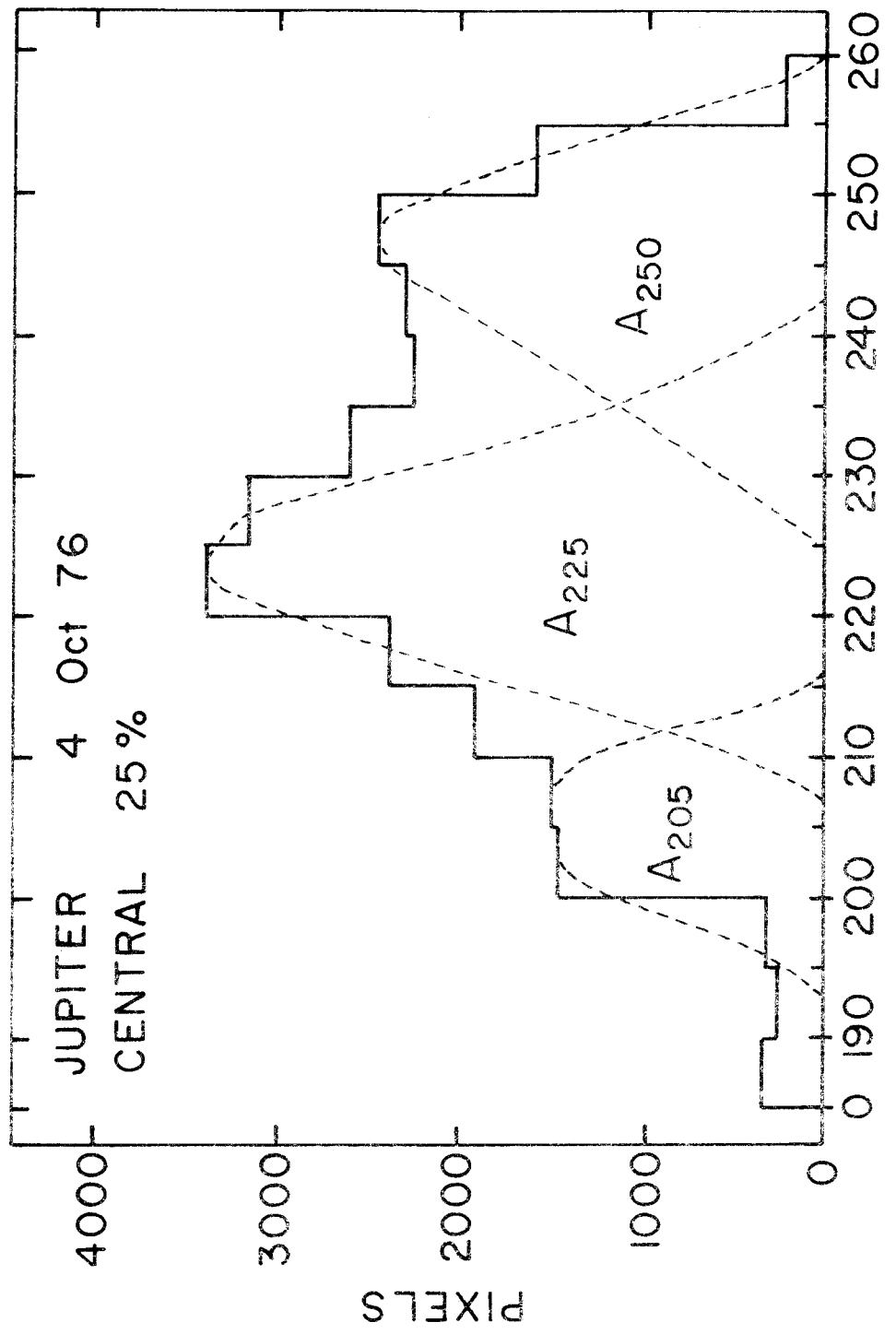
JUPITER 4 Oct 76
CENTRAL 25%
A_{205}
A_{225}
A_{250}
PIXELS
0
1000
2000
3000
4000
0 190 200 210 220 230 240 250 260
BRIGHTNESS TEMPERATURE (°K)

Figure 19

temperature of 258.0°K. The dashed lines represent the separation of the maxima in the distribution into discrete contributions which are assumed to have different physical origins within the atmosphere. The justification for this is that histograms from areas with different central meridian longitudes all show this trimodal distribution, but differ slightly in the relative amplitude of the peaks.

(i) Spectroscopic Cloud Temperatures

The spectroscopic microwindow calibrations were used to derive values for the radiance of Jupiter. These results are plotted in Figure 20, with the radiances converted to brightness temperature for compatability with the histograms of spatial brightness temperature distribution. The brightness temperatures are averaged only over 2 cm^{-1} (comparable to the size of the dots in Figure 20). The points are joined together only to make identification with run number possible, with no implication as to the value of brightness temperature between the points intended. In fact, intermediate values are indeterminate from these data. Consequently, the broad dip at 2112 cm^{-1}, for instance, occurs because that frequency happens to coincide with a major Jovian absorption feature, the P11 manifold of ν_2 CH_3D (Beer and Taylor, 1973; 1978a). That is, the 14 microwindows were chosen for the clarity of the Earth's atmosphere and less than half of the channels coincide with a Jovian microwindow. The points believed to be free of line absorption (but not, of course,

FIGURE 20 - The brightness temperature of Jupiter in selected spectroscopic regions. Each point represents a brightness temperature measurement in a 2 cm^{-1} wide region in the 5 μm window averaged across the central 25% of the planetary disk. The points are joined for identification only and are not intended to imply a trend. Values labeled by vertical arrows are in regions believed to be free from Jovian line absorption. The increase scatter in the points at low frequency a consequence of a declining signal-to-noise ratio. These data were collected by R. Beer on UT 3 October 1976.

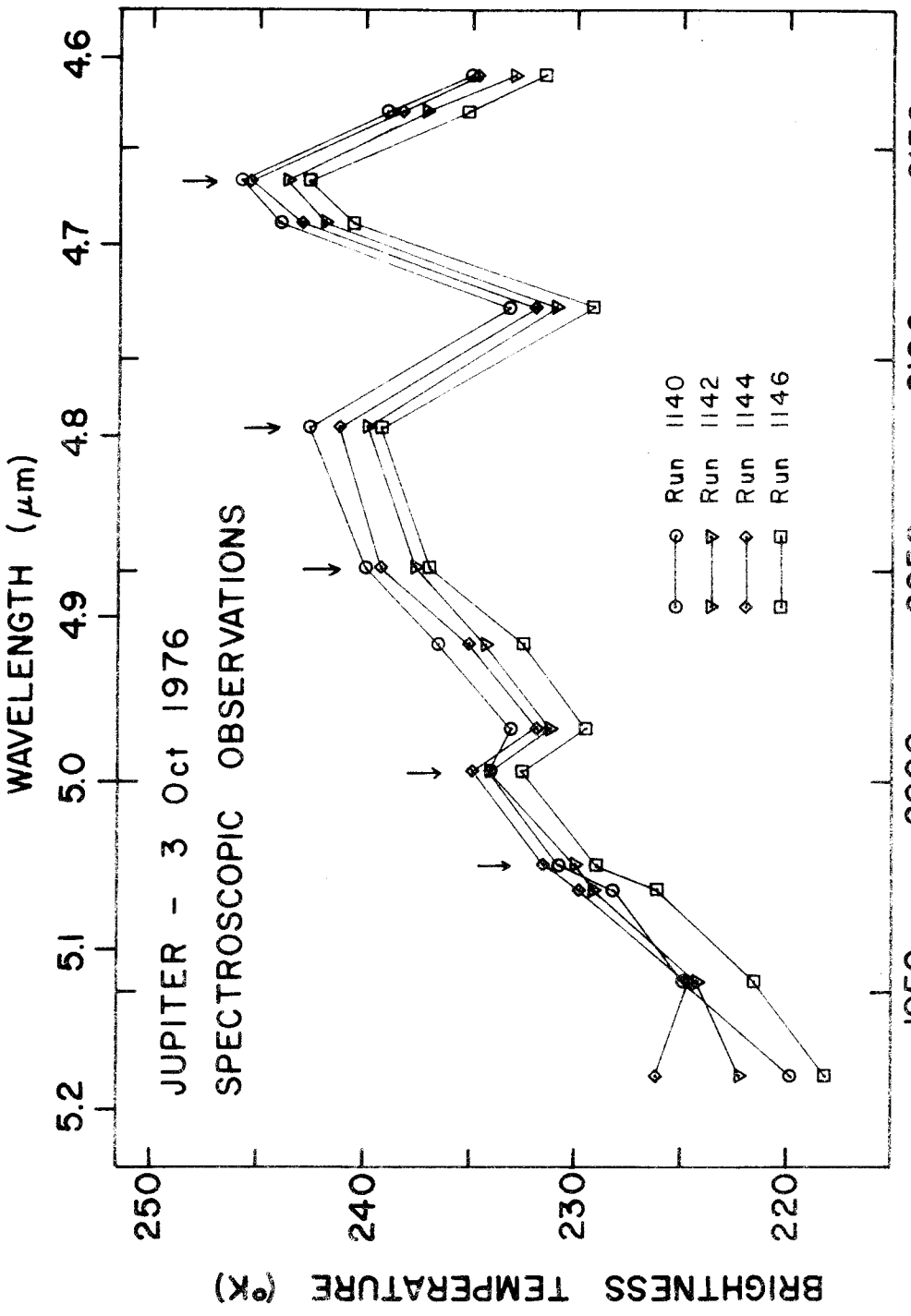
WAVELENGTH (μm)
5.2
5.1
5.0
4.9
4.8
4.7
4.6
JUPITER - 3 Oct 1976
SPECTROSCOPIC OBSERVATIONS
Run 1140
Run 1142
Run 1144
Run 1146
BRIGHTNESS TEMPERATURE (°K)
250
240
230
220
1950
2000
2050
2100
2150
FREQUENCY (cm⁻¹)

Figure 20

continuum absorption) in Jupiter are indicated by the vertical arrows in Figure 20. The general rise in brightness temperature toward 2142 cm^{-1} seems to be real and is probably a result of the wing of the NH_3 ν_4 band. The strong cut-off at short wavelength is also real and is due to the CH_4 ν_3 band. The data in Figure 20 indicate that the deepest penetration into the Jovian lower atmosphere is made at 2142 cm^{-1}.

Table 4 gives the mean and maximum brightness temperatures for the histogram most closely coinciding with the central meridian longitude of the spectral data. Brightness temperatures measured from the spectroscopic data are consistently greater than the mean brightness temperatures from the 5 μm histograms. The variability with longitude is well correlated between the two different types of observations. This suggests that at least some of the spread in brightness temperatures of each point is real and not an artifact of the calibration procedure.

Various factors could be responsible for the differences in the average brightness temperatures derived from the imaging and spectroscopic data. There may be a difference in the calibration of both data sets, or the time variations may have been greater than assumed, or the positions of the spectroscopic calibration points may be coincidental with very clear regions in the Jovian spectrum (or some combination of all three). The imaging broad-band filter effective frequency of 2070 cm^{-1} does not coincide with any spectroscopic microwindow, but does, fortunately, fall between two points at

TABLE 4

JOVIAN BRIGHTNESS TEMPERATURES CORRESPONDING TO SPECTROSCOPIC MEASUREMENTS

Run Number	Histogram T_B (^oK)*	
	Mean	Max
1140	225.9	258.0
1142	224.5	251.5
1144	225.9	253.2
1146	225.5	251.1

* Brightness temperatures from histograms with a similar viewing geometry as spectroscopic runs and for an effective frequency of 2070 cm^{-1}. These values are calibrated absolutely to $\pm 2^oK$, and have relative errors of $\pm 0.2^oK$

2051 and 2084 cm^{-1} that are both in clear regions (i.e., they are Jovian continuum points). A linear interpolation between the two might, therefore, be a realistic estimate of the continuum value at 2070 cm^{-1}. Using this, a brightness temperature of 239.7 ± 2.0°K is found, averaged across 25% of the projected area of the disk. Performing a similar spatial averaging of the imaging data, a brightness temperature of 225 ± 1°K is obtained. The difference is substantial, corresponding to a factor of 2.2 in effective radiance. This discrepancy is too large simply to arise from a calibration error or time variability alone. In part at least, it is undoubtedly a consequence of absorption in the Jovian atmosphere integrated over by the broad-band filter, but not allowed for in the derivation of the effective brightness temperature at 2070 cm^{-1} from the spectroscopic data. Leaving this problem aside, the general trend of brightness temperature with frequency is little affected by calibration errors even as large as the one suggested here, because the points are calibrated collectively, not individually. The major consequence of a change in calibration precedure would be to move the entire set of curves up or down with little change in slope. Peak temperatures, then, are about 5°K higher than the value derived from the broad-band data. It is conjectured that were it possible to perform the imaging with a filter of 2 cm^{-1} width, centered at 2142 cm^{-1}, brightness temperatures within a hot-spot would be raised by a similar amount. Thus, assuming the shape of the spectral

window does not change as a function of total flux, the brightness temperatures of the warmest hot-spots exceed 265°.

Independently of flux calibrations, Beer and Taylor (1978a) have determined the rotational temperatures of Jovian CH_3D from these same measurements, and derive 220 ± 20°K. The effective temperature for a clear column of uniformly mixed gas is defined by:

$$\theta_e = \frac{\int_{z_o}^{\infty} \theta(z)u(z)dz}{\int_{z_o}^{\infty} u(z)dz} \qquad (2)$$

where u(z) and θ(z) are the absorber abundance and temperature at height z, respectively. θ_e is equal to 220°K for a $\theta(z_o)$ equal to 270°K. In other words, the rotational temperature is consistent with a model which has an effective cloud top (either a discrete upper boundary, or optical depth unity in a diffuse cloud) in the range 270 ± 20°K. This agrees well with the direct flux calibration temperatures, and is entirely consistent with the cloud model to be presented in a later chapter.

(ii) Cloud Albedos and Spectral Line Saturation

It is found that there are several lines in each of the 5 μm spectra which appear to be saturated or nearly saturated. This phenomenon appears to be real and was also found in earlier spectra. Figure 21a shows a portion of the 5 μm spectrum of Jupiter, run

FIGURE 21 - Spectral saturation of Jovian features. A portion of the 5 μm spectrum of Jupiter collected by R. Beer on UT 3 October 1976 (run number 1146) near the P5 manifold of CH_3D is shown in Figure 21a. This unblended Jovian feature shows strong saturation in all spectra obtained. Figure 21b shows a set of synthetic spectra of the same wavelength region. These curves were computed by F.W. Taylor using a technique described by Beer and Taylor (1978b) and are shown as a function of mean Jovian cloud reflectivity in the field of view of the spectrometer. Comparison of the observed and synthetic spectra, in the most saturated region of the CH_3D manifold, show that if the mean Jovian cloud reflectivity were about 0.2 or greater, reflected solar flux would desaturate the observed spectrum.

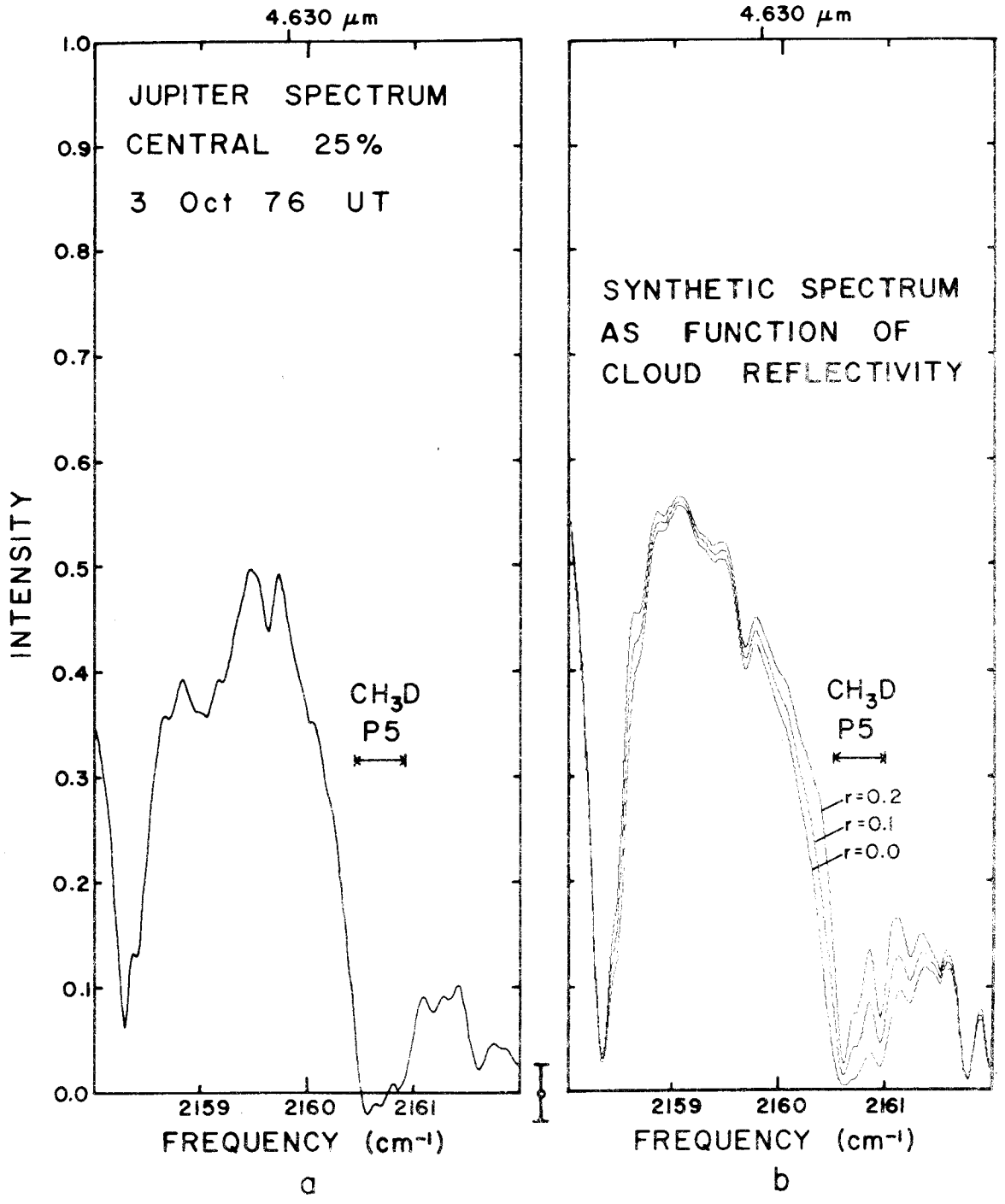
4.630 μm
JUPITER SPECTRUM
CENTRAL 25%
3 Oct 76 UT
INTENSITY
1.0
0.9
0.8
0.7
0.6
0.5
0.4
0.3
0.2
0.1
0.0
CH3D
P5
2159
2160
2161
FREQUENCY (cm-1)
a
4.630 μm
SYNTHETIC SPECTRUM
AS FUNCTION OF
CLOUD REFLECTIVITY
CH3D
P5
r=0.2
r=0.1
r=0.0
2159
2160
2161
FREQUENCY (cm-1)
b

Figure 11

number 1146, near the P5 manifold of CH_3D. This line, as well as 3 others appear saturated in each of the 4 spectra acquired on this observing run. This spectral feature was chosen because it shows the fullest saturation of any of the unblended Jovian features. Figure 21b is a set of synthetic spectra of the same region as a function of reflectivity over the field of view. These synthetic spectra were computed using the same technique described by Beer and Taylor (1978b). It can be seen that the contribution of reflected solar radiation tends to desaturate the lines. From the limit on the degree of desaturation allowed by the observations, the maximum allowable cloud reflectivity can now be computed. By looking at the zero source signal in the observed spectra, a peak noise of 0.05 times the calibrated full scale value is measured. It is found, when comparing synthetic spectra with measured spectra in the region of saturated lines, that synthetic spectra with computed cloud reflectivities greater than 0.17 fall above the peak-to-peak noise envelope for the measured spectra. This gives a maximum mean cloud reflectivity, averaged over the whole field of view, of 0.17 with better than a 3σ certainty. Using all the saturated lines in all of the spectra this limit can further be reduced to about 0.09. By using the knowledge of the spatial flux distribution over the field of view from brightness temperature histograms, further improvement can be made on the cloud reflectivity limits. During this period of observations 24% of the total area in the field of view radiated with a

brightness temperature less than 210°K, and in a peak centered about 203°K. This area corresponds to the white zone-like regions near the equator which if presumed to be the tops of a layer of NH_3 clouds, will have brightness temperatures much colder than 190°K (Trafton and Stone, 1974). Assuming this to be true, then a reflectivity of 0.63 is required for this region if all of the radiation emitted from these white clouds at 5 μm is reflected solar flux. However, even if all of the reflected energy from Jupiter is backscattered from these regions their reflectivity cannot exceed the maximum mean reflectivity derived above, divided by their fraction of the field of view (i.e., 0.09/0.24) or 0.36. A mean reflectivity, for the white zones, greater than 0.36 would result in detectable desaturation of the CH_3D lines observed spectroscopically. This means that depending on the exact reflectivity of this area (between 0.36 and 0.00), between 45 and 100 percent of the radiation observed from the zones must be transmitted through the upper cloud if the upper cloud is assumed to be NH_3. All of this information will be assimilated in the next chapter to constrain positions and optical depths of clouds in an atmospheric model.

CHAPTER V

DISCUSSION

In this chapter the observational data presented in the previous chapter are assimilated into an atmospheric model of the vertical and horizontal cloud structure of the Jovian atmosphere. Evidence supporting multiple cloud layers is discussed and a three layer cloud model is developed. Spectroscopic and limb-darkening measurements provide constraints on the physical properties of the Jovian clouds.

A. Evidence of Cloud Layering

The large differences in measured 5 μm brightness temperature from location to location on Jupiter may be explained by the masking of hot, lower levels of the atmosphere by cold, optically thick clouds. This requires the overlying clouds to be present in a non-uniform manner over the disk. Specifically, high, cold clouds must be present over the zones to block nearly all of the 5 μm flux from lower levels. Belts appear hotter because they are relatively free from these high clouds. Likewise the observed warm polar regions must also be areas of clear upper atmosphere at 5 μm.

The lowest brightness temperatures measured at 5 μm of about 194°K corresponded to the South Tropical Zone and give a good upper limit to the upper cloud top temperature. This low value for the upper limit, combined with other observational and theoretical results suggest that these upper clouds are composed of ammonia (NH_3) ice. Lewis (1969) and Weidenschilling and Lewis (1973), starting

with a Jovian atmospheric composition similar to solar abundance, showed that a cloud layer of NH_3 ice is expected to form with a base condensation temperature of about 140°K. This temperature is also consistent with brightness temperatures measured on Jupiter by Pioneers 10 and 11 (Ingersoll et al., 1976) at 45 μm, and coincidental with a zonal cloud level derived from thermal structure calculations by Orton (1975b). Measurements by Anderson and Pipes (1971) further support the NH_3 ice cloud hypothesis by demonstrating a strong agreement between the shape of the Jovian ultraviolet geometric albedo between 1800 and 1950Å, and that of layers of gaseous and solid NH_3 over a gray surface. Using the Pioneer 10 photopolarimeter data, Coffeen (1974) calculates the relative heights of the cloud tops from a simple model of Rayleigh scattering above a Lambertian cloud layer. The result is that white zones and Great Red Spot were found to be elevated by as much as 15 km with respect to the belts. This is indicative of a high cloud layer present only over the zones. The formation of high NH_3 ice clouds over the zones is also consistent with the dynamics model of Ingersoll and Cuzzi (1969), where warm gas rises in the zones to condense clouds and cold gas sinks in the relatively clear belts.

Evidence of other cloud layers comes from the 5 μm flux-frequency histogram. One interpretation of the histogram's trimodal nature is that the peaks are due to three different cloud layers of a different condensation temperatures and therefore different

compositions. The uppermost cloud uniformly covers only the white zones, while the brown belts are covered by a patchy lower cloud whose breaks give observational access to an even deeper layer which appears blue in the visible. The long term persistence of the trimodal nature of the histograms, in spite of the large scale variations in horizontal cloud distribution, is further evidence that the sources of the peaks are a long term stable vertical cloud feature. It will be shown later that a three layer cloud model fits all the imaging and spectroscopic 5 μm data.

The relatively short time scales involved in changes over large areas ($\sim 10^4$ km across) in the 5 μm flux also support the multilayer cloud model. These changes occur when clouds condense or evaporate over a large area. If, on the other hand, 5 μm opacities are caused by something other than cloud layers (i.e., the atmosphere of Jupiter may not be entirely transparent in the 5 μm window), then unreasonably rapid variations in the atmospheric thermal structure would have to be invoked in order to explain the observed 5 μm fluctuations.

An alternative interpretation of the peaks in the histogram is that they are indications of differential cloud opacity and not layering. A distribution of cloud density or of areal density of holes in clouds could give the same result with only one cloud layer. The observed trimodal flux distribution would mean, however, that there are preferred optical densities or cloud configurations. This is probably unlikely, but the possibility

cannot be ruled out. Nevertheless, the conclusion that NH_3 clouds are present primarily over the zones and not over the belts or polar regions, still holds.

B. 5 μm Cloud Model

It is useful to combine all the observational results into a cloud model for the deep Jovian atmosphere. By making some reasonable assumptions, simple mathematical expressions for the 5 μm limb-darkening and cloud parameters are derived and serve as a preliminary model for the vertical cloud structure. This model is valuable in studying the Jovian meteorology and in analysis of spectral data to obtain the composition of the atmosphere. Further observations at 5 μm, as well as at other wavelengths, can then be used to further refine this initial representation of the deep Jovian atmosphere.

The trimodal nature of the brightness temperature histograms offers the strongest evidence to justify modeling the atmosphere as multiple layers of clouds, each having an independent set of physical parameters. Since the highest 5 μm brightness temperatures are consistently between about 260-270^{o}K and absorption by ammonia, methane or hydrogen gas are not expected to be the major sources of 5 μm opacity at these atmospheric levels, it is reasonable to assume that the highest levels of emission come from particles in the top of a dense cloud deck. Therefore, in a multi-layer cloud model the lowest level is always a uniform optically thick cloud which limits the highest observable brightness

temperatures. If a simple two-layer cloud model is used to explain the trimodal nature of the observational data then it is necessary to make the assumption that the upper layer has at least three preferred values of optical thickness. There is no observational or physical basis for such an assumption. It seems more likely that multiple cloud layers are responsible. With this assumption, a three-layer cloud model is the simplest which can be constructed while retaining consistency with the observational data.

For the purpose of these cloud models, let each layer be characterized by a fractional cloud cover f, a mean optical thickness for the cloudy portions τ, and a mean cloud top temperature T. In the case of a three layer model, the deepest layer is defined as having f equal to unity and τ equal to infinity. Furthermore, under the assumption that the white zone clouds are composed of ammonia ice, then the cloud top temperature of the uppermost cloud layer can be set as $T_1 = 140^{\circ}K$. Such a low temperature generates negligible emission at 5 μm, making the cloud model insensitive to this parameter. The remaining undetermined parameters are f_1, f_2, τ_1, τ_2, T_2 and T_3. Figure 22 illustrates these parameters and how different possible combinations of these three layers can be expected to contribute brightness temperature maxima to the frequency of occurrence histogram. Any combination of these emitting or absorbing layers used to generate a particlar histogram peak must also predict the proper limb-darkening associated with that particular brightness temperature.

Figure 22 - Conceptual Jovian three-layer cloud model. Illustrated are all the possible modes of thermal emission and the related cloud configurations. In a three-layer model some combination of these modes of emission are responsible for the observed tri-modal brightness temperature distribution. Also shown are the model parameters for each cloud layer. The constraints of $T_1 \approx 140°K$, $\tau_3 = \infty$ and $f_3 = 1$ are initially placed on the model. Reflected solar radiation is not shown but will significantly affect the model only where brightness temperatures are less than 209°K.

POSSIBLE CLOUD CONFIGURATIONS FOR A THREE-LAYER MODEL

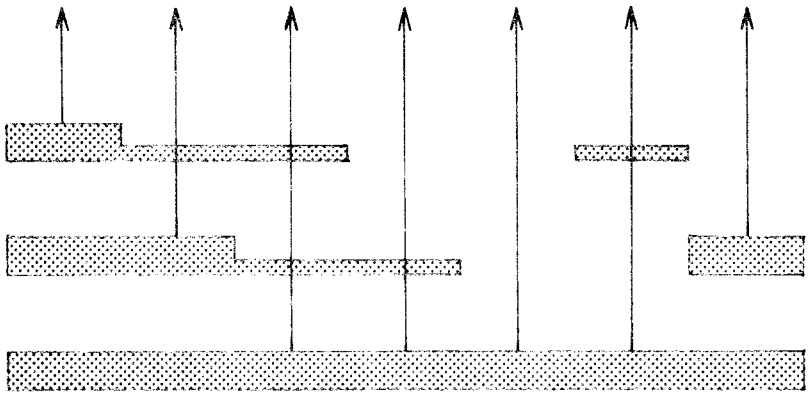

MODEL PARAMETERS

LAYER	TEMPERATURE	OPTICAL THICKNESS	FRACTIONAL COVER
1	$140^{o}K$	τ_1 or ∞	f_1
2	T_2	τ_2 or ∞	f_2
3	T_3	∞	1

THICK CLOUD (i.e. $\tau = \infty$)

THIN CLOUD (i.e. $\tau < \infty$)

Figure 22

It is perhaps easiest to begin with the limb-darkening associated with the highest brightness temperature peak in the histogram, and derive model cloud parameters for each layer. The limb-darkening curves for the hottest 5 μm regions display a very steep initial slope near the center of the disk with a gradual component of limb-brightening. Simple extinction of 5 μm radiation by a cold absorbing layer or limb-darkening derived from the isotropic scattering phase function for all values of particle albedo cannot alone account for the shape of the limb-darkening curve. This curve can, however, be produced by radiation, initially emitted by an optically thick lower cloud layer passing through an optically thin, warm, emitting layer. If the two lowest model cloud layers are responsible for the emission from the hottest belt regions then the limb-darkening can be written as:

$$F_H(\mu) = B(T_3)\, e^{-\tau_2/\mu} + B(T_2)\,(1 - e^{-\tau_2/\mu}) \qquad (3)$$

where $B(T_3)$ and $B(T_2)$ are the blackbody radiation emitted from the hot and warm cloud layers at temperatures T_3 and T_2 respectively, and τ_2 is the optical depth of the warm layer. The solution to this equation which best fits the observed brightness temperatures and limb-darkening gives $T_3 = 292 \pm 8\ ^{o}K$ $T_2 = 225 \pm 5\ ^{o}K$ and $\tau_2 = 2.0 \pm 0.4$. This has an implicit assumption that there is no substantial 5 μm opacity contribution from the uppermost cloud level. Figure 23 shows this model limb-darkening

FIGURE 23 - Limb-darkening model for 5 μm hot regions. The solid curve is the best fit limb-darkening model derived from Equation 3 and is plotted against the cosine of the emission angle (μ). The parameters used in this fit are $T_3 = 292^\circ K$, $T_2 = 225^\circ K$ and $\tau_2 = 2.0$. Also shown are the limb-darkening data from the hot brightness temperature regions in the North and South Equatorial Belts in 1973 and 1974. For comparison model fits with $T_3 = 305^\circ K$ (dashed), and $T_3 = 280^\circ K$ (dash-dot), are also shown using $T_2 = 225^\circ K$. These data and model fits are normalized on a relative flux scale to unity at $\mu = 0.9$.

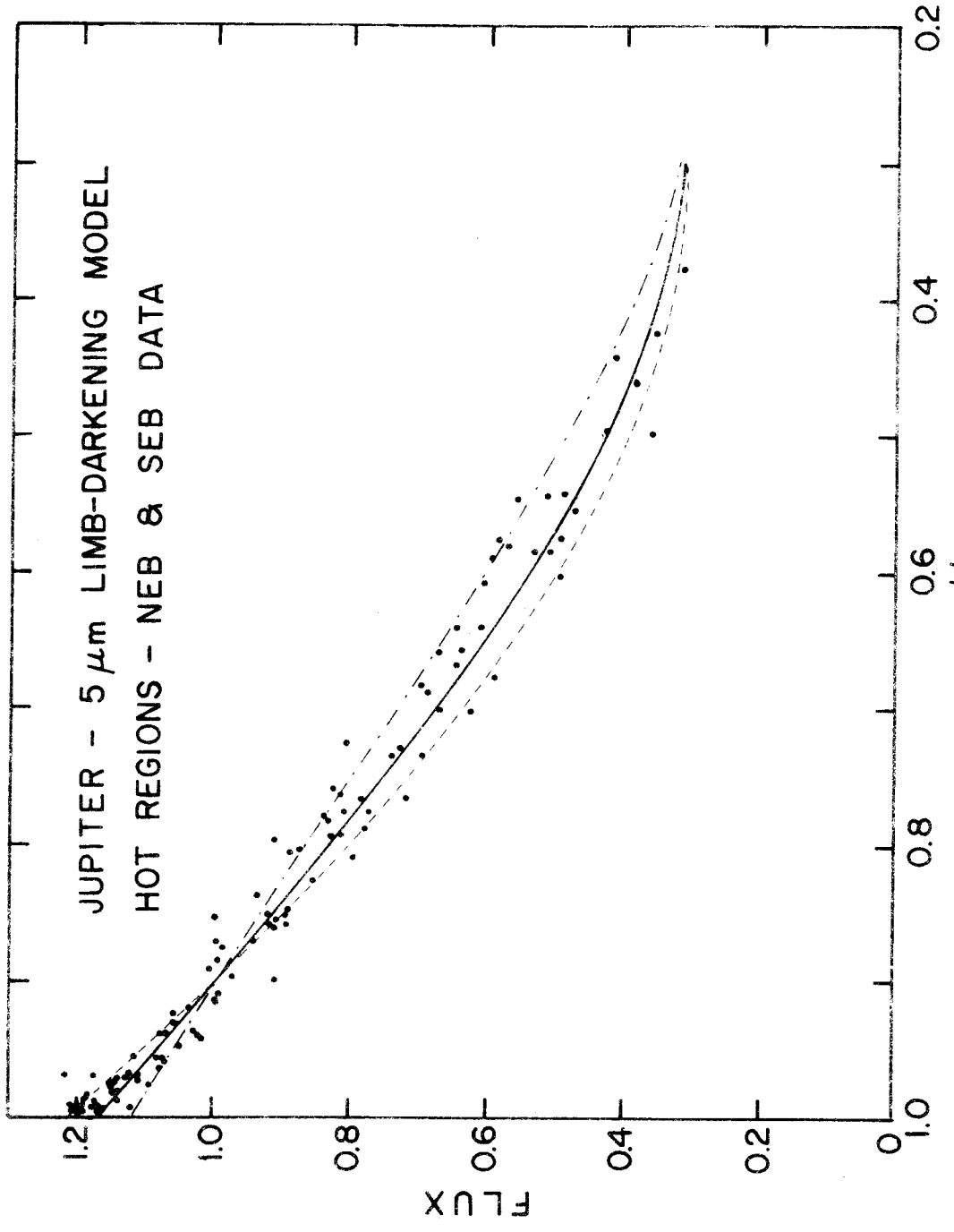
JUPITER - 5 μm LIMB-DARKENING MODEL
HOT REGIONS - NEB & SEB DATA
FLUX
μ
1.2
1.0
0.8
0.6
0.4
0.2
0
1.0
0.8
0.6
0.4
0.2

Figure 23

function plotted with data from 1973 and 1974 for the hot Equatorial Belt regions. These data and the model are normalized to unity at $\mu = 0.9$.

Emission at 5 μm from areas corresponding to the middle brightness temperature histogram peak, at about 225°K, have a characteristically flat limb-darkening curve compared to the hottest Jovian features. This curve can be simply approximated by an optically thick, isotropically radiating intermediate cloud layer superposed by a cold absorbing layer. This can be expressed as:

$$F_2(\mu) = B(T_2)\, e^{-\tau_1/\mu} \qquad (4)$$

where $B(T_2)$ is again the blackbody radiation emitted by the middle layer at temperature T_2, and τ_1 is the optical depth of the uppermost obscuring layer. The best fit to the observational data yields $\tau_1 = 0.3 \pm 0.1$ and $T_2 = 228 \pm 2$. This model is shown in Figure 24 along with data from 1973 normalized to unity, at $\mu = 0.9$. Alternatively, isotropic scattering by cloud particles in the middle layer could also produce the same shape for the limb-darkening curve if the single scattering albedo of the particles were 0.975. Any combination of scattering in the middle cloud and absorption in the upper layer yields an optical thickness for the upper layer (τ_1) less than 0.3 and a middle cloud temperature between 225 and 230°K. It is clear from this that the atmosphere above the brown belt, intermediate brightness temperature regions is relatively clear of high clouds, except for

FIGURE 24 - Limb-darkening model for 5 μm intermediate regions. The solid curve is the best fit limb-darkening model derived from Equation 4 and is plotted against the cosine of the emission angle (μ). The parameters used in this fit are $T_2 = 228^\circ K$ and $\tau_1 = 0.3$. Also shown are the limb-darkening data from the intermediate brightness temperature regions in the North Equatorial Belt in 1973. These data and the model fit are normalized on a relative flux scale to unity at $\mu = 0.9$. For comparison model fits for $T_2 = 230^\circ K$, $\tau_1 = 0.4$ (dashed curve) and $T_2 = 226^\circ K$, $\tau_1 = 0.2$ (dash-dot curve) are also shown.

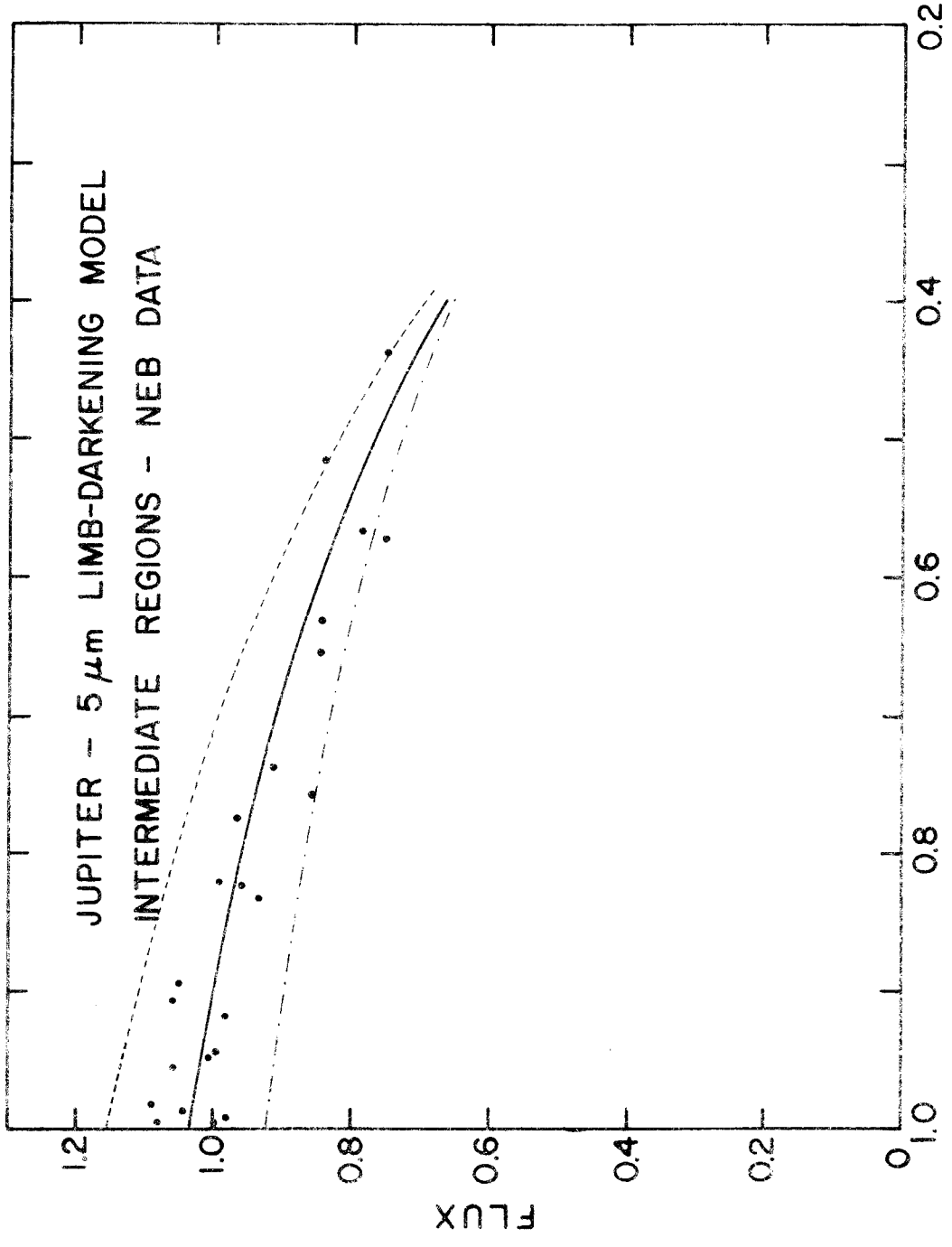
JUPITER - 5 μm LIMB-DARKENING MODEL
INTERMEDIATE REGIONS - NEB DATA
FLUX
μ
1.2
1.0
0.8
0.6
0.4
0.2
0
1.0
0.8
0.6
0.4
0.2

Figure 24

perhaps a very thin cold haze layer. Also, in the case of the hottest regions, the model cloud top temperature for the optically thick middle cloud is effectively the same as the temperature derived for the warm obscuring layer. This implies that the middle cloud occasionally thins to a τ_2 of about 2 to allow observation of the hot emission from the lowest cloud deck. This imposed thinning is in a statistical sense because it must be averaged over a region of about 9×10^6 square km (the resolution element of the 5 μm imaging system). Within this area, if the middle cloud has a patchy structure smaller than the resolution element, then an 86 ± 5% partial cloud cover of optically thick clouds would have the same observational effect as a uniform cloud of optical depth 2.0 ± 0.4, provided that there is no additional limb-darkening from geometrical effects (caused when the lateral structure in the clouds is of comparable size to the cloud thickness).

In order to solve for the model parameters of the uppermost cloud layer, corresponding to Jovian zones, spectroscopic observational data must be relied upon. Unlike the warmer belt regions where limb-darkening information was useful, the low 5 μm brightness temperatures of the zones create an ambiguity in which limb-darkening produced by either absorbed or scattered thermal radiation cannot be separated from that produced by scattered solar flux. However, from combined information on the degree of 5 μm spectral line desaturation allowable from observations and the knowledge of the simultaneous

flux distribution, a limit was placed on the amount of reflected solar flux contributing to the observed brightness temperature of 203°K during one particular observing run. This limit is that the mean reflectivity of the zone cloud cannot exceed 0.36. If thermal radiation from a thick middle cloud is being attenuated by the upper layer then this relationship can be expressed as:

$$F_1(\mu) = B(T_2)\, e^{-\tau_1/\mu} + B(209)\, R \qquad (5)$$

where $B(T_2)$ is the blackbody radiation emitted by the middle cloud at temperature T_2, τ_1 is the optical depth of the upper cloud, B(209) is the equivalent solar reflected radiation from a perfectly diffusing surface with an albedo of unity at the distance of Jupiter, and R is the mean reflectivity of the upper layer. For $T_2 = 225 \pm 5$°K τ_1 can range from 1.4 ± 0.3 to 2.2 ± 0.3, depending on what value of R is used (R between zero and 0.36). This range for the optical thickness of the upper cloud corresponds to one particular cloud configuration at the time the spectroscopic observations were made and does not represent a parameter which has been checked for temporal consistency. However, temporal variations measured in the spectra and in the 5 μm areal flux distributions are, in general, small and do not significantly change the overall characteristics of this model cloud layer. These model parameters indicate the upper zone cloud layer is relatively thin and allows radiation from lower, warmer cloud levels to be observed.

Fractional cloud covers for the upper and middle cloud layers can be derived from the area under each histogram peak. If these areas are A_{205}, A_{225} and A_{250}, corresponding to peaks with mean brightness temperatures 205, 225 and 250°K respectively, then the fractional cloud covers can be expressed as:

$$f_1 = \frac{A_{205}}{A_{205} + A_{225} + A_{250}} \tag{6}$$

$$f_2 = \frac{A_{205} + A_{225}}{A_{205} + A_{225} + A_{250}} \tag{7}$$

for which the solutions, corresponding to the data in Figure 19 are $f_1 = 0.15 \pm 0.01$ and $f_2 = 0.64 \pm 0.08$. The errors expressed here are due to the uncertainty in measuring the area in the histograms and do not represent the variability of the cloud covers.

The final version of the three layer cloud model is summarized in Figure 25. Radiation arising from an optically thick cloud deck at a temperature of about 292°K and attenuated by a warm cloud layer of approximate optical depth 2 and temperature about 225°K is responsible for the highest temperature peak in the Jovian brightness temperature histogram. These clearest regions correspond to the blue-gray areas in the Jovian belts. The middle histogram peak, corresponding to brown belt areas, arises from portions of the middle cloud layer where it is optically thick and relatively unobscured by higher clouds. Radiation from the white zones, responsible for the lowest temperature histogram peak, also comes from the thick middle cloud; but it is attenuated by a high cold

Figure 25 - Complete representation of the three-layer cloud model. This version of the Jovian cloud system is the simplest model which can be derived from three layers while still agreeing with all the 5 μm observations. A cross-section through a belt and a zone is shown with the thickness of each layer representing its relative optical depth. The model cloud top temperatures are shown for each layer along with the mode of thermal emission for each of the three brightness temperature histogram peaks. The observed brightness temperatures and visible color correlations for these modes are indicated at the top. Also shown is a probable dynamical state which could sustain this cloud configuration. Arrows at the bottom indicate regions of rising and sinking gases.

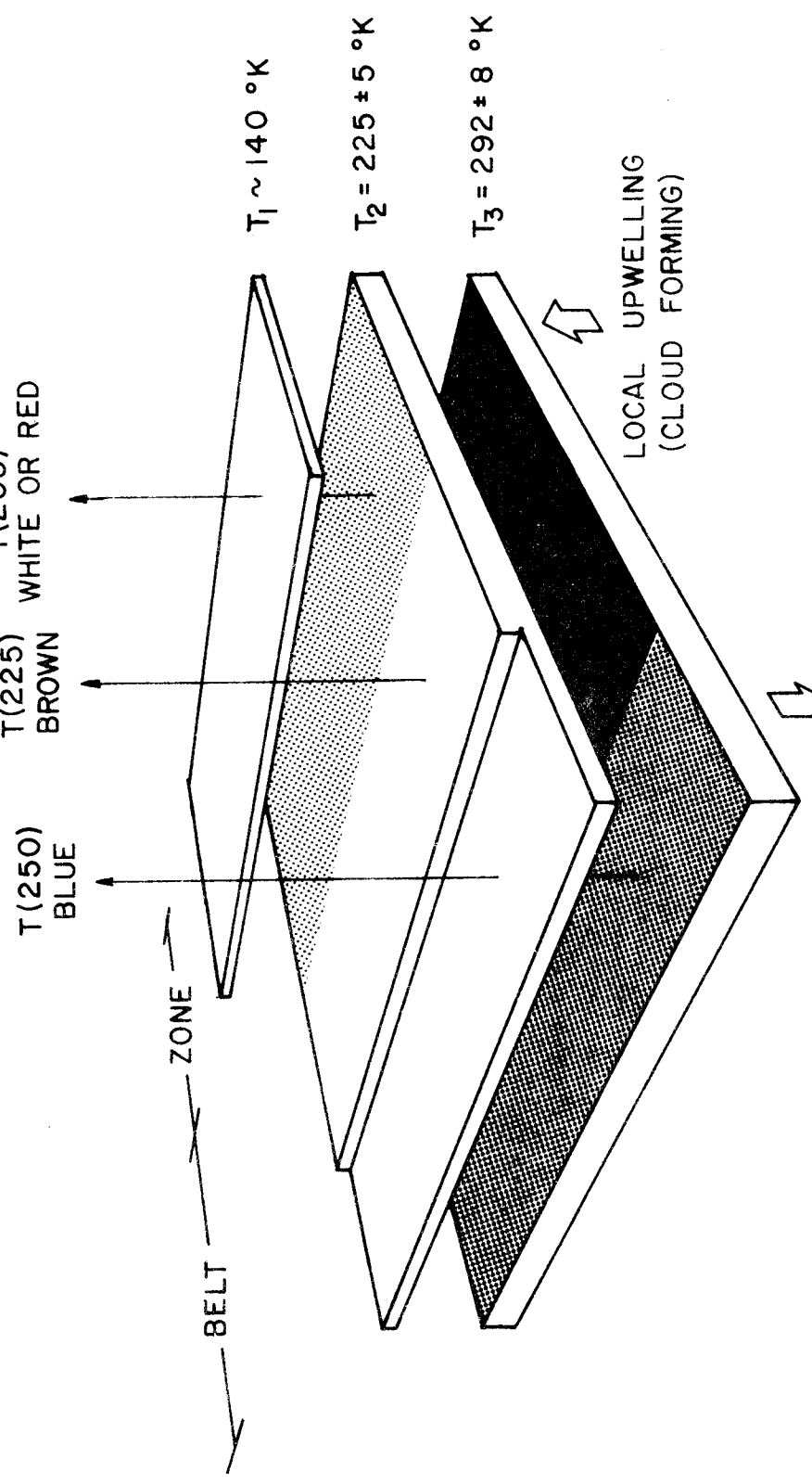
T(205)
WHITE OR RED
T(225)
BROWN
T(250)
BLUE
ZONE
BELT
$T_1 \sim 140$ °K
$T_2 = 225 \pm 5$ °K
$T_3 = 292 \pm 8$ °K
LOCAL UPWELLING
(CLOUD FORMING)
LOCAL DOWNWELLING
(DRYING)

Figure 25

cloud (presumably ammonia at 140°K). This cloud has a maximum 5 μm reflectivity of 0.36 corresponding to a maximum optical depth of about 2.2.

The middle model cloud layer is presumed to be optically thick everywhere under the upper layer. If this were not true then radiation from the lower cloud would be observed through breaks in the middle cloud and through the thin upper cloud. This would result in a white zone area exhibiting local regions with brightness temperatures of about 232°K. Since this result has never been observed in any of the 5 μm data, then it is reasonable to assume that the middle cloud is optically thick under the zones.

This cloud model not only gives the best agreement with the observed limb-darkening data, but also agrees with the observation that regions exhibiting different brightness temperatures correlate with different colored areas on the disk. These color differences can be interpreted as arising from differences in the composition or scattering properties of the uppermost cloud. In this model the uppermost cloud, for each of the three temperature regimes, is either a different layer or has different transmission properties. Other combinations of opacities and cloud temperatures are, of course, possible with a three-layer model, but in general these are unsatisfactory because they fail to predict the observed 5 μm limb-darkening and cloud color correlations.

The constraints on the vertical cloud structure implied by the 5 μm observations of Jupiter have been summarized in this model. More complex structures than those in the model cannot be excluded, but simpler models all have difficulty with some aspect of the observational data. At wavelengths other than 5 μm, the optical parameters will differ. In particular, the "clear" regions in the model probably contain thin haze, which might be nearly opaque in the visible and near infrared. Such refinements might be required to explain the belt to zone variations of near infrared spectral features of CH_4 and NH_3 (Owen, 1969).

C. Speculations

In this section speculations are made concerning the types of dynamics that could be present in the Jovian cloud system, assuming that it has a form similar to the model formulated in the last section. This model is also compared to theoretical predictions for the cloud compositions. Also discussed is a possible explanation of the correlation between the hottest 5 μm features and the blue-gray colored areas in Jovian belts.

(i) Possible Jovian Cloud Dynamics

The presumed vertical motions of gases in the multiple layer cloud model are illustrated in Figure 25 based on the dynamical description of Ingersoll and Cuzzi (1969). The upwelling of warm saturated gases in the zones produces a cloudy region with a high layer of ammonia clouds. Similarly, regions of local downwelling

in the blue-gray colored belts are relatively cloud-free areas of clear, dry atmosphere allowing observations of high brightness temperatures in the deep atmosphere. Various degrees of up and downwelling are probably present in the intermediate brightness temperature areas to produce a thick layer of middle clouds, with a relatively clear upper atmosphere. Assuming that this vertical cloud structure is representative of Jupiter, then some speculations about the global cloud dynamics can be made by considering the horizontal flux distribution over the disk. Figure 13d (Chapter IV) shows the spatial distribution of areas with brightness temperatures in each of the three peaks in the flux-frequency histogram. The contoured areas in this figure also correspond to the proposed dynamical regions of local up and downwelling. In the latitude region between $+45^{o}$ to -45^{o} these regions appear as latitudinal bands of rising and sinking gas. Presently there is little theoretical evidence to account for east-west convective rolls with horizontal scales many times larger than the atmospheric scale height. However, these surface manifestations may be the result of convection from deep in the body of the planet.

On a smaller scale, the doughnut-like 5 μm features seen at high latitudes may be analogous to terrestrial storm systems. These 5 μm features are warm regions about 8000 km in diameter with cold cloudy cores about 3000 km in diameter. Terrestrial hurricanes characteristically have a broad cloudy central region of upwelling surrounded

by a ring of relatively clear downwelling atmosphere (Palmén and Newton, 1969). The 5 μm signature of such a storm system would appear similar to the doughnut-like Jovian features. If these Jovian features are indeed analogous to terrestrial storm systems then future observations from earth orbit or from spacecraft flybys should resolve clear areas at the storm centers (terrestrial hurricanes usually have a small central eye clear of clouds) and possibly detect vorticity in the clouds.

(ii) Composition of Clouds

By using the derived model cloud top temperatures and comparing these to theoretical predictions for Jovian cloud condensation temperatures (Lewis, 1969; Weidenschilling and Lewis, 1973) it is possible to make some speculations on the composition of the three model cloud layers. Due to the steepness of the Planck function at 5 μm for temperatures below about 190°K and the possible contamination from reflected solar flux, only an upper limit of 190°K can be obtained for the uppermost cloud from 5 μm data. This limit is consistent with a cloud layer of condensed NH_3 with an effective temperature of 140°K. This is supported by the observed correlation between 5 μm images and 45 μm Pioneer 10 images which have a measured temperature of 140°K. Model temperatures for the intermediate layer of about 225°K are agreeably close to the temperature predicted for a layer of ammonium hydrosulfide, NH_4SH (Lewis, 1969). The same predictions, however, place a theoretical water

cloud at about 270°K. Such a layer has not been observed, rather it is found that a temperature of about 290°K is required for the lowest cloud layer. Perhaps the aqueous cloud is depressed because it is observed only in regions of local downwelling, where the gas has low relative humidity by virtue of its recent excursion into the cold upper atmosphere. This picture is consistent with the H_2O detection at 5 μm by Larson et al. (1975) in which they find water depleted by a factor of 10^3 relative to solar composition. This apparent depletion could be due to dynamics of cloud condensation and evaporation (i.e., in regions of high H_2O content, high clouds observe observations). Alternatively, the particles in the lowest cloud may be very impure water or some other chemical altogether.

(iii) Rayleigh Scattering as an Explaination for the Blue-Gray Color of Jovian Hot Spots

The close association of the visible blue-gray Jovian features with the hottest 5 μm regions is difficult to explain on the basis of reflection off of "blue" clouds, since few naturally occurring materials possess such a color. However, this phenomenon can be understood through a Rayleigh scattering model. Consider a semi-infinite atmosphere of molecular hydrogen gas. Using the Lorentz-Lorenz relationship and equation 205 from Chandrasekhar (1960), it can be shown that the mass scattering coefficient for molecular scattering is given by:

$$K_\lambda = \frac{32\pi^3 m N_o}{3\rho_o} \frac{1}{\lambda^4} = K_o \frac{1}{\lambda^4} \qquad (8)$$

where m is the mass per molecule, N_o and ρ_o are the refractivity and density of H_2 at STP, and λ is the wavelength. In hydrostatic equilibrium, the optical depth τ_λ of this atmosphere at altitude z is given by:

$$\tau_\lambda = \frac{K_o}{g} \frac{1}{\lambda^4} P(z) \tag{9}$$

where g is the gravitational acceleration and P(z) is the pressure. Optical depth unity will occur at different pressure levels for different wavelengths. This relationship is shown in Table 5.

If there are clear areas in Jupiter's clouds where photons could penetrate to a level of several bars, one finds that short wavelength light would never reach this level, but would be conservatively scattered due to molecular scattering by hydrogen gas. On the other hand, longer wavelength photons would penetrate to this level and if they are non-conservatively scattered by absorbing particles (i.e., a gaseous absorber or a cloud with an albedo less than unity), then the region would appear blue from above the atmosphere. Methane gas in the deep atmosphere provides this absorption for much of the radiation longward of 6200 $\mathring{A}$.

Five-micrometer brightness temperatures of about 260°K, measured in this study for the hottest blue spots, corresponds to a pressure level of about 5.0 bars (Ingersoll, 1976; extrapolated from Orton 1975a,b). It is not unreasonable, therefore, that the

TABLE 5

RAYLEIGH SCATTERING PRESSURE AND OPTICAL DEPTH FOR PHOTONS OF VARIOUS WAVELENGTHS

λ (Å)	Pressure at $\tau = 1$ (Bars)	Pressure at $\tau = 3$ (Bars)
3500	1.3	3.9
4000	2.1	6.3
5000	5.3	15.9
6000	10.1	30.3
7000	20.2	60.6

blue color of these hot 5 μm regions comes from a combination of Rayleigh scattering and absorption in the red, if visible light penetrates to these levels.

CHAPTER VI

CONCLUSIONS

Over the past four years an observational program was undertaken of high spatial resolution imaging of Jupiter at 5 μm. This spectral window into the deep atmosphere has provided direct observational evidence of the existence of multiple layers of clouds in the Jovian atmosphere. First, the 5 μm flux-frequency distribution of equal areas on the Jovian disk is a trimodal function. This indicates that three distinct brightness temperatures have a higher probability of being observed than a continuum of temperatures. The persistence of this trimodal distribution despite significant variations in the lateral 5 μm cloud distribution indicates that this phenomenon is a long term stable vertical cloud feature. Second, the visible color differences correlate with areas of different 5 μm intensity. This implies that the colors are due to reflection from areas of different chemistry or state at different levels in the atmosphere. Third, the short time scales associated with large 5 μm flux variation over extensive areas of the Jovian disk indicate condensation and evaporation of obscuring cloud layers. And finally, 5 μm limb-darkening and opacity models derived from imaging and spectroscopic data are consistent with multiple cloud layering in the Jovian atmosphere.

Further information about the Jovian clouds results from the combination of 5 μm spectroscopic and imaging data sets. First, from the shape of the spectrum in the 5 μm region true maximum brightness

temperatures are derived, corrected for the clearest regions in the Jovian atmosphere. Secondly, from data on spectral line saturation, limits are placed on the 5 μm cloud reflectivity over the field of view of the spectrometer. By combining this information with the knowledge of the spatial distribution of flux, constraints are derived for the optical properties of the upper Jovian clouds.

These results are incorporated in a three layer cloud model which is consistent with all the observational data at 5 μm. The three model cloud layers have cloud top temperatures of $T_1 \leq 190°K$ (presumably $T_1 \simeq 140°K$), $T_2 = 228 \pm 2°K$ and $T_3 = 292 \pm 8°K$. The highest layer, found only over the white zones and red spots, has optical depth near unity and transmits radiation from deeper levels. This upper level has a mean 5 μm cloud reflectivity less than 0.4, while the whole central 25% of the disk must have a mean reflectivity less than 0.1. The middle cloud deck is present under the upper level clouds and over the brown colored Jovian belts. This level is optically thick everywhere except in regions where blue-gray areas are visible. Here the middle level thins to a mean optical depth of about 2 and allows radiation from the deepest and hottest level to be detected.

This cloud model provides a physically reasonable and self-consistent picture for the nature and properties of the Jovian 5 μm features. It further provides a preliminary basis for the interpretation of other observational data acquired in this spectral

region. Further refinement of this model for the deep atmospheric cloud structure of Jupiter must await higher spatial and spectral resolution data from either Earth or Jupiter orbit.

APPENDIX

This supplementary section illustrates the versatility of the equipment and observational techniques developed for this thesis. An imaging system similar to the one used to produce high spatial resolution images of Jupiter at 5 μm was used to observe Jupiter at 8-14 and 20 μm (Terrile and Westphal 1977b). The results of these observations are presented in this appendix.

A. Introduction

The 8-14 μm spectral region has provided a window through which many interesting observations of Jupiter have been made. Gillett et al. (1969) observed the full disk spectrum in this region and found a complex brightness temperature structure indicative of a temperature inversion. Westphal (1971) observed large contrast structure in north-south scans at 8.5 μm which correlated with albedo markings. The thermal inversion was confirmed by Gillett and Westphal (1973) by demonstrating limb-brightening at 7.9 μm. As a result of these observations, Orton (1975b) has constructed thermal models for the upper atmosphere. Figure A.1 shows the spectrum of Jupiter from 5 to 25 μm using the data of Gillett et al. (1969), Aitken and Jones (1972), Gillett (1973), Aumann and Orton (1976) and Russell and Soifer (1977). Also shown on the figure are the dominant sources of opacity at various spectral regions (Orton, 1975b). In order fully to understand the relationships of opacity sources and belt-zone thermal structure differences a knowledge of the two-dimensional distribution of radiation

FIGURE A.1 - Infrared spectrum of Jupiter. This spectrum is composed of observations from Gillett et al. (1969), Aitken and Jones (1972), Gillett (1973), Aumann and Orton (1976) and Russell and Soifer (1977), and is shown in terms of calibrated brightness temperature. Also shown are the major sources of opacity in the Jovian atmosphere and the spectral regions where they dominate (Orton, 1975b). The approximate half-power spectral bandpasses of the infrared imaging filters are also indicated.

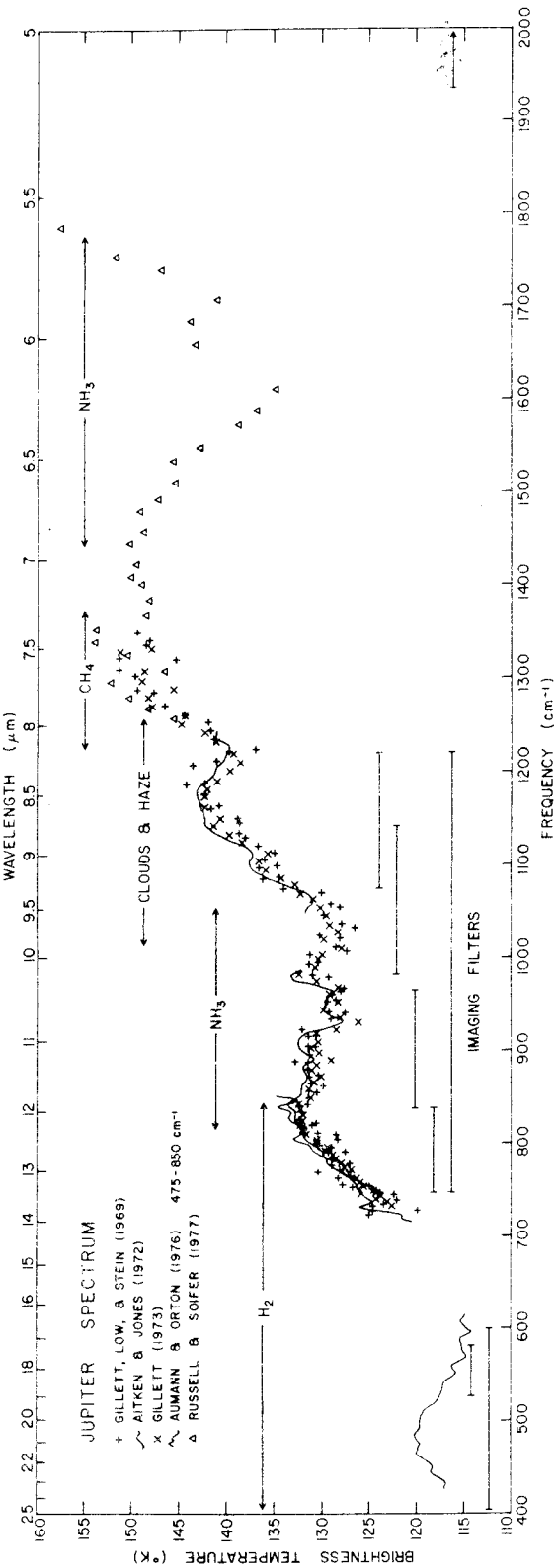
JUPITER SPECTRUM
+ GILLETT, LOW, & STEIN (1969)
~ AITKEN & JONES (1972)
× GILLETT (1973)
~ AUMANN & ORTON (1976) 475-850 cm⁻¹
△ RUSSELL & SOIFER (1977)
CH4
NH3
CLOUDS & HAZE
NH3
H2
IMAGING FILTERS
WAVELENGTH (μm)
FREQUENCY (cm⁻¹)
BRIGHTNESS TEMPERATURE (°K)

Figure A.1

is needed. This information is provided by imaging Jupiter with high spatial resolution in the 8-14 and 20 μm spectral regions.

B. Observations

On UT 31 August 1974, UT 25 October 1975 and UT 6 October 1976 Jupiter was observed at the east arm Cassegrain focus of the Hale 5-meter (200-inch) telescope using an optical arrangement similar to the one previously described in Chapter II. However, the 5 μm dewar was replaced with a Low dewar containing a gallium doped germanium bolometer cooled to 2^{o}K with pumped liquid helium. Radiation was focused onto this detector through a cold 2-mm round aperture corresponding to a projected sky resolution element of 1 arcsec. Jupiter had an equatorial diameter of 49.5 arcsec in 1974 and 1975 and 46.0 arcsec in 1976. The Gregorian wobbling secondary was driven with a programed signal such that the image of Jupiter moved across the aperture in sixty-four 40 msec steps. After each 40 msec integration, the planet's image was moved out of the field of view allowing a 40 msec integration of the background sky. The net signal, synchronously detected with a phase lock amplifier, was digitized to 8 bits (256 gray levels) and stored on magnetic tape using the data system described in Chapter II. At the end of each scan the secondary mirror was returned to its starting position in 640 msec. As the secondary scanned in declination, the telescope's right ascension tracking rate was adjusted to move the image in the focal plane such that a raster of 64 x 64 pixels with 0.75 arcsec pixel spacing was achieved. In this way complete images

were recorded every 6.14 minutes. The real-time TV display from the data system was used to determine data quality and filter sequencing. The data were reformated in a computer to 256 x 256 pixels to produce an output magnetic tape compatible with the playback system described by Westphal (1973). During all three apparitions of Jupiter, a broad-band 8-14 μm filter was used, but in 1975 and 1976 1 and 2 μm wide filters at 8.7, 9.5, 11.2 and 12.5 μm were included. Additionally, in 1976 imaging was performed through a broad-band 17-25 μm filter and a narrow-band 18 μm filter. The approximate half-power spectral bandpasses of these filters are illustrated in Figure A.1. In order to increase the signal-to-noise ratio, adjacent images taken with the same filter were registered and added together pixel by pixel.

C. Results

The results of the broad-band 8-14 μm imaging are shown in Figure A.2b, c, and e, taken near 04:35 UT 31 August 1974, 08:15 UT 25 October 1975 and 07:07 UT 6 October 1976, respectively. Figures A.2b and c were constructed from four raw data frames taken sequentially while Figure A.2c was constructed from five. This averaging causes a longitudinal smearing of about 15^{o} in the first two images and 14^{o} in the last, but this smearing does not affect the axi-symmetric banded structure visible in the images.

Broad-band 8-14 μm Jupiter images reveal a banded structure similar to the belt-zone features on visible photographs. Figure A.2a is a copy of a Kodachrome slide taken at UT 07:43 28 September 1974

FIGURE A.2 - Comparison of visible photographs with 8-14 μm images of Jupiter over a three year period. Figure A.2a is a copy of a Kodachrome slide taken at 07:43 UT 28 September 1974 with a System II central meridian longitude of 36°. Figures A.2b and c are 8-14 μm images made from four raw data frames each. They were recorded around 04:35 UT 31 August 1974 and 08:15 UT 25 October 1975 with mean System II central meridian of 31° and 243°, respectively. Figure A.2d is a copy of an Ektachrome slide taken at 07:07 UT 6 October 1976 with a System II central meridian of 101°. Figure A.2f is an 8-14 μm image constructed from four raw data frames recorded 21 minutes before and 11 minutes after the visible photograph in Figure A.2d. Figures A.2b, c and f illustrate the yearly global variations in the 8-14 μm appearance of Jupiter. In all the images north is at the top and east at the right.

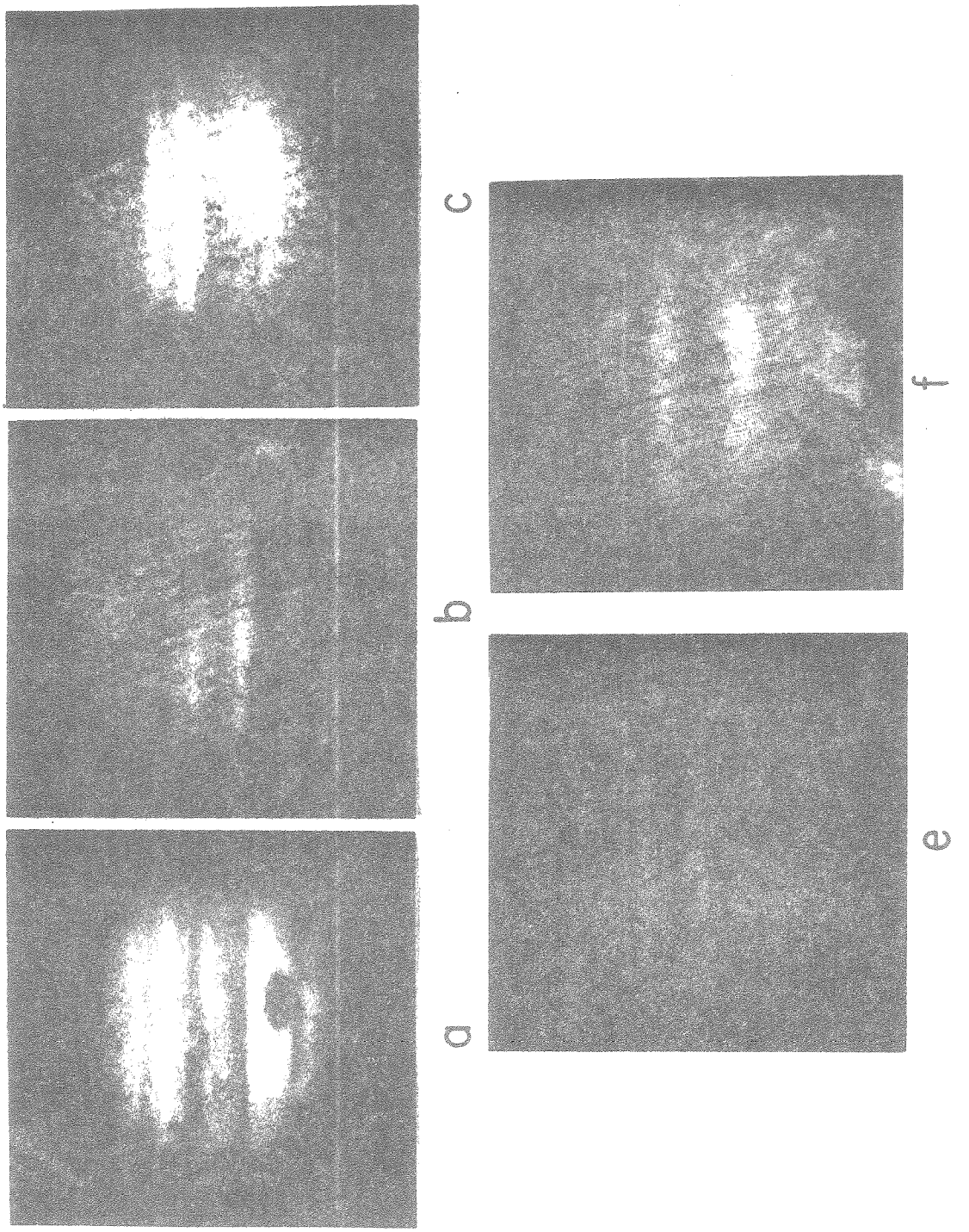

Figure A.2

which has a system II central meridian within 5° of Figure A.2b. Similarly, Figure A.2d is a copy of an Ektachrome slide taken at UT 07:07 6 October 1976, and has the same central meridian longitude as Figure A.2e. A direct comparison can be made between the visible photographs and their infrared counterparts. The dark belts in the visible correspond very closely to the warm (high flux) areas in the 8-14 μm images while the zones correlate with the cool (low flux) regions. The Great Red Spot appears smeared out in the composite image in Figure A.2b, but examination of individual frames confirms the observations of Wildey et al. (1965) that the Great Red Spot is colder than its surrounding area. A comparison of Figures A.2b, c, and e illustrate that over the course of one year large changes in the flux distribution in the 8-14 μm region are possible. It should also be noted that similar large changes were observed in the positions of the belts and zones in the visible images from these aparitions (see Chapter IV section B). Figure A.3 is a north-south scan taken from the image in Figure A.2c. Indicated on the scan are the positions of some of the more prominent belts and zones which appeared in photographs taken at the same time. A strong correlation is observed between belts and zones and high flux and low flux infrared areas. The flux contrast in this scan is about 20%.

Using the flux calibration of Gillett et al. (1969) over the broad-band region it is possible to derive brightness temperature contrasts in the images. In all three apparitions, belts appear to

FIGURE A.3 - North-south scan of the central meridian of Jupiter at 8-14 μm. This scan is part of an image recorded at 08:15 UT 25 October 1975. Shown on the scan are the positions of some of the more prominent belts and zones.

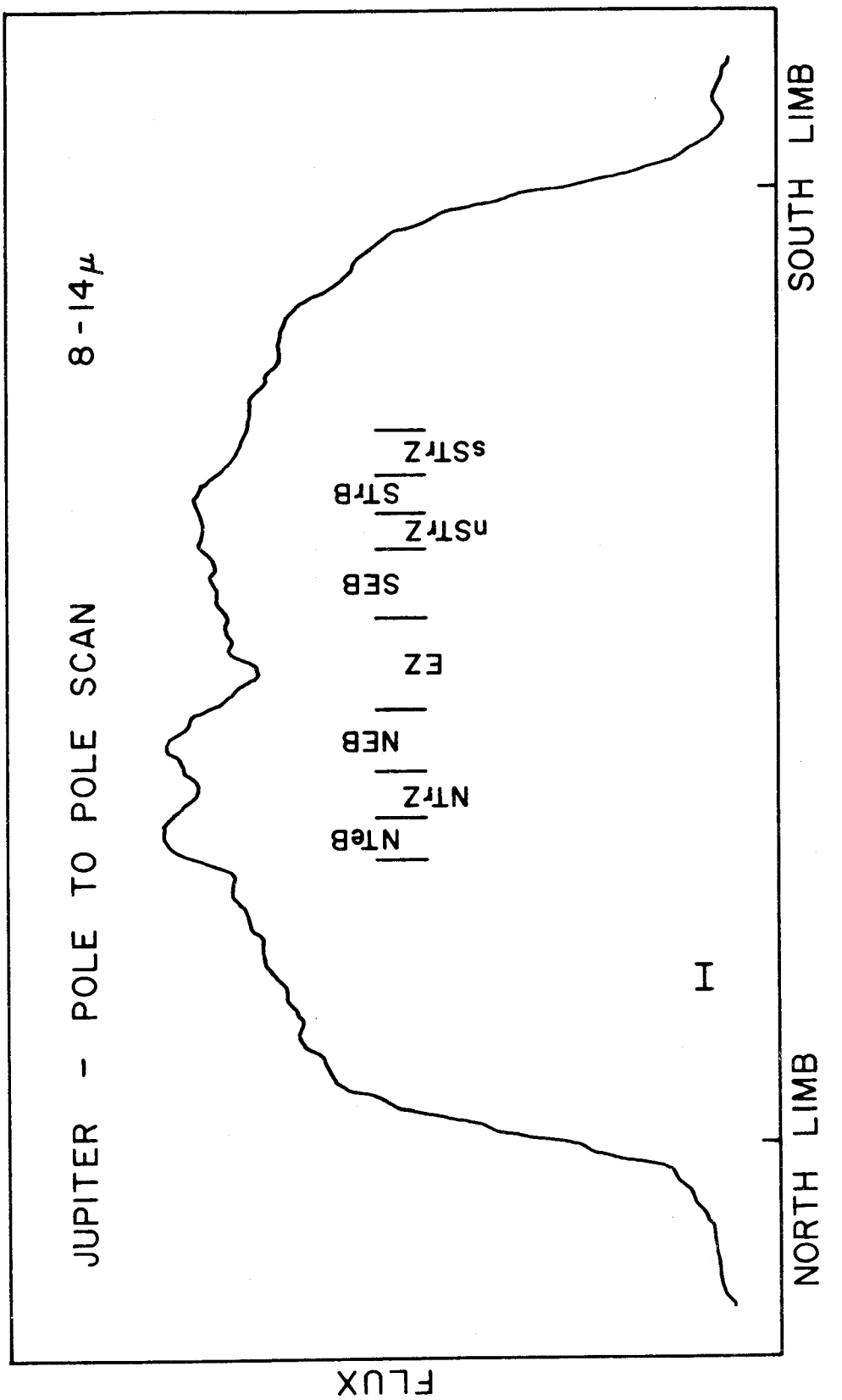
JUPITER - POLE TO POLE SCAN
8-14μ
FLUX
NORTH LIMB
SOUTH LIMB
H
NTeB
NTrZ
NEB
EZ
SEB
nSTrZ
STrB
sSTrZ

Figure A.3

be about 2.2°K hotter than the zones when an average disk brightness temperature of 130°K is used. Numerous opacity sources are present in the Jovian atmosphere in the 8-14 μm region (Gillett et al., 1969; Orton, 1975b) so the cause of the belt-zone contrast cannot be approached from the broad-band studies. However, narrow-band data can help to resolve this question.

Images produced in 1975 and 1976 through 1 and 2 μm wide filters reveal a large variation in belt-zone contrast across the 8-14 μm spectral region. The least contrast was observed in the hydrogen opacity dominated region near 12.5 μm. Here belt-zone flux contrasts of 12% were seen corresponding to a temperature difference of 1.7°K when using an average disk brightness temperature of 130°K. The largest belt-zone contrast was recorded in the 9.5 μm filter bandpass. Figure A.4 is a comparison plot of north-south scans made in the 9.5 and 12.5 μm filters. Both scans are normalized to the center three arcsec of the disk. The contrast in the 9.5 μm band is 32% in flux and again using 130°K for the disk brightness at 9.5 μm, a belt-zone temperature difference of 3.5°K is derived. There is also considerably greater limb-darkening in the 9.5 μm band than at 12.5 μm.

Figure A.5 is a composite image made from two raw data frames in the region of 9.5 μm. This image was recorded near 11:00 UT 25 October 1975 with a longitudinal smearing of 6°. The most prominent feature in the 9.5 μm image is an isolated bright region in the southern component of the South Equatorial Belt. The

FIGURE A.4 - Comparison of north-south scans at 9.5 and 12.5 μm. Both scans are part of images recorded on UT 25 October 1975 and are normalized to the center 3 arcsec of the disk.

FIGURE A.5 - Narrow-band 9.5 μm image of Jupiter. This image was made from two raw data frames recorded near 01:00 UT 25 October 1975. A one-dimensional Gaussian filter with a half-width of 1 pixel was applied perpendicular to the scan direction in order to smooth some of the high-frequency noise across adjacent scans caused by low-frequency detector drifts. North is at the top and east is at the right.

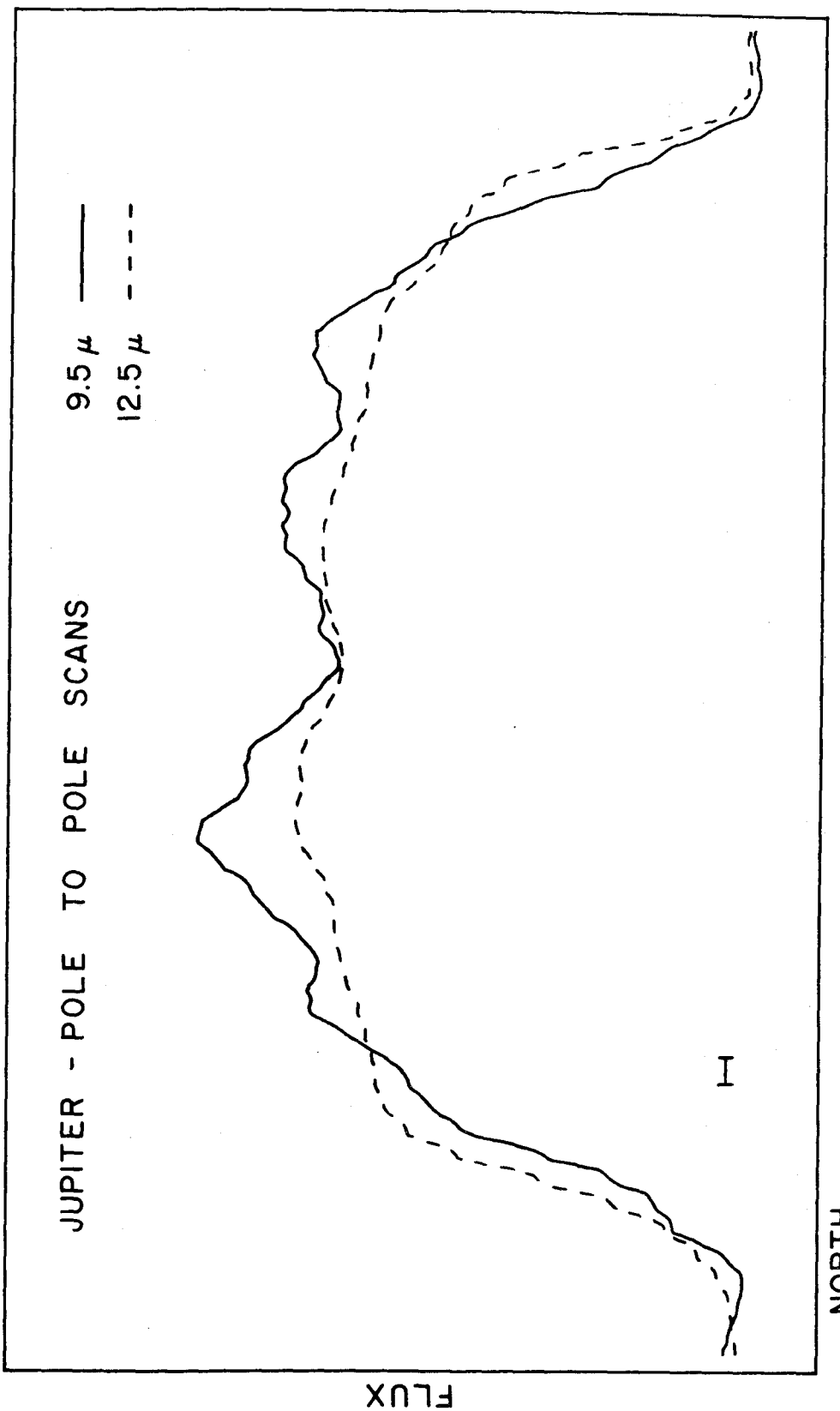

Figure A.4

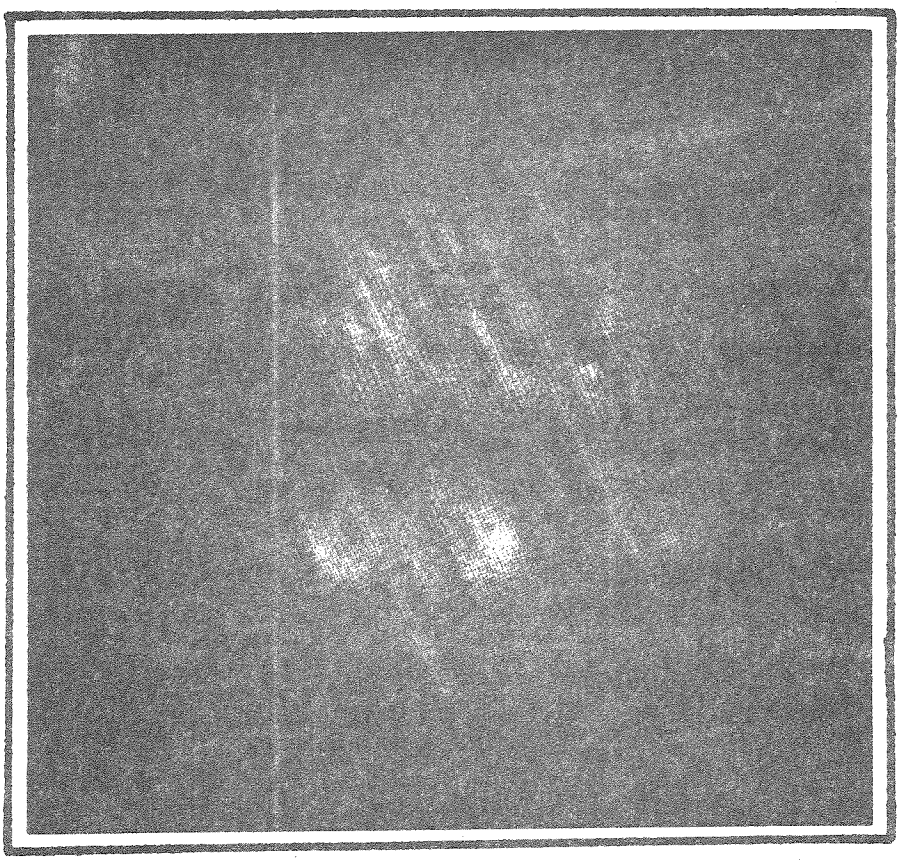

Figure A.5

measurements indicate that this feature is about 4°K hotter then the surrounding area and does not correlate with any visible marking. Specifically, it is not related to the Great Red Spot, which is 35° to the west of the 9.5 μm hot spot.

Figure A.6 is a comparison of a copy of an Ektachrome slide (Figure A.6a) taken at 09:18 UT 6 October 1976 and 20 μm broad-band image (Figure A.6b) made from four raw data frames recorded 11 minutes before and 15 minutes after the visible photograph was taken. The overall flux distribution of the 20 μm image is similar to the 1976 image at 8-14 μm with the equatorial belts displaying the brightest flux and the zones displaying the lowest. Figure A.6b can also be compared with Figure 18b which is the 20 μm image acquired by Pioneer 10 in 1973. Ground-based 20 μm broad-band images have belt-zone contrasts of about 26%. Using an average disk brightness temperature of 120°K (Aumann and Orton, 1976) over the 20 μm filter, temperature contrasts of about 5°K are measured between belts and zones. These temperature differences are consistent with those measured by Pioneer 10 and 11 (Ingersoll et al., 1976). The ground-based 20 μm images, like the Pioneer images, are relatively flat and display little limb-darkening.

D. Conclusions

This study has produced the first high spatial resolution 8-14 μm images of Jupiter. Broad-band images correlate well with visible images with belts appearing 2.2°K hotter than zones. Correlations

FIGURE A.6 - Figure A.6b is a copy of an Ektachrome slide taken at 09:18 UT 6 October 1976, with a System II central meridian longitude of 304^{o}. Figure A.6b is a 20 μm broad-band image made from four raw data frames recorded 11 minutes before and 15 minutes after the visible photograph was taken. North is at the top, east at the right.

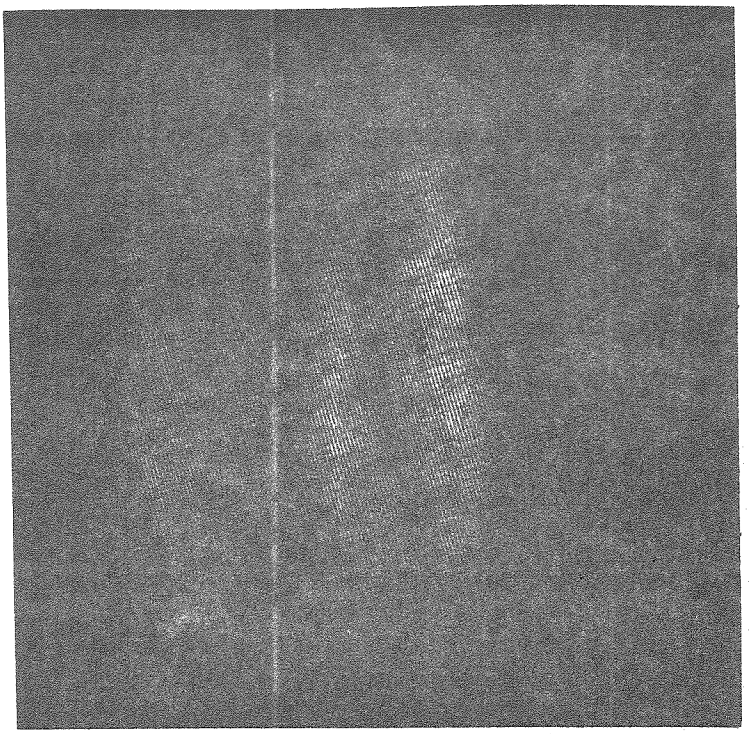

b

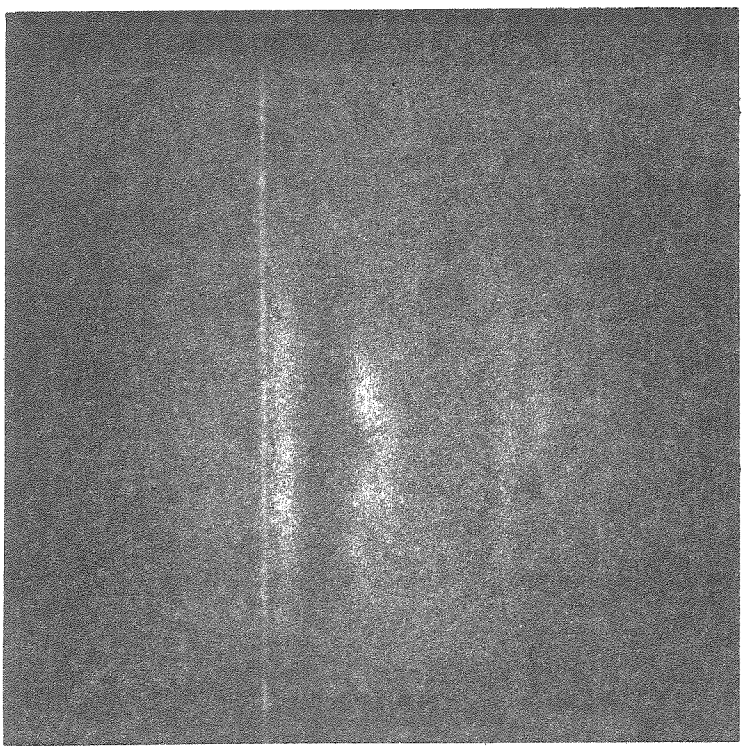

a

Figure A.6

with 5 μm images recorded two days earlier (Terrile and Westphal, 1976a) also show that hot 5 μm areas are, in general, hot 8-14 μm regions. However, the warm 8-14 μm areas seem to correlate with both blue and brown belt regions while the hottest 5 μm regions correspond only to blue belt areas. At 20 and 45 μm, the Pioneer 10 and 11 infrared radiometer results (Ingersoll et al., 1976) indicate a similar belt zone contrast with the effective temperature of belts greater than zones by as much as 3.5°K. Ground-based 20 μm broad-band imaging shows similar flux distributions with maximum belt-zone brightness temperature contrasts of about 5°K. Contrast across the 8-14 μm window varies between regions dominated by different opacity sources with the largest contrast near 915 μm. Narrow band images at 9.5 μm display an isolated feature 4°K hotter than the surrounding area. Orton (1975b) finds that contrast in this region is a result of inhomogeneities in the distribution of the solid particles in ammonia clouds and gaasous absorption by ammonia gas.

The contrast observed in the 8-14 μm region is larger than that predicted by the spatially differentiated models of Orton (1975b). This narrow-band limb-darkening and belt zone contrast data should enable a refinement of present atmospheric models and lead to a better understanding of the observed lateral variations.

REFERENCES

Aitken, D.K. and Jones, B. (1972). The 8 to 13 μm spectrum of Jupiter. Nature 240, 230-232.

Anderson, R.C. and Pipes, J.G. (1971). Jovian ultraviolet reflectivity compared to absorption by solid ammonia. J. Atmos. Sci. 28, 1096-1087.

Aumann, H.H. and Orton, G.S. (1976). Jupiter's 12-24 micron spectrum. Science 194, 107-109.

Baker, A.L., Baker, L.R., Beshore, E., Blenman, C., Castillo, N.D., Chen, Y.-P., Doose , L.R., Elston, J.P., Fountain, J.W., Gehrels, T., Kendall, J.H., KenKnight, C.E., Norden, R.A., Swindell, W., Tomasko, M.G., and Coffeen, D . (1975). The imaging photopolarimeter experiment on Pioneer 11. Science 188, 468-472.

Becklin, E.E. (1974). Private communication.

Beckwith, S., Evans II, N.J., Becklin, E.E., and Neugebauer, G. (1976). Infrared observations of Monoceros R2. Astrophys. J. 208, 390-395.

Beer, R. (1975). Detection of carbon monoxide in Jupiter. Astrophys. J. 200, L167-L169.

Beer, R. (1976). Private communication.

Beer, R., Farmer, C.B., Norton, R.H., Martonchik, J.V., and Barnes, T.G. (1972). Jupiter: Observations of deuterated methane in the atmosphere. Science 175, 1360-1361.

Beer, R., Norton, R.H. and Seaman, C.H. (1971). Astronomical infrared spectroscopy with a Connes-type interferometer. I. Instrumental. Rev. Sci. Instru. 42, 1393-1403.

Beer, R., and Taylor, F.W. (1973). The abundance of CH_3D and the D/H ratio in Jupiter. Astrophys. J. 179, 309-327.

Beer, R. and Taylor F.W. (1978a). The D/H and C/H ratios in Jupiter from the CH_3D phase. Astrophys. J. 219, 763-767.

Beer, R and Taylor, F.W. (1978b). The Abundance of Carbon Monoxide in Jupiter. Astrophys. J. in press.

Chandrasekhar, S. (1960). Radiative Transfer, Dover Publications, New York.

Chase, S.C., Ruiz, R.D., Münch, G., Neugebauer, G., Schroeder, M. and Trafton, L.M. (1974). Pioneer 10 infrared radiometer experiments: preliminary results. Science, 183, 315-317.

Coffeen, D.L. (1974). Optical polarization measurements of the Jupiter atmosphere at 103^{o} phase angle. J. Geophys. Res. 79, 3645-3652.

Gillett, F.C. (1973). Unpublished communication. (Data from Orton [1975b]).

Gillett, F.C., Low, F.J. and Stein, W.A. (1969). The 2.8-14 micron spectrum of Jupiter. Astrophys. J. 157, 925-934.

Gillett, F.C. and Westphal, J.A. (1973). Observations of 7.9 micron limb-brightening on Jupiter. Astrophys. J. 179, L153-L154.

Hovis, W.A., and Tobin, M. (1967). Spectral measurements from 1.6 μ to 5.4 μ of natural surfaces and clouds. Appl. Opt. 6, 1399-1402.

Ingersoll, A.P.(1976). The atmosphere of Jupiter. Space Sci. Rev. 18, 603-634.

Ingersoll, A.P., and Cuzzi, J.N. (1969). Dynamics of Jupiter's cloud bands. J. Atmos. Sci. 26, 981-985.

Ingersoll, A.P., Münch, G., Neugebauer, G., Diner, D.J., Orton, G.S., Schupler, B., Schroeder, M., Chase, S.C., Ruiz, R.D. and Trafton, L.M. (1975). Pioneer 11 infrared radiometer experiment: The global heat balance of Jupiter. Science 188, 472-473.

Ingersoll, A.P., Münch, G., Neugebauer, G., and Orton, G.S. (1976). Results of the infrared radiometer experiment on Pioneers 10 and 11. In Jupiter, University of Arizona Press, Tucson, 197-205.

Keay, C.S.L., Low, F.J., and Rieke, G.H. (1972). Infrared maps of Jupiter. Sky & Tel. 44, 296-297.

Keay, C.S.L., Low, F.J., Rieke, G.H., and Minton, R.B. (1973). High resolution maps of Jupiter at five microns. Astrophys. J. 183, 1063-1973.

Kieffer, H.H. (1975). Private communication.

Larson, H.P., Fink, U., Treffers, R. and Gautier III, T.N. (1975). Detection of water vapor on Jupiter. Astrophys. J. 197, L137-L140.

Lewis, J.S. (1969). The clouds of Jupiter and the NH_3-H_2O and NH_3-H_2S systems. Icarus 10, 365-378.

Orton, G.S. (1975a). The thermal structure of Jupiter. I. Implications of Pioneer 10 radiometer data. Icarus 26, 125-141.

Orton, G.S. (1975b). The thermal structure of Jupiter. II. Observations and analysis of 8-14 micron radiation. Icarus 26, 142-158.

Orton, G.S. and Terrile, R.J. (1978). Multiple frequency sounding of a Jovian cloud. Icarus, in press.

Owen, T. (1969). The spectra of Jupiter and Saturn in the photographic infrared. Icarus 10, 355-364.

Palmén, E. and Newton, C.W. (1969). Atmospheric Circulation Systems, Academic Press, New York and London.

Peek, B.M. (1958). The Planet Jupiter, Faber and Faber, London.

Reese, E.J. (1972). Jupiter: Its Red Spot and disturbances in 1970-1971. Icarus 17, 57-72.

Rossow, W.B. (1977). Cloud microphysics: Analysis of the clouds of Earth, Venus, Mars and Jupiter.

Russell, R.W. and Soifer, B.T. (1977). 5-8 μ observations of Jupiter and Saturn. Icarus 30, 282-285.

Smith, B.A. and Hunt, G.E. (1976). Motions and morphology of clouds in the atmosphere of Jupiter. In Jupiter, University of Arizona Press, Tucson. 564-585.

Terrile, R.J. and Westphal, J.A. (1977a). The vertical cloud structure of Jupiter from 5 μm measurements. Icarus 30, 274-281.

Terrile, R.J. and Westphal, J.A. (1977b). Infrared imaging of Jupiter in the 8-14 micrometer spectral region. Icarus 30, 730-735.

Trafton, L.M. and Stone, P.H. (1974). Radiative-dynamical equilibrium states for Jupiter. Astrophys. J. 188, 649-655.

Weidenschilling, S.J. and Lewis, J.S. (1973). Atmospheric and cloud structures of the Jovian planets. Icarus 20, 465-476.

Westphal, J.A. (1969). Observations of localized 5-micron radiation from Jupiter. Astrophys. J. 157, L63-L64.

Westphal, J.A. (1971). Observations of Jupiter's cloud structure near 8.5 μm, In Planetary Atmospheres, (C. Sagan, T.C. Owen, and H.J. Smith, eds.) D. Reidel, Dordrecht-Holland, 359-362.

Westphal, J.A. (1973). Application of the SIT vidicon to astronomical measurements. In Astronomical Observations with Television - Type Sensors (J.W. Glaspey and G.A.H. Walker, eds.), University of British Columbia, Vancouver.

Westphal, J.A., Matthews, K., and Terrile, R.J. (1974). Five micron pictures of Jupiter. Astrophys. J. 188, L111-L112.

Wildey, R.L., Murray, B.C. and Westphal, J.A. (1965). Thermal infrared emission of the Jovian disk. J. Geophys. Res. 70, 3711-3719.